

ABSTRACT

STRAKA, WESTON J. Chemical Solution Deposition Based Synthesis of High Symmetry Phase of Hafnium Dioxide Thin Films. (Under the direction of Dr. Justin Schwartz.)

Hafnium dioxide has attracted a great deal of attention recently due to its potential use in two different electronic applications: CMOS and FeRAM. In CMOS, the usefulness of hafnia comes in due to its high dielectric constant and compatibility with current IC processing parameters. For FeRAM, hafnia's recent discovery to exhibit ferroelectricity in an orthorhombic phase makes this material attractive for replacement of the ferroelectric material in FeRAM.

This study shows the feasibility of depositing thin films of hafnium oxide via chemical solution deposition for integration into these devices. The processing parameters necessary to produce this phase show how non-equilibrium processing plays a role in its synthesis. The temperature necessary to achieve the high symmetry phase was at 725 °C for 3 minutes on sapphire, silicon, and coated silicon substrates. The thermal conductivity of each was viewed as the property that allowed the hafnia formation. The dielectric constant of the hafnia films were between 30 and 32 with low dissipation factors and up to 47 with a poor dissipation factor all at 1 kHz. The formation of this phase was shown to be thickness independent with the high symmetry phase existing up to 300 nm film thickness. Interfacing the hafnia film with nickel ferrite was also studied to identify the possibility of using this composite for non-destructive reading of FeRAM. The magnetic properties showed an unchanged nickel ferrite film but the interface between the two was poor leading to the conclusion that more work must be done to successfully integrate these two films.

© Copyright 2017 Weston Straka

All Rights Reserved

Synthesis of High Symmetry Phase of Hafnium Dioxide Thin Films and Nickel Ferrite's
Effect on Microstructure in Composite Heterostructure

by
Weston J. Straka

A dissertation submitted to the Graduate Faculty of
North Carolina State University
in partial fulfillment of the
requirements for the degree of
Doctor of Philosophy

Materials Science and Engineering

Raleigh, North Carolina

2017

APPROVED BY:

Justin Schwartz
Committee Chair

Frank Hunte

Jacob Jones

Divine Kumah

DEDICATION

To my king and my savior, Jesus Christ, everything I am is yours.

BIOGRAPHY

Weston went to NC State University from 2008-2012 to study materials science and engineering for his undergraduate degree. He then attended the same university for his graduate work and got his doctorate in 2017.

ACKNOWLEDGMENTS

I would like to thank Dr. Justin Schwartz for his support and understanding over the last five years. Research often doesn't work as you (or your advisor) expects and a lot of patience is necessary.

I would like to thank Dr. Jacob Jones, Dr. Frank Hunte, and Dr. Divine Kumah for agreeing to be on my committee.

I would like to thank the NSF for their support on this project under the grant CMMI-1634955

This work was performed in part at the Analytical Instrumentation Facility (AIF) at North Carolina State University, which is supported by the State of North Carolina and the National Science Foundation (award number ECCS-1542015). The AIF is a member of the North Carolina Research Triangle Nanotechnology Network (RTNN), a site in the National Nanotechnology Coordinated Infrastructure (NNCI).

I would like to thank the countless other professors for their advice and guidance and their patience in my asking many questions.

I would like to thank my research group for their friendship and spitballing all of my ideas with me.

My friends and family have been huge in emotional and mental support throughout this difficult process. Without them, I would not have made it through.

TABLE OF CONTENTS

LIST OF TABLES	viii
LIST OF FIGURES	ix
CHAPTER 1: MOTIVATIONS AND OVERVIEW	1
1.1 Motivations	1
1.2 Overview	1
CHAPTER 2: BACKGROUND	3
2.1 Electrical Materials and Measurements	3
2.1.1 Capacitor Basics	3
2.1.2 Capacitors Versus Resistors	5
2.1.3 Mechanisms for Polarization in Dielectrics	6
2.1.3.1 Electronic Polarization	7
2.1.3.2 Ionic Polarization	7
2.1.3.3 Orientation Polarization	8
2.1.4 Linear Behavior of Dielectrics	9
2.1.5 Ferroelectrics	10
2.1.6 Mechanism of Ferroelectricity	11
2.1.7 Piezoelectricity	13
2.1.8 Electrical Measurements of Dielectrics and Ferroelectrics	14
2.1.8.1 Polarization Measurement	14
2.1.8.2 Transient Current Measurement	15
2.1.8.3 Leakage Current Measurement	16
2.1.8.4 Other Electrical Measurements	17
2.1.8.5 Electrical Breakdown	17
2.1.9 Measurement of Piezoelectric Properties	18
2.1.10 Dielectric Loss	19
2.2 Magnetism and Magnetic Materials	21
2.2.1 Magnetism	21
2.2.2 Origins of Magnetism in Materials	21
2.2.3 Magnetic Materials	22
2.2.3.1 Diamagnetic Materials	22
2.2.3.2 Paramagnetic Materials	23

2.2.3.3 Ferromagnetic Materials	24
2.2.4 Magnetic Domains	24
2.2.5 Ferrimagnetic and Antiferromagnetic Materials.....	26
2.2.6 Measurements of Magnetic Materials.....	27
2.2.7 Mechanism Behind Ferromagnetism	28
2.2.8 Magnetocrystalline Anisotropy.....	29
2.2.9 Magnetostriction	32
2.3 Magnetoelectricity	33
2.3.1 Magnetoelectric Effect.....	33
2.3.2 Magnetoelectric Materials	34
2.3.3 Piezomagnetism	35
2.3.4 Magnetoelectric Composites.....	37
2.4 Ferroelectric Random Access Memory	39
2.4.1 Computer Memory Basics	39
2.4.2 Ferroelectric Memory	39
2.5 Materials	43
2.5.1 Hafnium Oxide.....	43
2.5.2 Ferrites	45
2.6 Chemical Solution Deposition	47
CHAPTER 3: INSTRUMENTATION	49
3.1 GIXRD.....	49
3.2 AFM.....	52
3.3 XRR	53
3.4 Electrical Measurements	54
CHAPTER 4: PROCESSING OPTIMIZATION OF HIGH SYMMETRY HAFNIA THIN FILMS ON SAPPHIRE	55
4.1 Annealing Temperature Study	55
4.2 Starting Temperature Study	60
4.3 Solution Concentration Study	64
CHAPTER 5: PROCESSING STUDY AND ELECTRICAL PROPERTIES OF HIGH SYMMETRY PHASE HAFNIA THIN FILMS GROWN ON SILICON.....	69
5.1 Substrate Thickness Study	70

5.2 Intermediary Layer Study	74
5.3 Electrical Properties of the High Symmetry Phase Hafnia Films.....	79
5.4 Multiple Coats Study	85
CHAPTER 6: PRELIMINARY WORK ON THE EFFECTS OF COMPOSITE HETEROSTRUCTURE ON THE PHASE OF HAFNIA AND MAGNETIC PROPERTIES OF FERRITE.....	92
6.1 Phase Retention of Hafnia in Composite	93
6.2 Effects of Composite on Magnetic Properties	104
CHAPTER 7: SUMMARY OF WORK.....	110
REFERENCES.....	116

LIST OF TABLES

Table 2.1 This table shows the properties of several memory types in use today.....	42
Table 2.2 Comparison of some properties of a few well studied ferrites and a few well studied metal ferromagnets.....	46
Table 4.1 This table shows the peak heights for the major diffraction peaks in Figure 3.3. The ratios of the peak heights are also shown which gives an indication of the phase fraction of each phase	68
Table 5.1 This is a table showing the lattice mismatch between the different directions of the high symmetry phases of hafnia and both silicon and sapphire substrates.....	73
Table 5.2 This is a table comparing some of the electrical properties of hafnia films in this work to the hafnia films found in literature	84
Table 5.3 Shown in this table are the thickness of the hafnia film, the relative permittivity, and the leakage currents at 1.1 V and 1 MV/cm.....	90
Table 6.1 This table shows the magnetization data pulled from the hysteresis curves for NFO and the NFO/HfO ₂ composites.....	108

LIST OF FIGURES

Figure 2.1 A schematic of a parallel plate capacitor with electrode area of A separated by a distance d	4
Figure 2.2 This is a schematic of a dipole moment created by two equal but opposite charge centers separated by a distance apart.....	6
Figure 2.3 This is a schematic of the potential energy plot as a function of displacement. For this a) shows the placement of the ion with no electric field and b) shows the ion when there is an electric field.....	10
Figure 2.4 This is a schematic for the potential energy of a non-centrosymmetric ion within a ferroelectric material.....	12
Figure 2.5 This is an example plot of the polarization as a function of the electric field for an ideal ferroelectric. Marked on the plot are different points corresponding to various characteristics.....	15
Figure 2.6 These are plots of the transient current of an ideal a) dielectric and b) ferroelectric.....	16
Figure 2.7 These are example plots of the magnetization as a function of applied magnetic field for a) a diamagnetic material and b) a paramagnetic material.....	23
Figure 2.8 This is a schematic of the domain structure of a ferromagnetic material in order to reduce the overall energy of the system.....	25
Figure 2.9 These are schematics of the moments of a) ferrimagnetic materials and b) antiferromagnetic materials.....	27
Figure 2.10 This is a schematic of the magnetization as a function of applied magnetic field for a ferromagnetic material. The points of saturation, remanent, and coercive fields are marked.....	28
Figure 2.11 This is a plot of the exchange integral as a function of the ratio of atomic radius to the radius of the 3d orbital. Several 1st row transition elements are shown....	29
Figure 2.12 This is a schematic of the magnetization of a material along its easy, medium, and hard axes.....	31
Figure 2.13 This is a schematic of the domain structure of a block of iron. The domain walls align with the grain boundaries. The grains marked in red have the 100 axis pointing vertically. The grains marked in blue have the 111 axis pointing vertically. The image on the left is state 1 (no applied magnetic field). The image on the right is state 2 (magnetic field pointing vertically).....	33
Figure 2.14 This is a schematic of the 1T1C FeRAM. The initialism BL stands for bit line, PL for plate line, and WL for word line.....	40
Figure 2.15 This is a schematic of the 1T1C FeRAM. The initialism BL stands for bit line, PL for plate line, and WL for word line.....	41
Figure 3.1 This is a schematic for standard Bragg-Brentano geometry x-ray diffraction. Marked are angles described using this technique.....	50
Figure 3.2 Shown are the schematics for where diffraction peaks originate in a) Bragg-Brentano and where the peaks originate from in b) grazing incidence x-ray diffraction.	51

Figure 4.1 This is a plot of the diffraction spectra of a hafnia thin film on c-cut sapphire. The annealing time and temperature is shown beside each curve. The standard peak positions for each space group of hafnia are also shown below the diffraction spectra with the space group marked.....	57
Figure 4.2 This is a plot of the diffraction spectra of a hafnia thin film on c-cut sapphire. The annealing time and temperature is shown beside each curve. The standard peak positions for each space group of hafnia are also shown below the diffraction spectra with the space group marked.....	60
Figure 4.3 This is a plot of the temperature profiles used in this study. Each plot extends over 3 minutes of time. The alumina boat was cooled to vary the starting temperature and each time, the boat was placed back into the center of a preheated tube furnace at 725 °C.....	62
Figure 4.4 This is a plot of the GIXRD diffraction data of the hafnia film produced by varying the starting temperature of each sample. The diffraction data from each film has the starting temperature of that sample marked beside it. Below the diffraction plot is the standard peak positions of each phase of hafnia with the space group marked beside each one.....	64
Figure 4.5 This is a plot of the GIXRD spectra from the hafnia thin films. The concentration for the precursor solution used to produce each hafnia thin film is shown beside each curve. The standard peak positions for each space group of hafnia is shown below the diffraction plots with the space group marked.....	66
Figure 5.1 This is a plot of the diffraction spectra of a hafnia thin film on varying thicknesses of silicon. The thickness of the silicon substrate used is shown beside each diffraction spectrum. The standard peak positions for each space group of hafnia are also shown below the diffraction spectra with the space group marked.....	71
Figure 5.2 This is a plot of the diffraction spectra from hafnia films grown on 670 μm thick silicon substrates with different intermediary layers. The intermediary layers are marked next to each spectrum. The standard peak positions for each phase of hafnia is shown below the plot with the space group marked.....	76
Figure 5.3 This is a plot of the diffraction spectra from hafnia films grown on 370 μm thick silicon substrates with different intermediary layers. The intermediary layers are marked next to each spectrum. The standard peak positions for each phase of hafnia is shown below the plot with the space group marked.....	77
Figure 5.4 These are AFM height retraces of the hafnia layer on top of a) 670 μm silicon, b) 670 μm thick platinized silicon, c) 670 μm thick titanium nitride coated silicon, d) 370 μm thick silicon, and e) 370 μm thick platinized silicon.....	78
Figure 5.5 This is a plot of the polarization of a hafnia film grown on 670 μm thick silicon coated with TiN.....	80
Figure 5.6 These are the height retraces from AFM of the hafnia film on a) 670 μm thick platinized silicon and b) 370 μm thick platinized silicon.....	81
Figure 5.7 These are the XRR spectra for the hafnia film on a) 670 μm thick platinized silicon and b) 370 μm thick platinized silicon.....	81

Figure 5.8 This is a plot of the normalized capacitance values and dissipation factor for the hafnia films grown on 670 μm thick platinized silicon and 370 μm thick platinized silicon. The solid lines correspond to the capacitance while the dashed lines correspond to the dissipation factor.....	82
Figure 5.9 This is a plot of the polarization and the transient current for the hafnia film grown on 370 μm thick platinized silicon. The curves show good dielectric behavior with little losses. The small losses are indicated by near linear behavior in the polarization curve and the rectangular shape of the transient current plot.....	84
Figure 5.10 This is a plot of the GIXRD spectrum for the hafnia films at different thicknesses. The diffraction data for each film is marked with the thickness of the film. The standard peak positions are also shown below the spectra with the space groups listed.....	88
Figure 5.11 These are the XRR spectra for the hafnia layer on 370 μm thick platinized silicon with the number of coats marked by each spectra.....	89
Figure 5.12 These are the 3D representations of the height retraces of the hafnia films on 370 μm thick platinized silicon. The RMS roughness values are shown below each figure.	90
Figure 5.13 These are the polarization curves for each hafnia film up to 1 MV/cm.....	91
Figure 6.1 This is the GIXRD plot of the nickel ferrite film on various substrates. Shown below the diffraction data are the standard peak positions of the nickel ferrite..	94
Figure 6.2 This is the XRR spectra for the nickel ferrite film on the marked substrates.	95
Figure 6.3 These are the height retraces of the nickel ferrite film on a) 370 μm thick platinized silicon, b) 670 μm thick platinized silicon, and c) 670 μm thick silicon coated with TiN.....	95
Figure 6.4 This is a set of GIXRD plots for the nickel ferrite thin film stacked on top of the hafnia film. The substrate for each GIXRD plot is shown. Also shown are the standard peak positions for the nickel ferrite film and the phases of hafnia all marked with the appropriate space group.....	98
Figure 6.5 This is the GIXRD plot of hafnia films on 370 μm thick platinized silicon that have been annealed once and twice as marked on the plot. Shown below the plot are the standard peak positions for each phase of hafnia.....	99
Figure 6.6 This is the GIXRD plot of hafnia films on 670 μm thick platinized silicon that have been annealed once and twice as marked on the plot. Shown below the plot are the standard peak positions for each phase of hafnia.....	100
Figure 6.7 This is the GIXRD plot of hafnia films on 670 μm thick silicon with a TiN coating that have been annealed once and twice as marked on the plot. Shown below the plot are the standard peak positions for each phase of hafnia.....	101
Figure 6.8 These are the height retraces of the nickel ferrite layer stacked on top of the hafnia layer on a) a 370 μm thick platinized silicon substrate, b) a 670 μm thick platinized silicon substrate, and c) a 670 μm thick silicon substrate coated with TiN.....	102

Figure 6.9 This is a bright field TEM cross section of the composite. Each layer is labeled. The platinum layer shows large grains while the hafnium dioxide layer is very fine grained. The nickel ferrite layer does not appear to interface well with the hafnia as evidenced by the bright spots which are indicative of voids. The grain structure of the nickel ferrite is also much large than that of the hafnia.....	103
Figure 6.10 This is a plot of the magnetization of pure nickel ferrite and the nickel ferrite/hafnia composite on 370 μm thick platinized silicon with an inset showing the remanent magnetization and coercive fields.....	105
Figure 6.11 This is a plot of the magnetization of pure nickel ferrite and the nickel ferrite/hafnia composite on 670 μm thick platinized silicon with an inset showing the remanent magnetization and coercive fields.....	106
Figure 6.12 This is a plot of the magnetization of pure nickel ferrite and the nickel ferrite/hafnia composite on 670 μm thick silicon coated with TiN with an inset showing the remanent magnetization and coercive fields.....	107

CHAPTER 1

MOTIVATIONS AND OVERVIEW

1.1 Motivations

The higher symmetry phases of hafnia (cubic, tetragonal, orthorhombic) are of interest within the realm of both high-k dielectric materials and ferroelectric materials [1], [2]. These higher symmetry phases of hafnia have only ever been achieved using dopants [3]–[5] or from vacuum-based deposition techniques [6]–[8]. To begin to understand this material more fully and to facilitate its synthesis, chemical solution deposition can be utilized to create these thin films. The processing parameters necessary to create these phases of hafnia are also important to know for wider use. If this material is made to be ferroelectric, its integration with a ferromagnetic material can allow for the system to be utilized in ferroelectric RAM without a destructive read process. To ensure this possibility, the magnetic properties and electrical properties of the system must be measured.

1.2 Overview

This dissertation provides insight into the processing/structure/property relationships of the high symmetry phases of hafnium dioxide and a composite of hafnia and nickel ferrite.

Chapter 1 provides the motivation for researching this topic and a brief description of the structure of this dissertation. Chapter 2 looks into the necessary background to understand the proceeding chapters in terms of electrical and magnetic properties of materials, applications for these materials, and the materials themselves. Chapter 3 briefly explains the instrumentation used for the proceeding studies. Chapter 4 explores the processing steps

necessary to achieve the higher symmetry phases of hafnium dioxide thin films as deposited on sapphire. Chapter 5 builds on the work in chapter 3 and explores the processing of the high symmetry phases of hafnia on silicon and their electrical and microstructural properties. Chapter 6 looks into the preliminary work done on integrating a ferromagnetic material with hafnium dioxide. In this chapter, the effects on the magnetic properties and phase of the constituent films are studied. Chapter 7 gives a broad overview of the research developed in this work along with specific, important results and how they inform future directions of research.

CHAPTER 2

BACKGROUND

2.1 Electrical Materials and Measurements

2.1.1 Capacitor Basics

Dielectric materials are a class of materials with a wide variety of applications in today's electronics. To understand the physics behind these materials, a basic understanding of some aspects of electronics must be established.

Dielectric materials are mostly commonly used as the insulating material in a capacitor.

When a parallel plate capacitor, Figure 2.1, whose electrodes are separated by a distance d apart and with electrode areas of A , is placed into a vacuum, the capacitance of this capacitor is given by

$$C_o = \epsilon_o A/d$$

Equation 2.1

If an electric field is applied to the capacitor, the amount of charge, Q_o , stored in the capacitor is

$$Q_o = A\epsilon_o E$$

Equation 2.2

$$E = V/d$$

Equation 2.3

where E is the electric field applied to the capacitor and V is the voltage. In both of those equations, ϵ_o is the permittivity of vacuum. The permittivity is defined as the ability of that

medium to hold a charge. For vacuum, this number is defined as $8.85 * 10^{-12}$ F/m and is a universal constant. If a material is inserted between the two plates and this material does not pass charge between the two plates, equation 1.2 becomes

$$Q = A\epsilon_0\epsilon_r E$$

Equation 2.4

where ϵ_r is defined as the relative permittivity of the material. In this context, relative means as compared with the vacuum permittivity; i.e. a material with a true permittivity of $17.7 * 10^{-12}$ F/m will have a relative permittivity of 2. Equation 2.4 shows that inserting a material with a relative permittivity greater than one will increase the amount of charge stored in the capacitor at a given electric field. The result is that the greater the relative permittivity of the material inserted into the capacitor, the greater the charge stored in that capacitor at the same magnitude of electric field which is useful for energy storage.

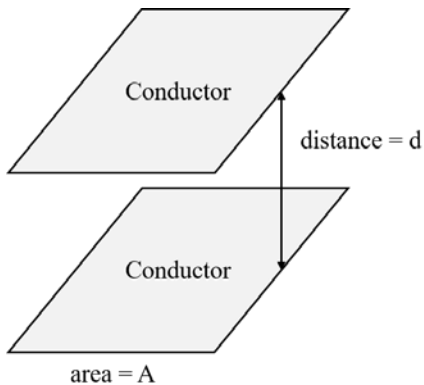


Figure 2.1 A schematic of a parallel plate capacitor with electrode area of A separated by a distance d .

The assumption made above (the material would not pass charge) is an important one for the application of capacitors. There are three basic groups of materials: conductors, semiconductors, and insulators. Of these three groups, insulators tend to be used as the

medium in capacitors. By definition, insulators are poor conductors of electricity due to their large band gap. Within the realm of capacitors, these insulators are known as dielectrics.

2.1.2 Capacitors Versus Resistors

At this point, it is important to make a distinction between a resistor and a capacitor. In a resistor (similar to a capacitor), a resistive material is placed in line with conductive materials. However, the characteristics that define each are different. Impedance is the measure of the opposition of current flow for a given applied voltage. The units for impedance are Ohms and it is usually shown as the variable Z . Impedance is given by equation 2.5 as

$$Z = R + jX$$

Equation 2.5

where R is the resistance (the real part of impedance), X is the reactance (the imaginary part of impedance), and j is the square root of -1. An ideal resistor would have zero reactance (all of the impedance would come from the resistance) and an ideal capacitor would have zero resistance (all of the impedance would come from the reactance). The impedance of an ideal resistor is frequency independent. Due to the mechanisms behind how dielectrics work (which will be covered later), the impedance of a capacitor directly depends on the frequency of the applied voltage and, in an ideal capacitor, the voltage would lag behind the current by $\pi/2$ radians. In reality, every capacitor has some resistance and every resistor has some reactance. For the background portion of this dissertation, the assumption made will be that the capacitor is ideal (the only contribution to the impedance comes from the reactance).

2.1.3 Mechanisms for Polarization in Dielectrics

The reason a dielectric increases the charge in a capacitor in a given electric field is due to the dipole moments that are created within the material. When a dielectric is introduced to an electric field, a force begins to act upon all of the charged species inside of the material. This force causes the negatively charged species to be drawn toward the positive side of the electric field while the positively charged species are drawn away from the positive side of the electric field. The spatial offset in opposite charge centers is a dipole. A dipole moment is the magnitude of that dipole and is defined as

$$\mu = Qd$$

Equation 2.6

where Q is the charge of the species and d is the separation distance between the charge centers. A schematic of this is shown as Figure 2.2. The summation of all dipole moments over a given volume is known as the polarization. There exist three main ways that polarization can be achieved inside of a material: electronic polarization, ionic polarization, and orientation polarization.

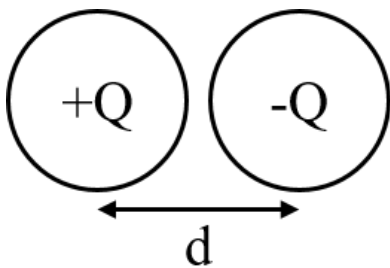


Figure 2.2 This is a schematic of a dipole moment created by two equal but opposite charge centers separated by a distance apart.

2.1.3.1 Electronic Polarization

To understand electronic polarization, assume a single atom whose position is fixed in space with a spherical electron cloud. Application of an electric field across that atom will cause the charged species (electrons and protons) to feel a force act upon them. The electron cloud will be drawn toward the positive side of the electric field while the nucleus will be repelled from that side. This is known as electronic polarization. After the electric field is removed, the atom returns to its normal state. For atoms with a spherical electron cloud, the dipole moment tends to be very small and therefore these materials have a fairly small polarization. However, because the p-block and d-block electron clouds are more directional, the effects of electronic polarization can be more pronounced. This is especially true for covalently bonded materials. For example, due to sp^3 orbital hybridization in pure silicon, the relative permittivity in this material is roughly 12 which comes almost exclusively from electronic polarization.

2.1.3.2 Ionic Polarization

Ionic polarization occurs when the molecule is comprised of two or more different elements whose electronegativity is fairly different and whose shape is non-symmetrical. As a simplistic example, a single molecule of sodium chloride ($NaCl$) is comprised of an electropositive sodium atom and an electronegative chlorine atom. When these two atoms bond, the chlorine pulls an electron from the sodium atom forming an anion-cation pair. This forms a natural dipole where the anion has a slightly negative charge and the cation has a slightly positive charge. If the system is built up to have a significant mass of sodium

chloride molecules, all of the moments cancel out entirely. However, upon application of an electric field, the ions slightly displace from their equilibrium position in a similar manner to the electron cloud and nucleus in electronic polarization. For the given example, after the field is removed, the ions return back to their equilibrium position and the net polarization is zero.

2.1.3.3 Orientation Polarization

The remaining type of polarization that commonly exists is known as orientation polarization. The previous two types of polarization assumed that the atoms or molecules were fixed in space. If spatially fixed, the electron cloud-nucleus pair or the anion-cation pair would stretch to align the negative tail of the dipole toward the positive side of the electric field and the positive tail of the dipole would align toward the negative or ground side of the electric field. If, from the ionic polarization example, a single sodium chloride molecule was not fixed but allowed to rotate freely, the application of an electric field would cause the molecule to rotate such that the chlorine ion was aligned toward the positive side of the electric field and the sodium ion was aligned toward the negative side of the electric field. This is an example known as orientation polarization. Similar to sodium chloride, a water molecule has a natural dipole associated with it because the oxygen has a negative charge and the hydrogens have a positive charge. In a volume of water, all of the water molecules are allowed to rotate pretty freely. Upon application of an electric field, the water molecules align to reduce energy which causes the oxygen atoms to align toward the positive side of the field.

2.1.4 Linear Behavior of Dielectrics

Every single material can be polarized. This is because every single material has electrons and nuclei which will respond to an electric field. However, for conductors and some semiconductors, this is not practical as any contact with the surface of the material will immediately allow for charge flow which will destroy the polarization in the material.

Most dielectric materials exhibit both electronic and ionic polarization. When an electric field is applied across the dielectric, the electron clouds/nuclei pairs and anion/cation pairs displace slightly. That dielectrics will have anion/cation pairs can be assumed is fair in that almost every insulator is comprised of at least two elements and these elements, when bonded, will have some ionic character to them. Once the electric field is removed, the species return to their equilibrium positions. Following an energy versus displacement plot for an ion in a dielectric (Figure 2.3a), the application of an electric field increases the energy in the system (Figure 2.3b) and causes the ion to be displaced from its energy minima. The direction of the displacement depends on the direction of the electric field and the electric character of the species displaced. Once the field is removed, the ion returns to its energy minima and its equilibrium position. This is a qualitative understanding as to the linear nature of the polarization of dielectrics as a function of applied voltage.

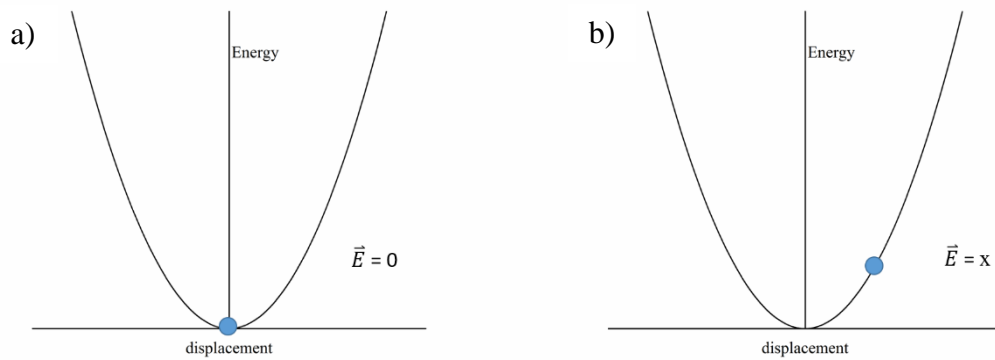


Figure 2.3 This is a schematic of the potential energy plot as a function of displacement. For this a) shows the placement of the ion with no electric field and b) shows the ion when there is an electric field.

2.1.5 Ferroelectrics

Ferroelectrics are a special kind of dielectric material whose electric polarization can be reversed upon application of an electric field. Additionally, once the electric field is removed from the ferroelectric, a net polarization still exists in the material. This makes a ferroelectric a material with non-linear dielectric behavior. It is necessary for the crystal structure of ferroelectrics to be non-centrosymmetric which means there is no inversion center. Of the 32 crystal classes, 21 are non-centrosymmetric. Of these 21 crystal classes, 20 exhibit piezoelectricity or the generation of surface charges in response to an external stress. Of these 20 piezoelectric crystal classes, 10 are pyroelectric which means they have a spontaneous change in polarization in response to a change in temperature. Of these 10 crystal classes, only a few exhibit ferroelectricity. This means that all ferroelectrics show pyroelectricity and piezoelectricity. From a crystallographic point of view, there is no distinction between a pyroelectric material and a ferroelectric material. The only difference

between the two is that a ferroelectric can have its polarization states switched from an applied electric field before the material exhibits a voltage breakdown. It is possible that the polarization states in a pyroelectric material could be switched from an applied electric field but the energy necessary to do so is higher than the material's ability to resist electric breakdown.

2.1.6 Mechanism of Ferroelectricity

Of all dielectrics, ferroelectrics tend to have the highest relative permittivity due to the presence of all three kinds of polarization modes. As is true for all materials, electronic polarization exists in ferroelectrics from the electron cloud/nucleus displacement. The ionic polarization comes from the difference in electronegativity between the ions in the compound. The orientational polarization comes from the non-centrosymmetry of the crystal structure. Within every crystal structure, each atom has an equilibrium position as shown in the schematic plot, Figure 2.3a. A change in the position of ion from its equilibrium position will change the potential energy of that ion. In Figure 2.3b, moving the ion in either the positive or negative x-direction necessitates an increase in the potential energy of the ion. For ferroelectric crystals, the potential energy plot of the non-centrosymmetric ions begins to develop two local minima instead of one. A schematic for this plot is shown as Figure 2.4. As evidenced by this potential energy plot, the non-centrosymmetric ion can exist in one of two physical locations and be in thermal equilibrium. When an electric field is applied to the ferroelectric that is not orthogonal to the axis of displacement for the non-centrosymmetric ion, the ion will displace into one of the energy minimas. When this field is removed, the ion

will tend to stay in that energy minima. Because of this displacement, there exists a net dipole in each unit cell and, summed over the entire volume, the crystal is polarized.

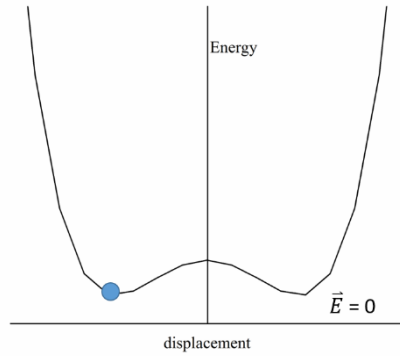


Figure 2.4 This is a schematic for the potential energy of a non-centrosymmetric ion within a ferroelectric material.

In a local region of the crystal, the non-centrosymmetric ions will sit on the same side of the double potential well (as shown in Figure 2.4). This local area of similarly seated ions is called a domain. Within ceramic ferroelectrics, domains do not have to correspond to grains; i.e. they can be smaller or larger than actual grains. Within a given domain, the polarization among all the unit cells will be in the same direction. A material comprised of many randomly oriented domains will have a net polarization of zero. Once the electric field is applied across the ferroelectric, the ions will try to align as best as possible with the field to reduce energy. This is known as poling the sample.

From the potential energy plot shown in Figure 2.4, if the temperature of the system were raised, the ion would have sufficient energy to then go between each of the two potential wells freely. Because there would be an equal probability of being in either well, the time

averaged position of that ion would converge onto the center of that potential energy plot. As the temperature continues to increase, the minima would converge into the center. This temperature at which the minima first converge is known as the Curie temperature. It's defined as the temperature at which the material is no longer ferroelectric, typically due to a phase change.

2.1.7 Piezoelectricity

As mentioned before, all ferroelectrics exhibit piezoelectricity. There also exist materials that exhibit piezoelectricity that do not exhibit ferroelectricity. Piezoelectricity is the response of a material to an electric field by straining and, conversely, the response of a material to mechanical stress by becoming polarized. A requirement of piezoelectric crystals is that they have no inversion center. If this is the case, within a single unit cell, an ion is slightly displaced from the center of the unit cell. When the material is stressed, the ion will move further from the center creating a larger dipole within the unit cell. Conversely, when an electric field is applied across the material, the ion will displace further from the center causing the unit cell to strain. This behavior makes piezoelectric materials useful in a variety of applications including: sensors [9], actuators [10], power sources [11], and increasing efficiency in photovoltaics [12].

2.1.8 Electronic Measurements of Dielectrics and Ferroelectrics

2.1.8.1 Polarization Measurement

To qualify a ferroelectric material, several electrical properties are measured as a function of the applied electric field. These properties include the polarization, transient current, leakage current, fatigue, imprint, and retention. In a typical dielectric, the polarization is positively linearly proportional to the applied electric field. A ferroelectric, by contrast, has a non-linear response to the applied electric field. Per the discussion earlier, not only will a ferroelectric have electronic and ionic polarization (as every other dielectric) but will also have orientational polarization. This is from the non-centrosymmetric ion in the unit cell. An example polarization curve for a ferroelectric material is shown as Figure 2.5. The following explanation assumes a polycrystalline material. As the applied voltage increases, all of the modes of polarization are activated and begin aligning to the applied electric field. This is a linear response (point A to B). Eventually, the system is fully saturated (i.e. the only increase in polarization now comes from the further displacement of electron cloud/nucleus pairs or cation/anion pairs) which is denoted by point C. Once the field begins decreasing, the electronic and ionic polarization mechanisms begin to relax while the non-centrosymmetric ions remain in their energy potential wells. Point D on the plot is known as the remanent polarization (P_r) and is the total polarization left in the material after all of the electric field has been removed. Once the applied electric field goes negative, the electronic and ionic polarization mechanisms are the only types activated by the applied field. Once the electric field reaches a certain magnitude, the non-centrosymmetric ions jump to the other potential well. This is marked by a near vertical polarization response in the plot. The electric field

where the polarization crosses the x-axis (Point E) is known as the coercive field. The same mechanisms occur as before but in reverse.

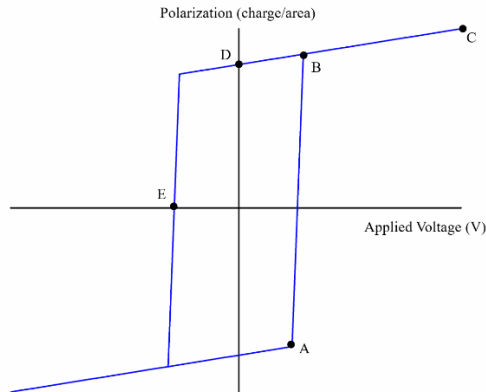


Figure 2.5 This is an example plot of the polarization as a function of the electric field for an ideal ferroelectric. Marked on the plot are different points corresponding to various characteristics.

2.1.8.2 Transient Current Measurement

The transient current plotted as a function of the applied electric field is important in helping to determine whether the polarization plot is indicative of a leaky dielectric or a ferroelectric material. For an ideal dielectric (one with no losses), the transient current plot appears as a perfect rectangle as shown in Figure 2.6a. In the case of a ferroelectric, the transient current plot has a rectangular shape with peaks appearing as shown in Figure 2.6b. These peaks correspond to the coercive field and occur at the point where the electric field is great enough to displace all of the non-centrosymmetric ions into the other side of the potential energy plot. Although no current is flowing through the dielectric (or at least no current should be flowing through the dielectric) the transient current measured comes from the movement of charges that can be detected with the measurement system. These charges don't flow through the dielectric as much as they are displaced within the system.

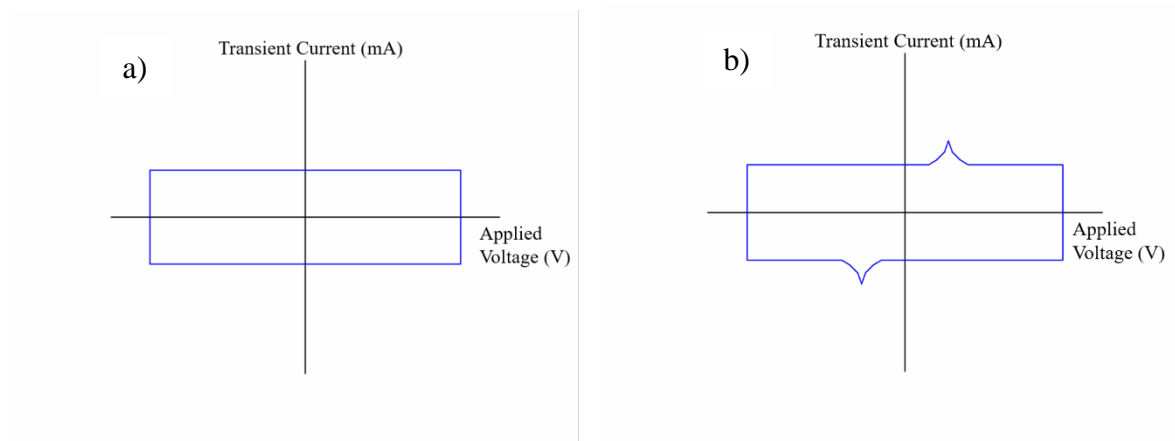


Fig 2.6 These are plots of the transient current of an ideal a)dielectric and b)ferroelectric.

2.1.8.3 Leakage Current Measurement

Leakage current is important to measure because it allows the user to know what engineering problems will arise in the device. Leakage current is the flow of current through the dielectric. It can be due to defects (grain boundaries, impurities, etc.) within the dielectric or because the material broke down. If the film has high leakage current, the material will continue to heat which can damage many of the components in the electronics and will further lead to more current flow. Additionally, in a capacitive role, a slow leakage current will dissipate the stored charge which will render the energy storage capabilities of that capacitor useless. To measure the leakage current, a steady state DC voltage is applied to the dielectric long enough that relaxation effects are negated but short enough that there will not be breakdown. Leakage current levels should be similar between dielectrics and ferroelectrics.

2.1.8.4 Other Electrical Measurements

Fatigue, imprint, and retention are all different things that negatively affect the performance of the capacitor for use as a ferroelectric. Fatigue is the decrease in polarization as the number of cycles increases in ferroelectrics. Imprint is a horizontal shift in the polarization curve. Retention is the ability of the ferroelectric to store the remanent polarization as a function of time. The mechanism behind fatigue is the entrapment of defects and impurities which leads to a loss of polarization [13]. This occurs because of the chemical instability of the grain boundaries. As the field alternates in the ferroelectric, the vacancies, impurities, and interstitials migrate towards the grain boundaries where their movement is stabilized. Imprint occurs due to space charges [14] and affects the amount of ions that can be switched. Retention is typically directly tied to the mobility of charged defects. If the charged defects are mobile, they help to compensate for the ‘charge’ in the ferroelectric from the displaced non-centrosymmetric ions.

2.1.8.5 Electrical Breakdown

One more important parameter to measure for a particular dielectric is its breakdown voltage. The origins of breakdown come from different mechanisms which are covered well in [15]. Breakdown typically occurs when the defects in the material migrate and cause a rapid change in the resistance of the dielectric. This causes a large, local current flow, destroys the material, and can damage the measuring electronics. When measuring and reporting the dielectric breakdown strength of a particular material, it is best to report the highest value

observed. This is because the lower values could come from localized defects, poor electrode deposition, or some other external factor which is not intrinsic to the given material.

2.1.9 Measurement of Piezoelectric Properties

One of the more important parameters for qualifying piezoelectrics is to measure the magnitude of strain as a function of applied electric field and to measure the polarization as a function of applied stress. Today, this is typically done in one of two ways: 1) apply a voltage and measure the displacement or 2) apply a stress and measure the polarization.

Method 1 typically involves the use of a capacitive displacement probe [16] or a laser interferometer [17]. A capacitive displacement probe is able to use the capacitance difference between the probe and the target to measure the distance between the two. In this way, the strain in the ferroelectric can be easily measured. Laser interferometry uses a modified Michelson experiment to measure the displacement of the piezoelectric as a function of the applied electric field. Method 2 typically involves stressing the material locally (with an AFM type tip) or in the bulk and measuring the voltage output from the material. An additional method that has been used to measure the piezoelectric effects in materials is with X-ray diffraction. Because there is a local displacement within the unit cell, an applied electric field can change shift peak along 2θ due to the strained unit cell. This is especially useful for thin films.

2.1.10 Dielectric Loss

For designers of electrical components, there are two main quantities of interest within dielectric materials: dielectric constant and loss. The dielectric constant, as mentioned before, is a proportionality constant that indicates to what extent the electric field can be reduced and the material can achieve the same charge. As shown previously, not all dielectrics will have all of its impedance from the reactance of the material. It was also shown that the capacitors are different than the resistors due to this difference in reactance versus resistance. This can be understood from the delay in response to an applied voltage. Assuming two parallel plates with vacuum as the separation between the two plates, an alternating voltage applied across the plates can be represented by the equation

$$v = V_m \cos(\omega t)$$

Equation 2.7

where v is the instantaneous voltage, V_m is the maximum voltage, and ω is the frequency of the applied voltage in radians per second. The current in that capacitor will be represented by the equation

$$i = I_m \cos\left(\omega t + \frac{\pi}{2}\right)$$

Equation 2.8

where the maximum current is represented by the equation

$$I_m = \omega C_o V_m$$

Equation 2.9

In equation 2.9, C_o is the vacuum capacitance. These equations show that the current through a perfect capacitor leads the voltage by 90° . If a dielectric is placed between the two parallel plates, the equations for current change to

$$i = I_m \cos \left[\omega t + \left(\frac{\pi}{2} - \delta \right) \right]$$

Equation 2.10

and

$$I_m = \omega C_o \epsilon_r V_m$$

Equation 2.11

where δ is the loss angle in radians and ϵ_r is the relative permittivity of the dielectric. In equation 2.10, it is evident that the larger the loss angle, the closer the current comes to being in-phase with the alternating voltage (the closer this material comes to being a resistor). The result is that the current can be split into two components: the component leading the applied voltage and the component in phase with the applied voltage. These two components can be viewed as the capacitive and resistive components of the dielectric, respectively. The dielectric loss is defined as the tangent of the loss angle which is proportional to the current in phase with the applied voltage or the resistive part of the material.

For designers, the goal of a good dielectric for use in a capacitive role, is to have a large dielectric constant (this increases the amount of charge that can be held in the capacitor as a function of unit voltage) and to have a small dielectric loss.

2.2 Magnetism and Magnetic Materials

2.2.1 Magnetism

Magnetism is a physical phenomenon that imparts force on all other objects around it. The origins of magnetism are from moving electrical charges. This is why magnetism can be observed in materials or in objects with current passing through. The effects of magnetism were discovered in ancient Greek society where some rocks would “stick” to pieces of iron through an invisible force. These rocks are called lodestones. Until the early 1800s, the only use of magnetism was to magnetize iron needles for use in compasses. In 1820, Hans Christian Oersted noticed that a magnetic iron needle would change direction upon application of current through a nearby wire. This led him to postulate that magnetic fields would be produced by current flowing through a wire. In 1821, he published a paper showing this phenomenon and research in magnetism has grown ever since.

2.2.2 Origins of Magnetism in Materials

The origin of magnetism in materials is due entirely to electron motion. Electrons have two primary kinds of motion, orbital and spin. Orbital motion can be thought of as the electron orbiting around the nucleus of the atom. Electron spin can be likened to an electron orbiting around its own axis. Both of these kinds of motion have an associated magnetic moment due to a charge moving in a loop (the loop around the nucleus or the loop around the electron’s own axis). Although these definitions of electron motion are not rigorously correct and have no quantitative significance, they help to visualize the derivation of magnetic moment.

Due to these electron motions, every material responds in some way to an applied magnetic field. The response to an applied magnetic field is known as magnetization. Magnetization is the sum of all magnetic moments within the system. The way that these materials respond dictate which of the three classes of magnetic materials they get grouped into. The groups of magnetic materials are diamagnetic, paramagnetic, and ferromagnetic.

2.2.3 Magnetic Materials

2.2.3.1 Diamagnetic Materials

Diamagnetic materials are materials that have a negative linear response to an applied magnetic field. This response is known as the susceptibility and is the slope of the magnetization as a function of the applied magnetic field. Once the field is removed, the magnetization goes back to zero. The reason for this negative response is due to the atoms having a closed shell. The magnetic moments of all of the electrons will perfectly cancel out. This can come from many materials including monoatomic noble gases, diatomic gases with closed shells, or ionic solids. Examples are He, N₂, and NaCl, respectively. This behavior is also seen in materials with primarily covalent bonds. The electrons are nearly perfectly shared and have almost perfect moment cancellation. This behavior is also seen in some metals and is a more complex behavior than simple closed electron shell configurations. Additionally, the susceptibility in diamagnetic materials is independent of temperature. An example plot of the magnetization of a diamagnetic material as a function of applied magnetic field is shown as Figure 2.7a.

2.2.3.2 Paramagnetic Materials

The second class of magnetic materials are the paramagnetic materials. Paramagnetic materials are materials that have no initial magnetization, respond linearly and positively to an applied magnetic field, and have no magnetization upon removal of the applied field. These materials have unpaired electrons in its atomic structure. This means that every atom has an associated magnetic moment. Upon application of an applied magnetic field, these magnetic moments align with the field. If there were no opposing forces or if the field was sufficiently large, all of the atomic moments would align and the magnetization of this material could be quite large. However, due to thermal energy, some of the magnetic moments remain randomly aligned. This leads to a small but positive susceptibility for paramagnetic materials. Because of the thermal agitations, the susceptibility in paramagnetic materials is dependent on temperature. An example plot of the magnetization of a paramagnetic material as a function of applied magnetic field is shown as Figure 2.7b.

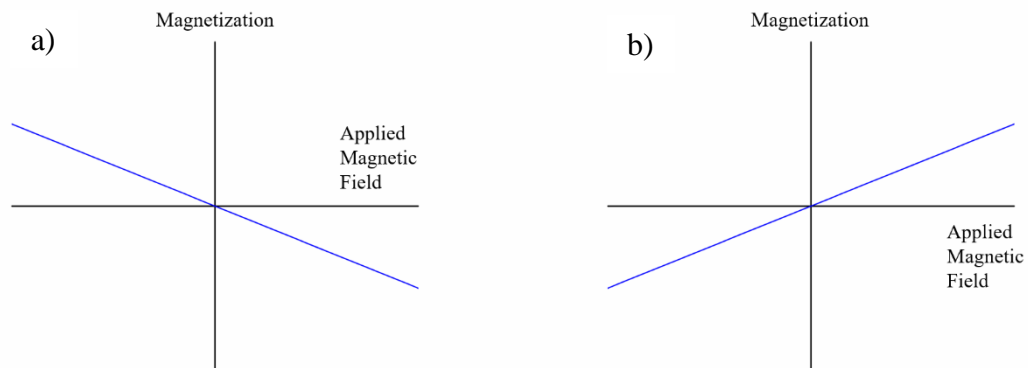


Figure 2.7 These are example plots of the magnetization as a function of applied magnetic field for a) a diamagnetic material and b) a paramagnetic material.

2.2.3.3 Ferromagnetic Materials

The third class of magnetic materials are known as ferromagnetic materials. These materials, similar to paramagnetic materials, have unpaired electrons, each atom has an associated magnetic moment, and the susceptibility is dependent on the temperature. Unlike paramagnetic materials, these magnetic moments can align spontaneously and are not randomized by thermal agitations. This is because the unpaired electrons have an exchange force acting between them. This exchange force acts to align the magnetic moments of each electron. Once the temperature is high enough, the Curie temperature, the thermal agitations begin to take over and ruin the cooperative alignment of magnetic moments. Once the Curie temperature is reached, the material becomes paramagnetic. In ferromagnetic materials, all of the unpaired electrons for nearest neighbor atoms have magnetic moments that are aligned parallel to one another. However, it is common to see ferromagnetic materials, like iron, that are not magnetized. The reasoning behind this is that within a localized area in the ferromagnetic material, all of the spins of the unpaired electrons align parallel. However, to reduce the amount of energy in the system, the material will divide into regions called domains.

2.2.4 Magnetic Domains

Within a domain, all of the unpaired electrons spins are aligned parallel. This domain then has a magnetization in some direction as shown in Figure 2.8a. To reduce the amount of energy, a second domain will form in close proximity to the first domain whose magnetization direction will allow for a closed magnetic loop within the material as shown in

Figure 2.8b. Further reductions in energy can be made by continuing to divide into smaller and smaller domains such that the net magnetization of the material is zero as shown in Figure 2.8c. There does exist a limit to which a ferromagnetic material will divide into more domains. At some point, the energy reduction in the creation of new domains is outweighed by the energy necessary to create them. The border between domains is known as a domain wall. It is a region where the alignment of the electron spins continuously changes from the orientation in domain 1 to the orientation in domain 2. The amount of energy for this domain wall is known as the domain wall energy and is one of the balancing factors for the creation of a new domain and the retention of the current domain structure.

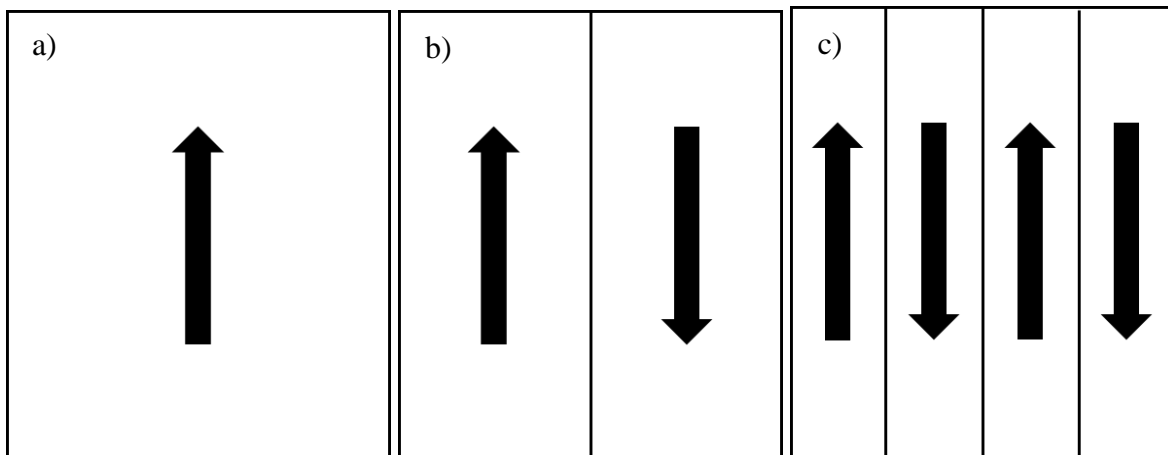


Figure 2.8 This is a schematic of the domain structure of a ferromagnetic material in order to reduce the overall energy of the system.

During the application of a magnetic field to a ferromagnetic material, the magnetization of the material changes based on two main mechanisms: domain-wall motion and domain rotation. Using iron as an example, at low applied magnetic fields, the domains whose magnetization align with the applied magnetic field are of lower energy than any other domains in the system. This applied field then acts to increase the total energy in the system.

To reduce this energy, the magnetic moments at the domain walls (where the magnetic moments continuously rotate from one domain orientation to the next) of the domains aligned with the magnetic field will begin to rotate. This rotation effectively looks like domain-wall motion as the boundary begins to shift. As the domain-walls continue to move, the number and size of the other domains will decrease until saturation is reached where there will exist only one domain. Domain rotation is a phenomenon that typically occurs at higher applied magnetic fields. During domain rotation, domain-wall motion has ceased and to further reduce the energy in the system, the magnetization of the remaining domains must flip. Why domain rotation would occur over domain-wall motion will be explained later.

2.2.5 Ferrimagnetic and Antiferromagnetic Materials

In the ferromagnetic materials class, there exist two other kinds of magnetic materials known as ferrimagnetic and antiferromagnetic materials. Unlike in ferromagnetic materials, ferrimagnetic and antiferromagnetic materials have magnetic moments that are antiparallel. In ferrimagnetic materials, these antiparallel moments are not enough to fully cancel the other magnetic moments and as a result, a net magnetization still exists. In antiferromagnetic materials, the antiparallel moments are enough to fully cancel the other magnetic moments and as a result, no net magnetization exists. An example schematic is shown as Figure 2.9.

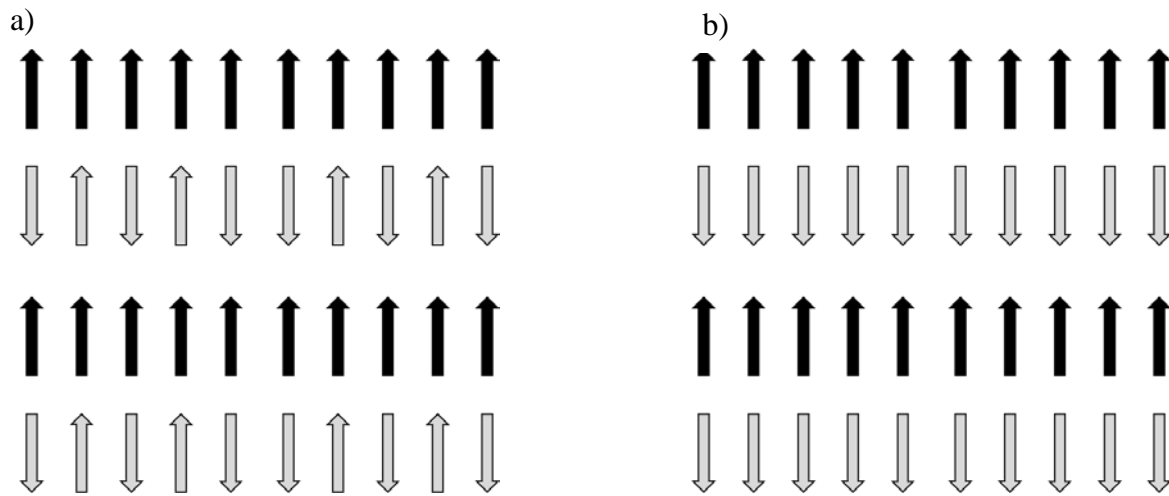


Figure 2.9 These are schematics of the moments of a) ferrimagnetic materials and b) antiferromagnetic materials.

2.2.6 Measurements of Magnetic Materials

Examples of the magnetization versus applied magnetic field for diamagnetic and paramagnetic materials have already been shown as Figure 2.7a and 2.7b, respectively. The magnetization is non-linear for a ferromagnetic material. An example plot of the magnetization as a function of applied magnetic field for a ferromagnetic material is shown as Figure 2.10 (from Cullity and Graham [18]) which is called a hysteresis curve. In this plot, several important points in the curve are marked. In this plot, B_r is the remanent magnetization, H_c is the coercive field, and B_s is the saturation magnetization. The saturation magnetization is an intrinsic property whereas the remanent magnetization and coercivity are extrinsic and can depend on grain structure and geometry. The total area inside the hysteresis curve is a measure of the amount of energy loss inside of the magnetic material.

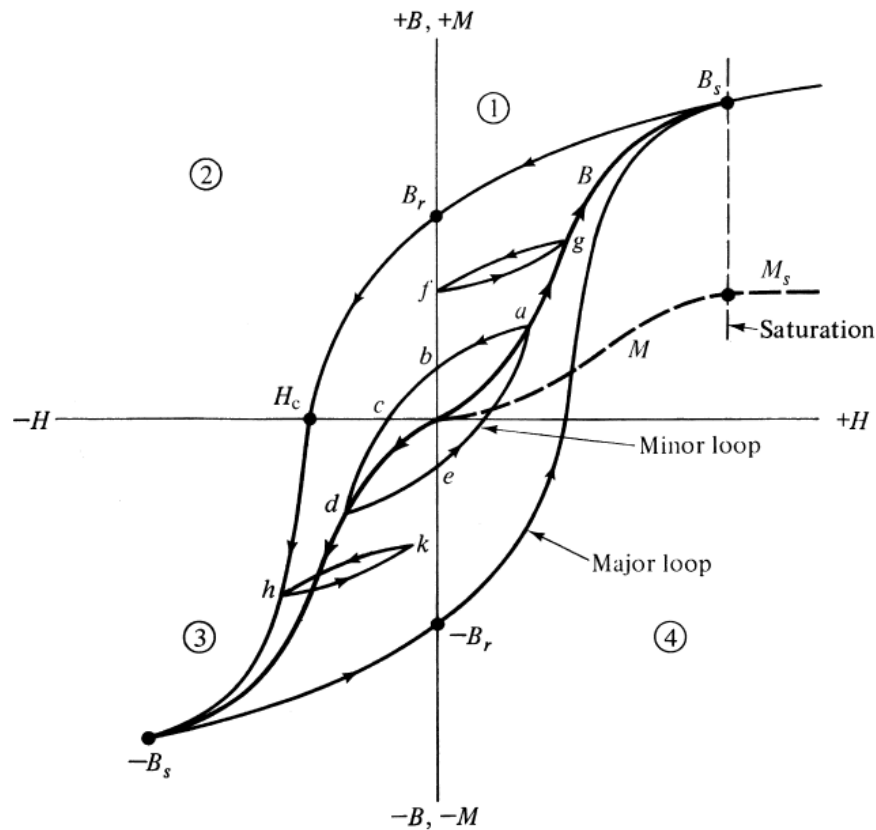


Figure 2.10 This is a schematic of the magnetization as a function of applied magnetic field for a ferromagnetic material. The points of saturation, remanent, and coercive fields are marked.

2.2.7 Mechanism Behind Ferromagnetism

Within ferromagnetic materials, one of the main drivers behind the coupling between electrons is due to the exchange interaction between electrons from neighboring atoms. Because electrons are indistinguishable to one another, electrons can interchange between atoms at high frequencies. This interaction between the two electrons can also lead to an exchange integral between the two electrons, J_{ex} . When this exchange integral is positive, the energy between the electrons is at a minimum when the electron spins are parallel and a maximum when they are antiparallel. The opposite is true when the exchange integral is

negative. A positive exchange integral is a necessary condition for ferromagnetism though not a sufficient condition. The magnitude of the exchange integral is also influenced by the distance between neighboring atoms. If r_a is the atomic radius and r_{3d} is the radius of the 3d electron shell, the ratio r_a/r_{3d} decreases as the atoms are brought closer together if the 3d shell radius stays the same. As this ratio decreases, the electrons are brought closer together which drives the exchange interaction up until a certain point at which further decrease in this ratio actually causes the exchange integral to become negative. A schematic of a Bethe-Slater curve is shown as Figure 2.11 [18]. This shows how the ratio between the atomic radius and the 3d electron shell affects the exchange integral for some of the first row transition metals.

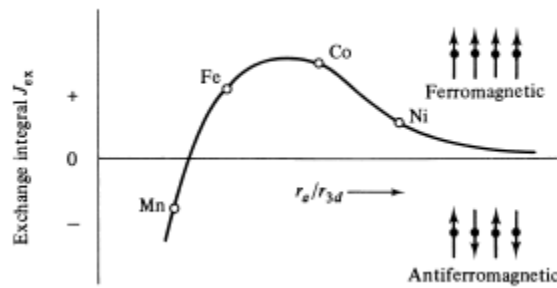


Figure 2.11 This is a plot of the exchange integral as a function of the ratio of atomic radius to the radius of the 3d orbital. Several 1st row transition elements are shown.

2.2.8 Magnetocrystalline Anisotropy

For magnetic materials, it is easier to magnetize some crystalline directions than others.

Assuming a single crystal of a ferromagnetic material, the applied magnetic field necessary to fully magnetize the sample is dependent upon the orientation of the crystal relative to the applied magnetic field. This is known as magnetocrystalline anisotropy. If the crystalline direction is easily magnetized, that family of directions is known as the easy axis.

Conversely, if the direction is difficult to magnetize, that family of directions is known as the hard axis. A schematic for the magnetization as a function of applied field of the same material along the easy axis and the hard axis is shown as Figure 2.12 [18]. The amount of energy required to rotate the magnetic domains in the material is known as the magnetocrystalline anisotropy energy. If it is difficult to magnetize a material along a particular direction (i.e. it requires a lot of applied magnetic field), the magnetocrystalline anisotropy energy is high. Depending on the application it is either necessary or unwanted to have a material with high magnetocrystalline anisotropy. The ferrites tend to have low magnetocrystalline anisotropy. With the exception of cobalt containing ferrites, the amount of energy required to fully magnetize these materials is low. A quick way to estimate the easy and hard axes of cubic magnetic materials is to minimize the energy equation. The equation is shown as $E/V = K_1(m_1^2m_2^2 + m_2^2m_3^2 + m_3^2m_1^2) + K_2m_1^2m_2^2m_3^2$ where K_1 and K_2 are anisotropy constants and m_1 , m_2 , and m_3 are the unit vector quantities along the applied field direction. It has been shown that the easy axis in nickel ferrite is $\langle 111 \rangle$ and the easy axis in cobalt ferrite is $\langle 100 \rangle$ [19].

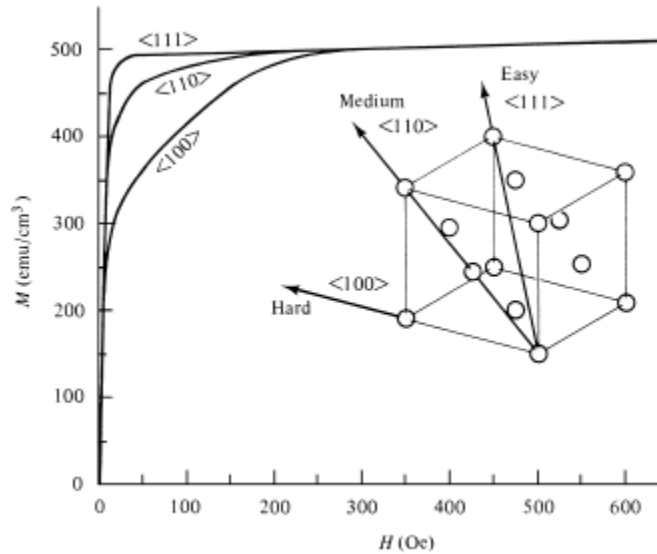


Figure 2.12 This is a schematic of the magnetization of a material along its easy, medium, and hard axes.

As mentioned previously, a ferromagnetic material is magnetized by either domain-wall motion or domain rotation. Assuming a material with high magnetocrystalline anisotropy energy, the application of a small magnetic field may not be enough to cause all domains to be magnetized in the same direction. This is due to the hard axes which may be aligned in the direction of the applied magnetic field. With a sufficiently high applied magnetic field, the remaining domains would rotate in the direction of the magnetic field which would cause the material to reach saturation magnetization. As a consequence, the dimensions of the material would change due to this magnetocrystalline anisotropy.

Magnetocrystalline anisotropy also plays a role in determining whether a magnet is defined as a hard magnet or a soft magnet. A hard magnet is a ferromagnetic material that retains most of its magnetization after removal of an applied magnetic field. By contrast, a soft magnet is a ferromagnetic material that does not retain its magnetization after the applied

magnetic field is removed. A hard magnetic material, therefore, has a high magnetocrystalline anisotropy. Additionally, hard magnets tend to have high coercivity, high eddy current losses, low permeability, and large hysteresis loops. Soft magnetic materials are ferromagnets with low magnetocrystalline anisotropy, have low eddy current loss, high permeability, and very small hysteresis loops.

2.2.9 Magnetostriction

Magnetostriction is the response of any pure substance to an applied magnetic field via strain. The magnetically induced strain is represented by the variable λ and is defined as

$$\lambda = \frac{\Delta l}{l}$$

Equation 2.12

where l is the length of the material. For most materials, this effect is so small (for weakly magnetic materials, a strain of 10^{-7} at really strong fields is observed) that it is of very little concern. However, the effect can be more pronounced in strongly magnetic materials. In ferromagnetic (and ferromagnetic and antiferromagnetic) materials at saturation magnetization, the strain can reach a maximum value denoted λ_s due to the complete alignment of the unpaired electron spins. As mentioned earlier, one of the origins of the larger magnetostriction observed in ferromagnetic materials is due to their magnetocrystalline anisotropy. As an example, the easy axis of iron is the $\langle 100 \rangle$ direction and the hard axis is the $\langle 111 \rangle$ direction. If a polycrystalline iron sample were placed into a magnetic field, H_1 , with the domain structure and microstructure, as shown by Figure 2.13,

the domain-walls would begin moving until state 2 is reached. At this point, the amount of energy required to change the remaining domain to align with the applied magnetic field would require more energy. This is accomplished by increasing the magnetic field to H_2 . The remaining domain would then flip causing a strain to occur across the length of the material. This schematic is overly simplified and many other factors are at play with magnetostriction but it gives a good demonstration into what magnetostriction looks like and how magnetocrystalline anisotropy plays a role into this phenomenon. For a full look into the mathematical proofs for this effect, the derivation for cubic ferromagnets has been published [20].

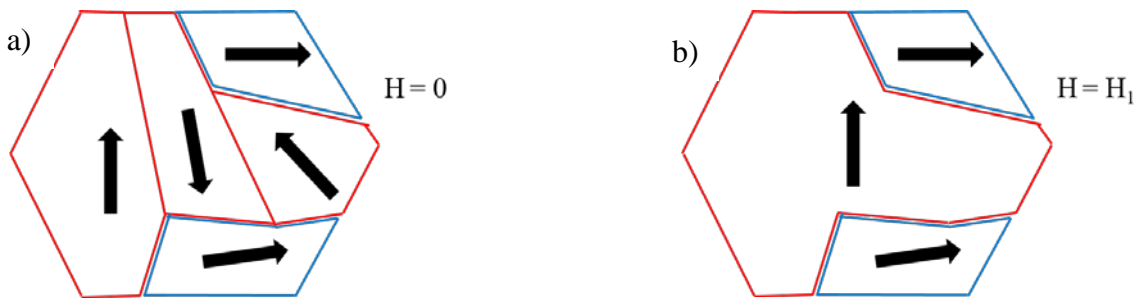


Figure 2.13 This is a schematic of the domain structure of a block of iron. The domain walls align with the grain boundaries. The grains marked in red have the 100 axis pointing vertically. The grains marked in blue have the 111 axis pointing vertically. The image on the left is state 1 (no applied magnetic field). The image on the right is state 2 (magnetic field pointing vertically).

2.3 Magnetoelectricity

2.3.1 Magnetoelectric Effect

The magnetoelectric effect is a materials phenomenon where an electric field can induce magnetization in a sample and its converse. This effect is mediated through strain. The mathematical derivation behind the coupling between the mechanical-electric-magnetic

responses in magnetoelectric materials for a linear approximation is given by the set of equations shown below.

$$\sigma = cS - e^T E - q^T H$$

Equation 2.13

$$D = eS + \varepsilon E + \alpha H$$

Equation 2.14

$$B = qS + \alpha^T E + \mu H$$

Equation 2.15

where σ , S , D , E , B , and H are the stress, strain, electric displacement, electric field, magnetic induction, and magnetic field, respectively. The variables c , ε , μ , e , q , and α are the stiffness tensor, relative permittivity tensor, permeability tensor, piezoelectric coefficient tensor, piezomagnetic coefficient tensor, and magnetoelectric coefficient tensor, respectively. The T's in the equation represent the transpose of the tensor. This set of equations relates the mechanical, electrical, and magnetic behavior in a magnetoelectric system. These equations assume the magnetic portion of the magnetoelectric is piezomagnetic, which is not often true. This distinction will be covered later. Further analysis will not be done here.

2.3.2 Magnetoelectric Materials

The uses for materials that exhibit magnetoelectric behavior include sensors, memory devices, transformers, resonators, and optical devices [21]. The magnetoelectric effect was theorized to exist in the oxide Cr_2O_3 in 1959 [22] and was experimentally verified in 1960 [23]. In this oxide, the piezoelectric behavior (from being a ferroelectric) couples with the

piezomagnetic behavior (from being antiferromagnetic). Few single phase materials exist which show the magnetoelectric effect. This is due to the competing mechanisms by which ferromagnetism and ferroelectricity exist. For the majority of materials that exhibit ferroelectricity, the crystal structure is perovskite. In this crystal structure, the nearest neighboring ions have a hybridized electron structure. If the ions have empty d-orbitals in this hybridization, the structure tends to be non-centrosymmetric. The empty d-orbital is in direct conflict with an almost necessity for ferromagnetism which is unpaired electrons in the d-orbital. There do exist, however, a few materials which have both ferromagnetism and ferroelectricity. To understand how single phase multiferroics can exist in light of the seemingly contradictory requirements, several mechanisms have been proposed which will not be covered. Since the time of discovery of magnetoelectricity in Cr_2O_3 , much study has been devoted to single phase materials which exhibit the magnetoelectric effect [24]–[27]. The issue with single phase magnetoelectrics is the weakness of its effect. The strength of the magnetoelectric effect is summarized by a value which is given by the variable α_E with has the units $\text{V Oe}^{-1} \text{ cm}^{-1}$. For single phase materials, the greatest magnetoelectric voltage coefficient seen is around 3 V/Oe.cm [28].

2.3.3 Piezomagnetism

Before delving into magnetoelectric composites (which have been studied due to their ability to couple well and increase the magnetoelectric voltage coefficient), it's important to note that the magnetoelectric effect is defined as the coupling between the piezoelectric and piezomagnetic effects in materials. Piezoelectricity (as briefly covered previously) involves

the induction of a polarization by an applied stress and, conversely, the induction of a mechanical strain by application of an electric field. This comes from the breaking of space-inversion symmetry due to the non-centrosymmetry in the crystal structure. Additionally, as noted before, the piezoelectric effect is seen in all ferroelectric crystals and even crystals which do not exhibit ferroelectricity. The piezomagnetic effect, by corollary to the piezoelectric effect, is the induction of a magnetization in a material by application of a mechanical stress and, conversely, the induction of a mechanical strain by application of a magnetic field. The origins of this are from the breaking of time-inversion symmetry. By contrast to piezoelectric materials, piezomagnetism is not seen in all ferromagnetic materials. This is because the mechanism by which magnetism exists is from the positive exchange interaction between electron spins in neighboring atoms. Although crystal structure plays a role (see the Bethe-Slater curve in section x), the origins of the positive exchange interaction is not merely from symmetry or crystal structure. The origins behind piezomagnetism, though, are directly related to the crystal symmetry. This effect is not nearly as well covered in the literature due to its uncommonness. It is known that piezomagnetism linearly couples stress/strain to magnetization/applied magnetic field. Additionally, a magnetic moment can be produced by mechanical strain alone in zero magnetic field. Although uncommon, piezomagnetism has been seen in the materials Cr_2O_3 [23] and Mn_3GaN [29]. To achieve the magnetoelectric effect in composites, magnetostrictive materials have been used instead.

2.3.4 Magnetoelectric Composites

To achieve a greater magnetoelectric effect to be used in devices, magnetoelectric composites have been used. This involves combining a piezoelectric material with a piezomagnetic (or magnetostrictive) material in a singular sample. There exist three main orientations for the combination of these two material classes: 0-3 structure, 2-2 structure, and the 1-3 structure. The 0-3 structure is particles of one phase existing in a matrix of the second. The 2-2 structure is a layered laminate structure where the phases exist in stacks. The 1-3 structure is columnar or fiber-like grains of one phase existing in a matrix of the second. Because all ferroelectric materials are piezoelectric, ferroelectrics tend to be used as the piezoelectric in the system. For the magnetic material, a piezomagnetic linearly couples the stress/strain with the magnetization/applied magnetic field which a magnetostrictive material couples the stress/strain and magnetization/applied magnetic field non-linearly. While this makes device application more difficult, the benefits far outweigh the detractions. One of the first composite magnetoelectric composites made combined the ferroelectric barium titanate and the ferrimagnetic cobalt ferrite. This composite produced a magnetoelectric voltage coefficient of 0.13 V/Oe.cm [30]. Since that time, further research into the composites has been done. The ferroelectric systems studied for the composites include PZT ($\text{Pb}(\text{ZrTi})\text{O}_3$), PMN-PT ($\text{Pb}(\text{MgNb})\text{O}_3\text{-PbTiO}_3$), PVDF (poly(vinylidene fluoride-trifluorethylene)), and BTO (BaTiO_3), among others. These materials are chosen for the electrical part due to their high piezoelectric coefficients. For the magnetostrictive materials used in magnetoelectric composites, the ferrites and Terfenol-D have been studied. The main ferrites of study have been nickel ferrite and cobalt ferrite. Terfenol-D is a metallic alloy with chemical formulae

of $\text{Tb}_x\text{Dy}_{1-x}\text{Fe}_2$. Each of these materials has their own unique advantages and disadvantages. Nickel ferrite is a material with a fairly high Curie temperature, high resistivity, and a decent magnetostrictive coefficient. Cobalt ferrite has a slightly lower Curie temperature, similar resistivity, and a large magnetostrictive coefficient. Terfenol-D has an extremely large magnetostrictive coefficient, low resistivity, and a lower Curie temperature than either CFO or NFO. One of the main disadvantages to using nickel ferrite for the magnetostrictive layer is its lower magnetostrictive coefficient. CFO has an order of magnitude high magnetostrictive coefficient while the MS coefficient of Terfenol-D is two orders of magnitude higher [21]. However, the high resistivity of nickel ferrite means eddy current losses will not occur with this material and its high Curie temperature means it can be used in applications not able to be achieved in materials with lower T_c . Additionally, nickel ferrite couples extremely well with PZT [31]. Cobalt ferrite has a fairly large magnetostrictive coefficient, high Curie temperature, and high resistivity. Because of these properties, cobalt ferrite is well suited for all of the applications that NFO could be used in while maintaining a higher sensitivity to magnetic fields. However, it's been difficult to interface this material with PZT like NFO is able to do [31]. Terfenol-D has an enormous magnetostrictive coefficient with a reasonably high Curie temperature ($\sim 380\text{--}430^\circ\text{C}$) [32] which makes this material really promising for use as the MS layer. However, it has a low resistivity which means there will be large eddy current losses in this material. Additionally, Terfenol-D is extremely brittle which means it has been more heavily integrated into the polymer-based piezoelectrics [33]; eliminating the need for high Curie temperature.

2.4 Ferroelectric Random Access Memory

2.4.1 Computer Memory Basics

As computer usage is higher today than ever before, the need for computer memory that has good data retention, fast read/write speed, low cost, and good reliability is more important now than ever. Historically, computer CPUs (central processing units) have written data that needs to be quickly and immediately accessed onto RAM (random access memory) which can be read and written to at speeds comparable to the running speed of the CPU (10s of ns). Here, RAM is defined as memory that operates at speeds comparable to that of the CPU. Random access memory is typically volatile, i.e. when power to the memory is cut, the data are lost. When data does not need to be immediately accessed by the CPU, data is typically written to non-volatile memory (NVM). Non-volatile memory is defined as memory that has the capacity to retain data for at least 10 years. Hard drives today are NVMS and are either FLASH based (~1 ms read/write time) or magnetic bit based (1s-10s of ms read/write time). These operational times are orders of magnitude slower than that of the CPU running speed. This leaves a gap for memory that is both non-volatile and can run at the operating speeds of computer CPUs. To fill this gap, ferroelectric memories have been heavily studied.

2.4.2 Ferroelectric Memory

The use of a ferroelectric for computer memory takes advantage of the materials ability to have two polarization states. If this material is integrated into a capacitor-type structure (the ferroelectric thin film sandwiched between two similar metal electrodes), the ferroelectric film can be polarized in the up or down state normal to the plane of the film. The up or down

state would correspond to a 1 or 0, respectively, which is the basis for computer memory. Ferroelectric memories were theorized several decades ago and devices integrating them have been built since the 1980s. The simplest way that ferroelectric capacitors can be integrated into computer memory is through a 1T1C architecture. An example schematic is shown below as Figure 2.14. In this setup, the BL stands for bit line, PL stands for plate line, and WL stands for word line. In this configuration, the ferroelectric capacitor stores the bit by the direction of its polarization. The BL is used to read the state of the capacitor. The WL is used to open the transistor and access the capacitor. To write a new bit to the ferroelectric, a $+V$ would cause the ferroelectric to go into its $-P_r$ while a $-V$ pulse would cause the ferroelectric to go into its $+P_r$. To read the existing bit, a switching voltage must be applied to the capacitor, measure its output current via a load resistor, send the signal to a sense amplifier and determine whether the displacement current is large (the ferroelectric switched) or small (the ferroelectric did not switch). This read process ends up destroying the original data in the ferroelectric capacitor. The process then involves rewriting the data to the capacitor that was just read. This is known as a destructive read process and is one of the main drawbacks for utilizing this architecture in FeRAM widely.

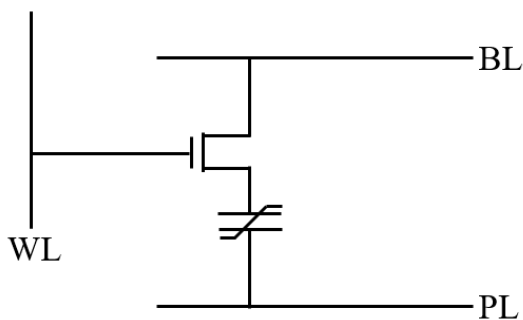


Figure 2.14 This is a schematic of the 1T1C FeRAM. The initialism BL stands for bit line, PL for plate line, and WL for word line.

Some ways of mitigating this are to use different FeRAM architectures. Some examples are the 2T2C (schematic shown as Figure 2.15) and the 6T4C. In the 2T2C, two ferroelectric capacitors and two transistors are used. This architecture has the advantage of being able to reduce the amount of imprint-retention that the capacitors will have seen. This is because complimentary signals will be written across each capacitor which will give an imprint-retention across one capacitor while the other will get a non-imprint-retention signal. The 2T2C architecture also maximizes the sensed voltage and ensures a more stable read-out. The 6T4C architecture, discovered by S. Masui et al [34], combines six transistors with four ferroelectric capacitors. This architecture is advantageous in that this architecture has an unlimited lifetime (lifetime of more than 10 years with constant read/write cycles on the capacitors) and its access time is much faster than that of the 1T1C and the 2T2C architecture. The main issue with the 2T2C and 6T4C is that the bit density is much lower than that of the 1T1C. Although advantageous, within the same sized memory package, the memory density would be significantly lower.

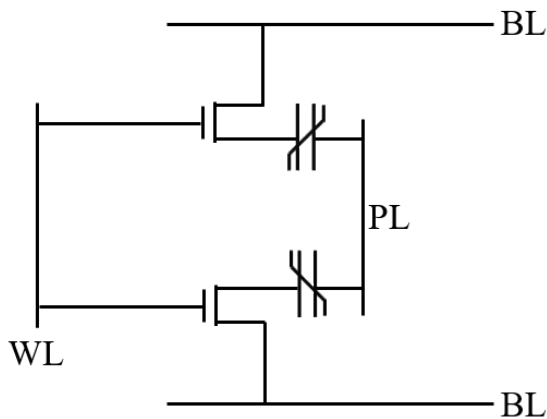


Figure 2.15 This is a schematic of the 1T1C FeRAM. The initialism BL stands for bit line, PL for plate line, and WL for word line.

Today, flash based memories are widely used due to their increased speed over the traditional hard disk drives used a decade ago. Therefore, any new memory that hits the market must compete (and have advantages that outweigh) with the speed of the flash memory. The table shown below as table 2.1 gives a rough comparison of the flash memory, SRAM (static random access memory), DRAM (dynamic random access memory), and the FeRAM. This table is adapted from [15].

Table 2.1 This table shows the properties of several memory types in use today.

Memory Type	Endurance	Access Time	Data Retention	Standby	Cell Size
Flash	$\sim 10^5$	ms	10 years	$< 1 \mu\text{A}$	~ 1
SRAM	unlimited	ns	10 years	$> 1 \mu\text{A}$	~ 6
DRAM	unlimited	ns	ms	$> 10 \mu\text{A}$	~ 1
FeRAM	unlimited	ns	10 years	$< 1 \mu\text{A}$	1-6

This table shows that each memory type has its own advantages and disadvantages. In particular, the main disadvantage to the FeRAM is the cell size necessary to achieve unlimited endurance and high data retention. This is due, in part, to the destructive read process in these cells.

2.5 Materials

2.5.1 Hafnium Oxide

Hafnium oxide (hafnia or HfO_2) is a binary oxide system which has garnered much interest over the last several decades for a variety of reasons. One of the more obvious uses of this material is as a refractory, inert material to protect more reactive materials due to its high melting temperature (2758 °C). More recently, the research on this material has been focused on its optical and electrical properties.

Some investigations [35] into the phase of the material lead to a pressure/temperature phase diagram that shows, as temperature is increased at standard pressure, a $P2_1/c$ monoclinic phase, a $P4_2/nmc$ tetragonal phase, and a $Fm\bar{3}m$ cubic phase. With higher pressures, the phases present were a $Pbca$ orthorhombic and a $Pnma$ orthorhombic phase. At least one additional phase of hafnia has been discovered with the discovery of ferroelectricity in hafnium oxide. The main phase is the $Pca2_1$ phase. A second orthorhombic phase is theorized to be the $Pmn2_1$ phase.

One of the biggest drivers for research on hafnia thin films is in the search for a replacement gate dielectric for silicon dioxide in CMOS transistors. The need for a replacement is due to large leakage currents that flow through this gate dielectric because of its thickness (1.4 nm). The gate dielectric layer thickness was consistently reduced to increase the capacitance in the transistor gate. Because the thickness has reached such a critical level (where the probability of tunneling electrons becomes large), a material with a higher dielectric constant is needed

to achieve the same capacitance at larger thicknesses. Research for new high-k dielectric materials led, eventually, to hafnium dioxide. This is because this material has a relatively high dielectric constant (16 for the monoclinic phase, 28-70 for the tetragonal phase, and 26-29 for the cubic phase [1]), is thermodynamically stable with Si, is insulating, forms a good electrical interface with Si, has few bulk electrically active defects, and is kinetically stable with current processing parameters [36]. In this context, high is as compared with the current standard gate dielectric used for computers. The desire for using hafnium oxide as the gate dielectric was to use the amorphous phase or to use a nano-crystalline high symmetry phase. The reasoning for the former was to lower the magnitude of leakage current and the latter due to its higher dielectric constant. However, only dopants were found to achieve the high symmetry phases of hafnia in thin film form [1] until very recently [37].

From this research, a ferroelectric phase of hafnia was discovered in 2011 [38] by doping it with small amounts of silicon. Since that time, much research has been devoted into trying to understand the structure [39], [40], modeling the phase [35], [41], and finding the dopants that best optimized the properties [4], [5]. Although this material does not have the highest piezoelectric response to applied fields [38], [42], its ability to be cycled up to 4 MV/cm and exhibit ferroelectric properties down to 10 nm makes this material extremely useful for applications in the ferroelectric-based memory. Most of the synthesis of ferroelectric hafnia has been done using vacuum based deposition techniques including ALD [6], [43], [44] and sputtering [45]. There have been a few reports that have found that ferroelectric hafnia can be

grown via chemical solution deposition (the technique is covered later) with various dopants [5], [7], [46].

2.5.2 Ferrites

Ferrites are iron oxide materials typically used in some magnetic capacity (although their usefulness in antennas [47], catalysts [48], and gas sensors [49] cannot be ignored). Today, two main crystal structures of the ferrites are researched: the cubic spinel phase and the hexagonal phase, known as hexaferrites. Of focus for the remainder of this paper is the cubic spinel phase. The chemical formula for the cubic spinel ferrites is MFe_2O_4 where M is typically a transition metal and can be many different metal cations in the same system. To date, Li [50], Al [51], Zn [52], Co [53], Ni [54], Cu [55], Mg [56], Gd [57], Y [58], and Mn [59](among others) have been looked into for the metal cation. Depending on what metal is chosen, the structure will vary between spinel and inverse spinel. A spinel structure is where the oxygen atoms comprise an FCC lattice, the M atoms sit on the tetrahedral sites, and the iron atoms sit on the octahedral sites. In inverse spinel, the oxygen still comprises the FCC lattice while the M atoms sit on the octahedral sites, and half of the iron atoms sit on the tetrahedral and the other half on the remaining octahedral sites. Ferrites tend to be ferrimagnetic materials. For both nickel ferrite, the crystal structure is inverse spinel. This means that the nickel atoms tend to sit on octahedral sites while half of the iron atoms sit on tetrahedral sites and the other half sit on octahedral sites. The magnetic moments of the iron atoms on the octahedral sites cancel out the magnetic moments of the iron atoms on the

tetrahedral sites. As a result, within NFO, the magnetism in the system is coming entirely from the moments of the nickel.

Table 2.2 compares some of the properties of a few well studied ferrites and a few well studied metal ferromagnets.

	NiFe ₂ O ₄ [60]–[63]	CoFe ₂ O ₄ [64]–[67]	Fe ₃ O ₄ [68]	Fe [69]	Ni [69]
ρ (g/cc)	5.38	5.26	5.18	7.87	8.91
ρ (Ω cm)	10^6	10^6	10^{-3}	10^{-9}	10^{-9}
T_c ($^{\circ}$ C)	592	490	577	771	355
λ_s (10^{-6})	-21	-164	35	-7	-35
M_s (emu/g) (300 K)	55	69	92	217	55
M_s (emu/cc) (300 K)	296	363	474	1710	488

Of these magnetic materials, nickel ferrite and cobalt ferrite have been among the most highly studied for use in magnetoelectric composites. This is due to their relatively high Curie temperature and their high resistivity. The former property allows their use in a variety of applications even into the higher temperature regime where the latter property allows for fewer losses through eddy currents. Additionally, these materials have a lower density than the metallic ferromagnets which allows for weight savings when these materials are packaged. Among the materials shown in the table, cobalt ferrite has the largest magnetostriction which will tend to give a higher magnetoelectric constant. However, nickel ferrite tends to couple better with the titanate materials. This has led to the large study of these two magnetic materials for the magnetostrictive layer of the heterostructure.

2.6 Chemical Solution Deposition

Chemical solution deposition (CSD) is a broad term describing using a chemical solution to deposit thin films of material onto a substrate. Typically, these films are oxides [7], [70], [71] although polymers have also been deposited via CSD [72]. This technique is typically done in one of two ways: dip coating and spin coating. Spin coating involves putting a substrate onto a spin coater, holding that sample in place, dropping solution onto the surface, and spinning the substrate at a set speed for a set time at a set acceleration. The solution used tends to be a mixture of large organic ligands that bond to the metallic ions and the solvent. The viscosity of the solution plays an important role as more viscous solutions will tend to deposit thicker films. During the process, most of the solution is spun off of the surface. As the solution is spun on the substrate, a balance between the outward force on the resin is balanced by how quickly the solution is drying. Due to the increasing surface area to volume ratio, the solution tends to dry more and more quickly as the film thins. The process of drying causes the viscosity of the film to increase which counteracts the centrifugal force. For spin coating, several parameters can be varied to affect the thickness and quality of the deposited film. These include but are not limited to: spin speed, spin acceleration, substrate composition, spin time, number of spin cycles, and exhaust air flow. Spin coating has been used by groups to do deposition of both ferroelectrics [7], [73]–[75] and ferromagnets [54], [76]. This deposition technique has advantages in its flexibility with stoichiometric variation. Where vacuum-based deposition techniques depend heavily on the plasma and plume kinetics as well as the deposition pressure, gas mixture, target to substrate distance and angle, power density, temperature, cleanliness, deposition rate, and target purity, chemical solution

deposition allows for flexibility with substrate and chemical stoichiometric changes. Some of the major drawbacks of chemical solution deposition are the necessity to find solvents that wet the desired substrate well and its limitation to depositing oxide and polymer-based films.

CHAPTER 3

INSTRUMENTATION

3.1 GIXRD

The primary method for evaluating the phase of the synthesized films was through grazing incidence x-ray diffraction (GIXRD). In standard Bragg-Brentano geometry XRD, a divergent x-ray beam strikes the surface of the sample at an angle (ω) from the plane of the sample. The x-rays will, if in Bragg condition, strike the sample and constructively interfere producing intense regions of diffracted x-rays. If the detector is a point detector, the detector will collect the diffracted x-rays from a position co-planar to the sample and source and at an angle 2θ from the line of the source x-rays if they fully transmitted through the sample. If the XRD is in standard Bragg-Brentano geometry, (ω) will be equivalent to half of 2θ . A schematic for the description above is shown as Figure 3.1. The Bragg condition is fulfilled when the incident x-rays strike the sample and the diffracted x-rays constructively interfere as described by equation 3.1

$$n \lambda = 2d \sin\theta$$

Equation 3.1

where λ is the wavelength of the x-rays, d is the spacing of the lattice planes, θ is the angle between the plane of the sample and the diffracted beam, and n is some integer multiple. In standard Bragg-Brentano geometry, the source and detector will move together to maintain the same angular relationship to the sample plane normal. The result is that, in theory, the only information on lattice spacing that can be collected using this geometry is if the crystal planes are parallel to the sample surface. A schematic of this is shown as Figure 3.2 a.

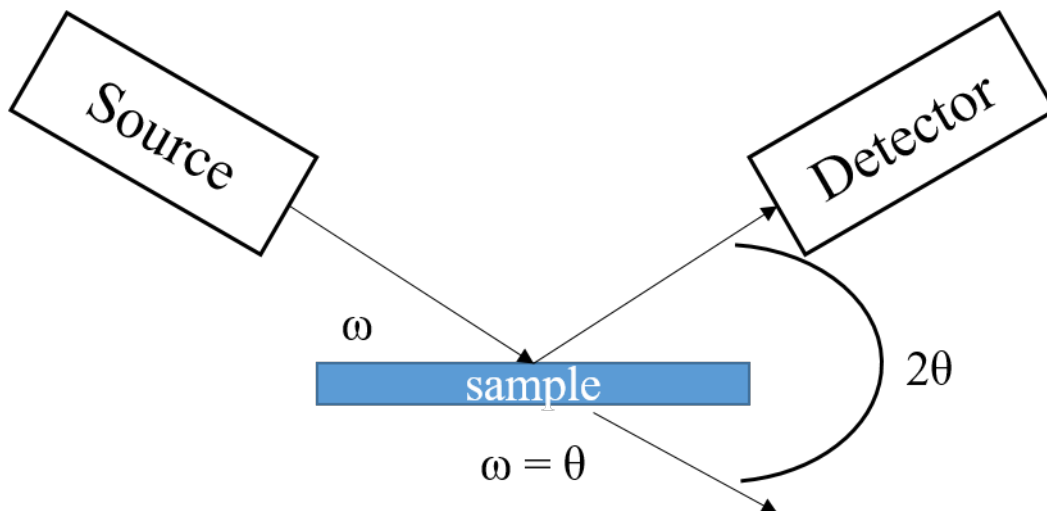


Figure 3.1 This is a schematic for standard Bragg-Brentano geometry x-ray diffraction. Marked are angles described using this technique.

By contrast, GIXRD involves striking a sample with a parallel x-ray beam. The other major difference with GIXRD over Bragg-Brentano geometry is that the source stays fixed at a low incident angle, i.e. (ω) is static. This does not change the fact that Bragg condition must be met for the x-rays to diffract in the sample. The major difference is that crystal planes parallel to the sample surface plane will not diffract in GIXRD. Instead, the crystal planes whose normal bisects the angle between the source and detector are the only crystal planes that will diffract. This tends to heavily reduce the signal that is detected from the substrate which makes this orientation useful for thin film analysis. A schematic of what happens is shown as Figure 3.2 b.

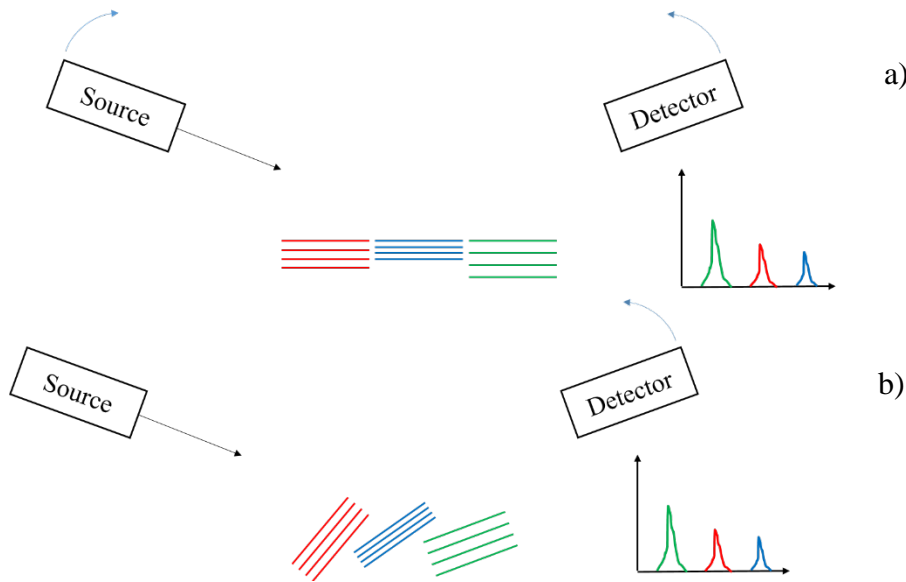


Figure 3.2 Shown are the schematics for where diffraction peaks originate in a) Bragg-Brentano and where the peaks originate from in b) grazing incidence x-ray diffraction.

The other reason that GIXRD tends to work well for thin films is due to the amount of space covered in the thin film as opposed to the substrate of the material. As a simple example, using the data from the NIST website for calculating mass attenuation coefficients in compounds [77] and the equation

$$\frac{\mu}{\rho} = \sum_i w_i (\mu/\rho)_i$$

Equation 3.2

the mass attenuation coefficient for hafnium dioxide is roughly $135 \text{ cm}^2/\text{g}$. To calculate the thickness required to bring the intensity of the x-ray beams in hafnia down to 10 %, the equation

$$\frac{I}{I_o} = e^{[-(\mu/\rho)\rho t]}$$

Equation 3.3

is used where the I/I_o expression represents the fraction of intensity emerging, the μ/ρ expression is the mass attenuation coefficient, ρ is the density, and t is the thickness that the x-rays would penetrate to achieve that drop in intensity. For hafnia, using the density of 9.68 g/cc, the thickness required to achieve a 90 % drop in intensity is 1.76 μm . Using Bragg-Brentano, this would present a problem because the x-ray beam would completely penetrate the thin film and most of the signal would come from the substrate. But, because the source angle is fixed to a low position, an $(\omega) = 1.5^\circ$ with a 50 nm thick thin film of hafnia would mean the incident beam would travel at least 1.91 μm before signal could come from the substrate. This makes GIXRD powerful for acquiring information from the thin film only.

3.2 AFM

To evaluate the roughness of the sample, atomic force microscopy (AFM) was used in tapping mode. This involves tapping a sharp tip across the surface of the sample and, using a laser in combination with a photodiode, recording the topography of the sample surface. This technique is dependent on the quality of the tip used and the accuracy of the photodiode. However, very fine resolution of the surface roughness can be measured with great accuracy. Films that have ~1 nm RMS roughness or less are considered quality thin films. Root mean square (RMS) roughness is calculated via the equation

$$R_q = \sqrt{\frac{1}{n} \sum_{i=1}^n y_i^2}$$

Equation 3.4

where y_i is the difference between the height at a given point i and the mean of all of the points in the image, n is the total number of points measured, and R_q is the RMS roughness value.

3.3 XRR

To confirm the roughness value seen in AFM and to measure the thickness of the thin films deposited, a technique known as x-ray reflectivity (XRR) was used. The geometry for XRR is the exact same as in a Bragg-Brentano XRD experiment except that the incident beam is parallel and not divergent. For XRR, only small angles of (ω) and 2θ are used. When the incident beam angle is small enough, the sample reflects 100 % of the incident beam. As (ω) continues to increase, the beam will penetrate into the sample. The angle at which this happens is known as the critical angle (θ_c). Beyond the critical angle, some x-rays will penetrate into the sample while others will be reflected; as the angle increases, the number of x-rays that penetrate increases. If there exists one thin film on top of a substrate, at an angle larger than the critical angle, some x-rays will fully reflect off of the surface of the sample. Other x-rays will penetrate the thin film and will reflect off of the interface between the film and the substrate. Others still will penetrate fully into the substrate which will be diffracted and not seen by the detector. If the x-rays reflected from the surface are an integral wavelength multiple of the x-rays reflected from the interface, there will be constructive interference and the appearance of a peak in the reflection data. If the difference in path length of these two x-rays is $\frac{1}{2}$ a wavelength multiple, there will be destructive interference and a trough will appear in the reflection data. This periodicity in peaks and troughs is called

Kiessig fringes and determines the thickness of the thin film. This is done by using the Fresnel equation

$$d = \frac{\lambda}{2 \left(\sqrt{(\theta_2^2 - \alpha_c^2)} - \sqrt{(\theta_1^2 - \alpha_c^2)} \right)}$$

Equation 3.5

where d is the thickness of the film, λ is the wavelength of the incoming x-rays, θ_2 is the second fringe, θ_1 is the first fringe, and α_c is the critical angle. All of the angles should be in radians.

Using modeling software, the roughness of the film can be calculated by how quickly the intensity dies off in 2θ space. This technique is not useful for thin films with thickness above about 200 nm (unless the detector is extremely high resolution) nor for films with roughness above about 2-3 nm RMS roughness.

3.4 Electrical Measurements

For the electrical measurements, an LCR meter was used to measure the dissipation factor and the capacitance while a Radiant Technologies Multiferroic/Ferroelectric Test System was used to measure the polarization, transient current, and leakage current. For a good overview of the electrical measurements done on dielectrics and ferroelectrics, see the review by Damjanovic [78].

CHAPTER 4

PROCESSING OPTIMIZATION OF HIGH SYMMETRY

HAFNIA THIN FILMS ON SAPPHIRE

The high symmetry phases of hafnia have higher dielectric constants than the monoclinic phase or amorphous hafnia [1]. Electric field cycling of doped hafnia in the higher symmetry phase (cubic, tetragonal, orthorhombic) has also been shown to induce the ferroelectric phase of hafnia [2]. These higher symmetry phases of hafnia have only ever been achieved using dopants [3]–[5] or from vacuum-based deposition techniques [6]–[8]. To use the high symmetry phases of hafnia for MOSFETs, the film should not have dopants because they tend to create charge imbalances in the oxide. This will cause a shift in the gate threshold voltage which will affect when the transistor turns on [36]. For ferroelectric hafnia, the understanding of processing parameters necessary to achieve high symmetry hafnia may allow for this material to be more well understood and further utilized. In this chapter, some of the processing parameters necessary to synthesize thin films of the high symmetry phases of hafnia will be studied. The main benchmark for success was determining the phase from XRD and/or GIXRD. For deposition parameter optimization, single side polished, 430 μm thick c-cut sapphire wafers were used. This will inform a starting place for the synthesis of the high symmetry phase of hafnia on other substrates and how best to process them.

4.1 Annealing Temperature Study

Based on the phase diagram of hafnium dioxide, the high symmetry phases are produced with high pressures and/or high temperatures [35]. A method for overcoming this is to use

lattice mismatch/quenching the high symmetry phases in place via rapid temperature processing. As a starting place, to synthesize high symmetry phases of hafnium dioxide via chemical solution deposition with no dopants, it was important to first settle on a chemistry to be used for the solution. Based on the dissertation of Benjamin Norris [79], a 1.8 M hafnium oxychloride solution was used for chemical solution deposition. This was made by mixing 4.96 g of hafnium oxychloride octahydrate with 1 g of glycine in 3.6 mL of deionized water. This mixture was covered, stirred, and heated to 115 °C for 75 minutes. After that time, 3 mL of deionized water was added to the solution and allowed to stir for 30 additional seconds. This solution was filtered through a 0.2 μ m PTFE filter and designated as the stock solution.

For the depositions, a 1 cm by 1 cm c-cut sapphire substrate was used. This substrate was cleaned by blowing compressed air over the surface, then deionized water, then methanol, then acetone, and finally methanol. It was then blow dried using compressed air. The substrate was put onto a WS-400-6NPP-lite from Laurell Technologies Corporation spin coater while the hafnium oxychloride solution was statically dropped onto the surface until the entire substrate was covered. The sample was then spun at 6000 rpm for 30 seconds with an acceleration of 1064 rpm/s. The sample was then placed into a preheated tube furnace at varying temperatures for varying times to narrow down the appropriate annealing temperature and time. Each sample was coated twice following the procedure above in order to get the most signal from the XRD. Standard Bragg-Brentano geometry XRD (PANalytical Empyrean X-ray Diffractometer) was used to find the phase of the thin film. The XRD

spectrum is shown below as Figure 4.1. Shown below the diffraction data are the peak positions of the corresponding hafnium dioxide phases. The space groups corresponding to the diffraction peak positions are shown.

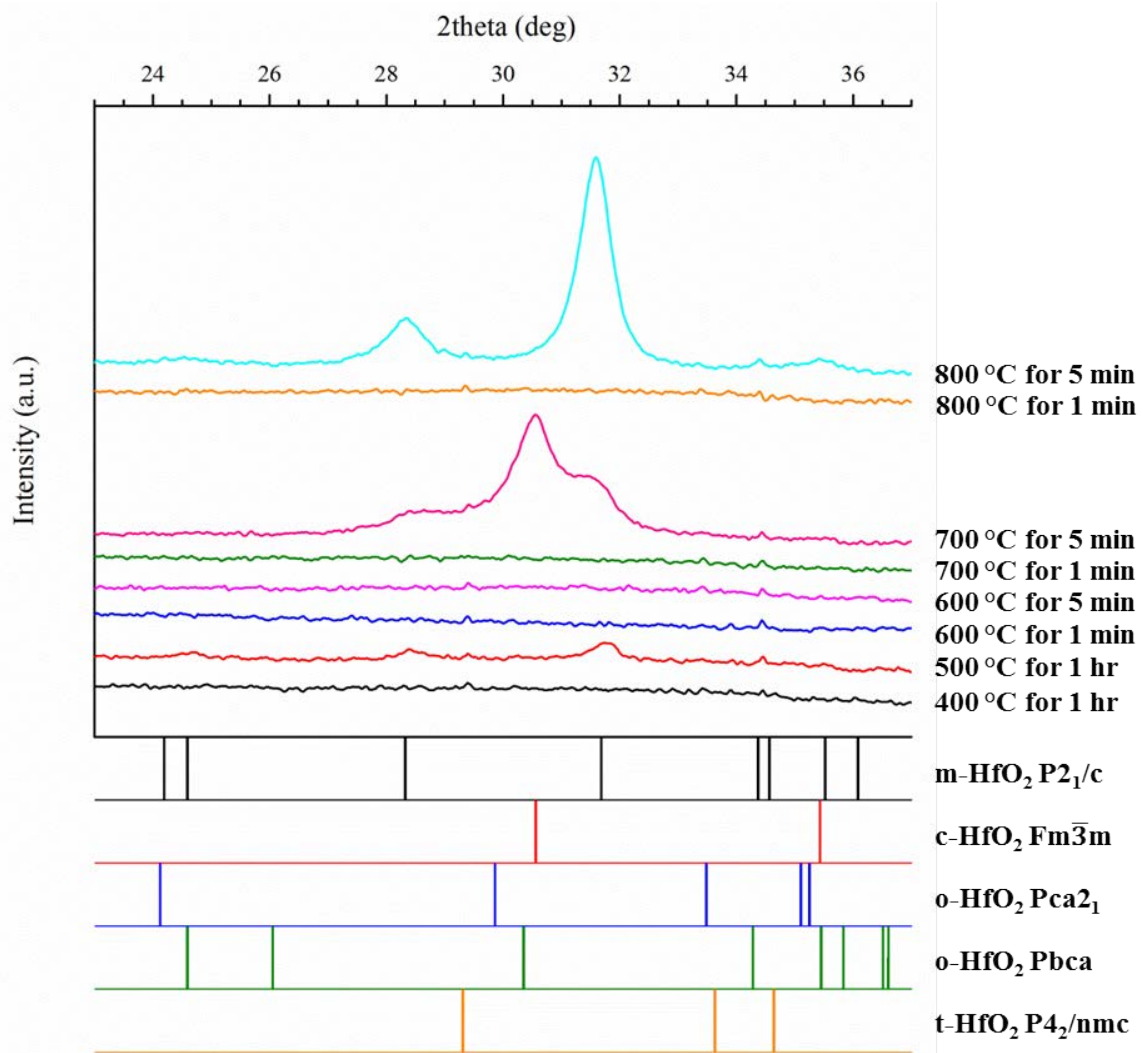


Figure 4.1 This is a plot of the diffraction spectra of a hafnia thin film on c-cut sapphire. The annealing time and temperature is shown beside each curve. The standard peak positions for each space group of hafnia are also shown below the diffraction spectra with the space group marked.

As is quickly evident from the diffraction data, all samples annealed for only 1 minute, the sample annealed at 400 °C, and the sample annealed at 600 °C for 5 minutes have no peaks show up in the XRD plot from the hafnia thin film. These films are amorphous. When the films are annealed to 500 °C for an hour, the faintest of peaks corresponding to the monoclinic -111 and 111 peaks are visible indicating that the crystallization process is beginning. Upon annealing at higher temperatures, diffraction peaks appear in the spectrum. For the sample annealed at 700 °C for 5 minutes in air, the same monoclinic peaks visible in the 500 °C sample appear but an additional peak at 30.6 ° also appears. This diffraction peak is from a high symmetry phase of hafnia believed to be the cubic phase. When the sample is annealed to higher temperatures, only the monoclinic peaks appear in the diffraction data. The appearance of the high symmetry phase diffraction peak in the diffraction data of the hafnia film annealed at 700 °C is a promising first result for synthesizing this phase of hafnia with no dopants. The desire was to maintain this high symmetry phase with one coat and to optimize the synthesis procedure. An additional test showed that for one coat, 700 °C for 3 minutes yielded a thin film with no visible monoclinic peaks. Therefore, an annealing time of 3 minutes was used for the rest of the experiment.

To further pare down on the appropriate annealing temperature, annealing temperatures of 650 °C, 675 °C, 700 °C, 725 °C, and 750 °C were used with an annealing time of 3 minutes in air. The same 1.8 M hafnium oxychloride solution was used and the solution was statically dropped onto the substrate. The samples were spun at 6000 rpm for 30 s with an acceleration of 1064 rpm/s on a c-cut sapphire substrate. These samples were only coated once. To

qualify the thin films, GIXRD was used. The omega was fixed to 1.5° for all of the scans. The diffraction spectrum for the films is shown below as Figure 4.2. The standard peak positions for several phases of hafnia are shown below the spectrum with the corresponding space group denoted beside each standard. Only the samples annealed at 725°C and 750°C showed a peak beginning to form around 30.6° which corresponds to one of the high symmetry phases of hafnia. The lower temperature anneals appeared mostly amorphous with a slight hump around the monoclinic 111 peak. For the samples annealed at 750°C , based on the heat treatment, the substrates would crack apart which made them unsuitable for further use.

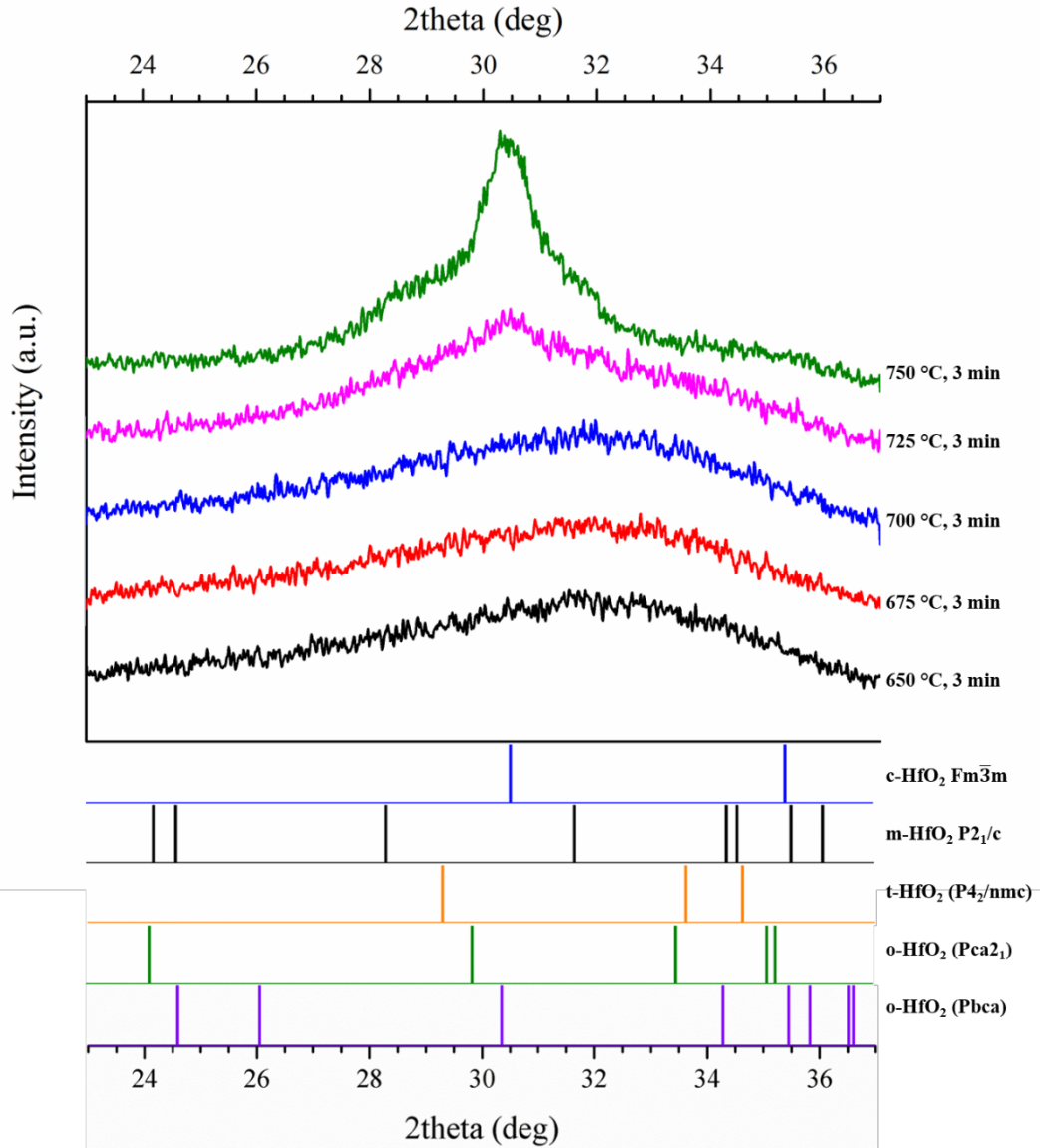


Figure 4.2 This is a plot of the diffraction spectra of a hafnia thin film on c-cut sapphire. The annealing time and temperature is shown beside each curve. The standard peak positions for each space group of hafnia are also shown below the diffraction spectra with the space group marked.

4.2 Starting Temperature Study

In section 4.1, the annealing temperature was optimized to produce the high symmetry phase of hafnia in thin film form with no dopants. This study showed that the appropriate annealing

temperature was 725 °C for 3 minutes. The process for making the hafnia thin films involved a rapid thermal process whereby the spun samples were placed into a preheated alumina boat in a preheated tube furnace at a given temperature. It was important to understand how the initial temperature played a role in the phase formation of the hafnia thin film. The temperature necessary to transform the monoclinic phase of hafnia to tetragonal and cubic are about 2000 K and 2900 K [1], respectively. The temperatures achieved in the tube furnace do not reach near that temperature. This being the case, the rate at which the film is heated (stress) is most likely the cause for the formation of this high symmetry phase. The rapid annealing process was accomplished by preheating an alumina boat to the annealing temperature, allowing the boat to cool for a set amount of time to achieve the desired starting temperature, and then placing the sample into the boat. This would cause the sample to heat from room temperature to several hundred degrees Centigrade in a matter of seconds. It was not possible to measure the temperature profile of the sample itself. The way to best estimate the sample temperature, which was important for understanding the rapid anneal's effects on the phase of the film, was to use a thermocouple attached to the bottom of the alumina boat. In this way, the temperature of the boat (which was a much larger thermal mass than the sample) could be used to estimate the temperature of the sample. The plot below, Figure 4.3, shows the temperature profiles for the alumina boat during the anneal which gives a good estimation of the temperature experienced by the sample.

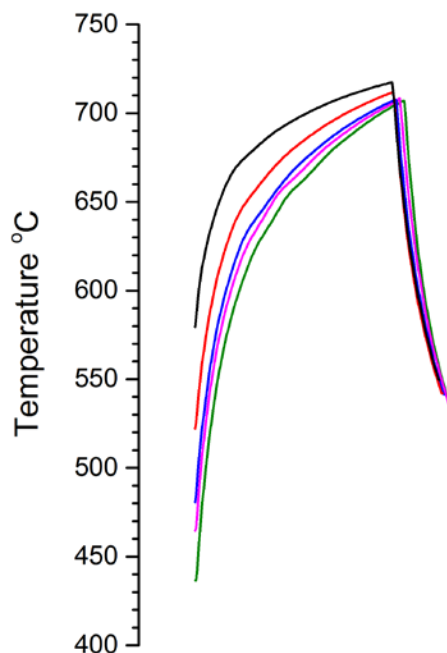


Figure 4.3 This is a plot of the temperature profiles used in this study. Each plot extends over 3 minutes of time. The alumina boat was cooled to vary the starting temperature and each time, the boat was placed back into the center of a preheated tube furnace at 725 °C.

The procedure for synthesizing the hafnia thin films was similar to the previous section. The c-cut sapphire was cleaned using compressed air, methanol, acetone, and methanol. It was placed onto the spin coater and the 1.8 M solution was statically dropped onto the sample. The sample was spun at 6000 rpm for 30 s with an acceleration of 1064 rpm/s. A tube furnace was preheated to 725 °C with an alumina boat in the center. Once the alumina boat had been at 725 °C for at least 5 minutes, the alumina boat was pushed to the edge of the tube and allowed to cool to the appropriate temperature as shown in the temperature profile above. The spun sample was then placed into the alumina boat and the boat was pushed into the center of the tube furnace. A thermocouple was measuring the temperature of the alumina boat constantly. After 3 minutes, the sample was removed.

A GIXRD plot of the hafnia films is shown below as Figure 4.4 with the peak position standards for each phase of hafnia shown below the plot. Marked with each diffraction set is the starting temperature of the sample as measured by the thermocouple on the alumina boat. For the sample that was annealed from 560 °C up to 725 °C, monoclinic peaks were the only diffraction peaks that showed up. These data corroborate what was seen in Figure 4.1. When the temperature is too high, the monoclinic phase will form in the hafnia. For all other samples, the high symmetry phase diffraction peaks appeared. The sample annealed from 520 °C to 725 °C showed some significant monoclinic peaks. The samples annealed from lower temperatures to 725 °C showed mostly high symmetry phase hafnia diffraction peaks with the monoclinic diffraction peaks showing up as shoulders. Therefore, 480 °C was chosen as the starting temperature to anneal the films to 725 °C to keep to a minimum the amount of monoclinic phase in the hafnia film and to maximize the amount of the high symmetry phase.

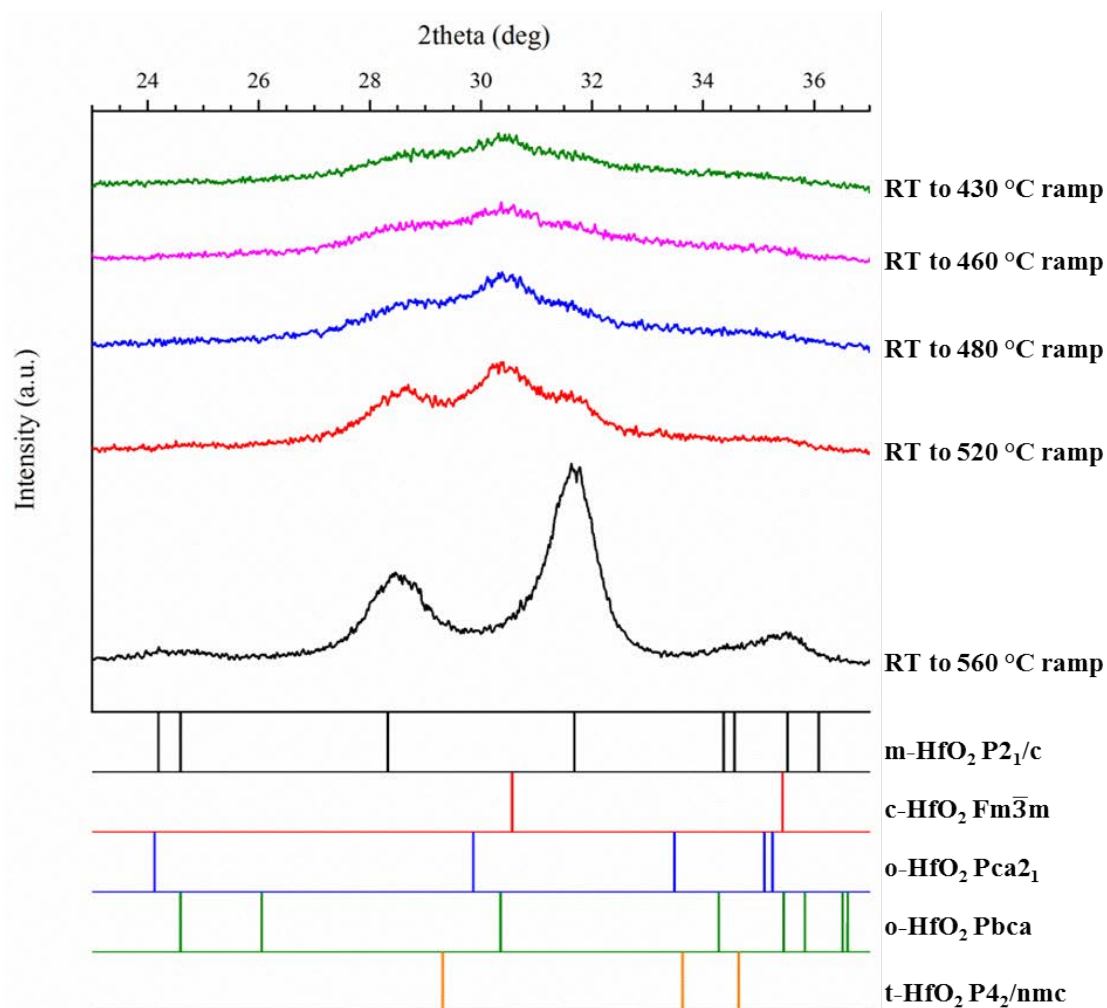


Figure 4.4 This is a plot of the GIXRD diffraction data of the hafnia film produced by varying the starting temperature of each sample. The diffraction data from each film has the starting temperature of that sample marked beside it. Below the diffraction plot is the standard peak positions of each phase of hafnia with the space group marked beside each one.

4.3 Solution Concentration Study

At this point, it was important to ensure that the solution concentration was appropriate for obtaining the high symmetry phases of hafnia in the thin film form. The solution concentration used in section 4.1 and 4.2 was 1.8 M hafnium oxychloride with 1.8 M glycine. In this portion of the study, the concentration of the solutions was varied by synthesizing new

batches of hafnium oxychloride solution. This was done by mixing an equivalent number of moles of hafnium oxychloride and glycine into deionized water, stirring and heating as mentioned previously, and filtering the new solutions through the 0.2 μm PTFE filter. The glycine and the hafnium oxychloride reacted to form a metal-ligand complex which would increase the viscosity of the resulting solution. The solution concentrations were 0.4 M, 1.1 M, 2.0 M, 2.2 M, and 2.5 M. Because the 1.8 M concentration began showing the desired phase of hafnia, the concentration was varied in finer steps near this 1.8 M concentration. Each sample was coated once with the appropriate hafnium oxychloride solution. The solution was statically dropped onto a c-cut sapphire substrate and spun at 6000 rpm for 30 s with an acceleration of 1064 rpm/s. Because the diffraction data showed that annealing the samples at 725 $^{\circ}\text{C}$ produced the high symmetry phase of hafnia without the samples breaking apart, all samples were annealed at 725 $^{\circ}\text{C}$ for 3 minutes with a starting temperature of 480 $^{\circ}\text{C}$. The GIXRD spectrum for this study is shown below as Figure 4.5 with the standard peak positions corresponding to the phases of hafnia shown below the spectra.

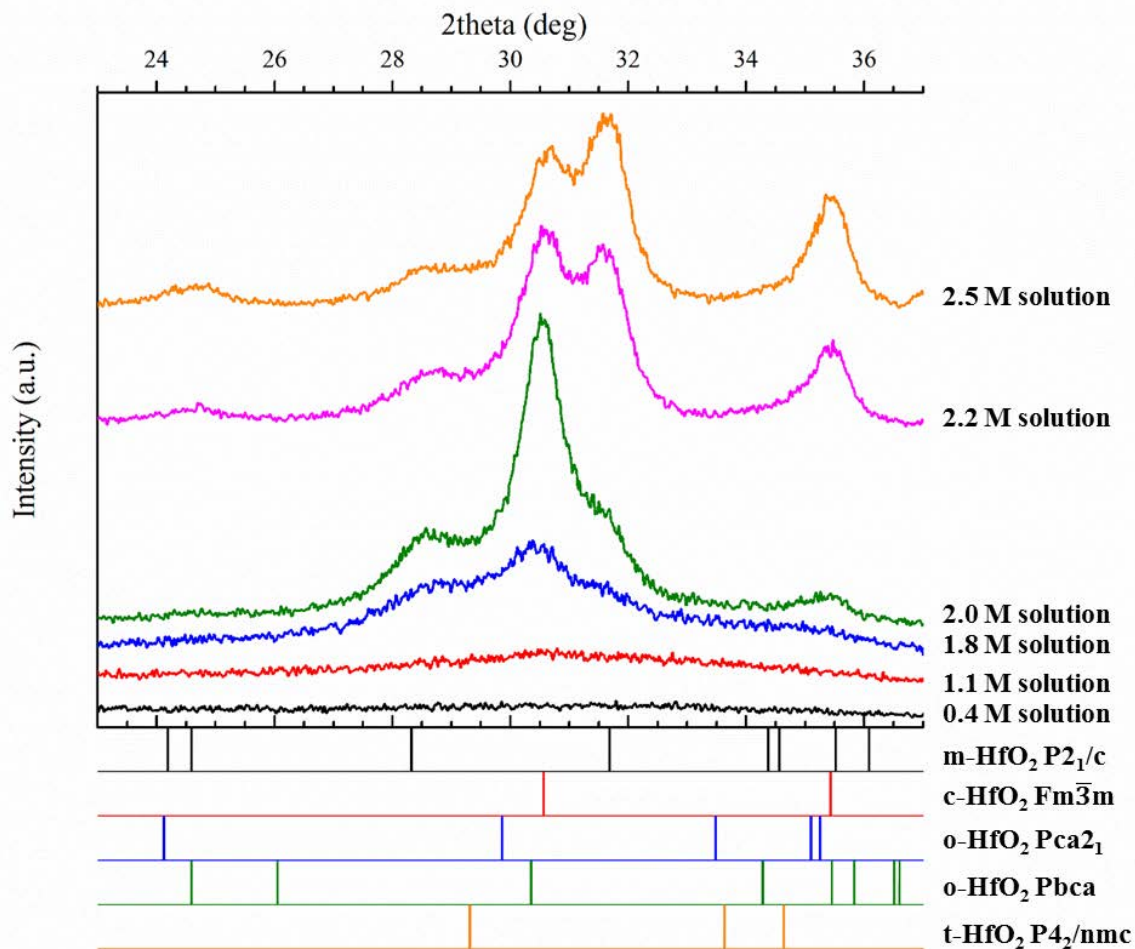


Fig 4.5 This is a plot of the GIXRD spectra from the hafnia thin films. The concentration for the precursor solution used to produce each hafnia thin film is shown beside each curve. The standard peak positions for each space group of hafnia is shown below the diffraction plots with the space group marked.

To further understand the diffraction data, XRR was done to each film to measure its thickness. These data show that the thickness for the films made from the 0.4 M, 1.1 M, 1.8 M, 2.0 M, 2.2 M, and 2.5 M precursor solutions were 10.9 nm, 35.7 nm, 58.9 nm, 57.9 nm, 60.1 nm, and 59.7 nm, respectively. The films made from the 0.4 M and 1.1 M solutions showed no diffraction peaks in GIXRD. This could be due to the necessity for higher

annealing temperatures or longer annealing times to achieve crystallinity due to their smaller thickness. As an example, the crystallization temperature of an amorphous thin film was shown to increase as the thickness of the film decreased [80]. The diffraction data of the films made from the higher concentration solution all showed a high symmetry phase of hafnia which is believed to be the cubic phase. The diffraction data showed that the films produced from the 2.2 M and 2.5 M concentration precursor solutions had an increasing amount of the monoclinic phase. This is evidenced by the increasing intensity of the monoclinic peaks as compared to the intensity of the high symmetry phase diffraction peak. Because the thicknesses of the films made from the precursor solutions of 1.8 M, 2.0 M, 2.2 M, and 2.5 M concentrations were roughly equivalent, the difference in phase formation is most likely due to some interaction between the metal and ligand complex. One simple way to determine the amount of each phase is to look at the ratios of the peak intensities of these peaks. This method works in this scenario because the mass absorption coefficients for all of the phases of hafnia are roughly equivalent. This means that the peak intensity ratio should give a reasonable estimation of the amount of each phase. In table 4.1, the ratios of the peak intensity of the high symmetry phase (here labeled c-HfO₂) was compared to the peak intensity of the -111 m-HfO₂ and the 111 m-HfO₂ peaks.

Table 4.1 This table shows the peak heights for the major diffraction peaks in Figure 3.3. The ratios of the peak heights are also shown which gives an indication of the phase fraction of each phase.

Concentration	-111 m-HfO ₂ peak height	111 m-HfO ₂ peak height	c-HfO ₂ peak height	ratio of c-HfO ₂ :-111 m-HfO ₂	ratio of c-HfO ₂ :111 m-HfO ₂
1.8 M	139	152	209	1.50	1.38
2.0 M	179	228	557	3.11	2.44
2.2 M	106	328	369	3.48	1.13
2.5 M	94	362	305	3.25	0.84

The previous studies have shown that a high symmetry phase of hafnia can be grown onto c-cut sapphire substrates with chemical solution deposition and no dopants. The heating rate appears to play an extremely important role in phase formation as well as the concentration of the precursor solution. For this chemistry on sapphire, the 2 M concentration precursor solution annealed to 725 °C for 3 minutes at a starting temperature of 480 °C yields hafnia thin films with a very high phase fraction of the high symmetry phase of hafnia.

CHAPTER 5

PROCESSING STUDY AND ELECTRICAL PROPERTIES OF HIGH SYMMETRY PHASE HAFNIA THIN FILMS GROWN ON SILICON

In chapter 4, hafnia thin films of high symmetry phase were grown on c-cut sapphire substrates via chemical solution deposition with no dopants. However, as was mentioned in the opening paragraph of that chapter, the importance of the high symmetry phase comes from hafnia's use as a high-k dielectric in MOSFETs and from its use as a ferroelectric material. In order to realize these goals, it is important to interface the hafnia thin films with silicon instead of sapphire. This is due to two reasons: 1) the architecture of almost all ICs are built on silicon and 2) metal coated silicon is readily available and well-understood.

As the heating rate played a large role in the phase formation of the hafnia thin film and because silicon and sapphire have different thermal conductivities, lattice constants, and coefficients of thermal expansion, some processing parameter optimization is important to begin the study of hafnia thin films on silicon substrates before characterizing their microstructure and electrical properties.

In this chapter, verification of the appropriate heating rates for the hafnia thin films on silicon will be studied. Additionally, the importance of lattice parameters will be looked at by addition of an intermediary layer between the silicon substrate and the hafnia thin film. To qualify the thin films, GIXRD will be used to know the film's phase while AFM and XRR will be used to find the films quality through roughness and thickness. Finally, the electrical

properties of the hafnia films will be measured. The dielectric constant and leakage currents will be shown with comparisons to values found in literature. The polarization curve as well as the dissipation factors will also be shown for the films to show the quality of the hafnia thin films.

5.1 Substrate Thickness Study

Because the starting temperature had such a profound effect on the phase of the thin film, it was important to study how the thickness of the silicon substrate would affect the synthesis of the high symmetry phase. This is directly related to the heating rate because the thicker the substrate, the more material must be heated before the energy can conduct to anneal the hafnia thin film. For this study, 280 μm , 370 μm , 450 μm , 530 μm , 630 μm , and 670 μm thick silicon substrates were used. Each was boron doped, single side polished silicon with a resistivity between 1 and 100 Ωcm . Each substrate was heated to 250 $^{\circ}\text{C}$ for 30 seconds so that the solution would wet the surface. For this portion of the study, 2.0 M hafnium oxychloride solution was used. The substrates were placed onto the spin coater, the solution was statically dropped onto the substrate, the sample was spun at 6000 rpm for 30 s with an acceleration of 1064 rpm/s, the samples were heated from 480 $^{\circ}\text{C}$ to 725 $^{\circ}\text{C}$ for 3 minutes. The GIXRD plots for each sample are shown below as Figure 5.1 with the peak position standard for each phase of hafnia shown below the plot. Each diffraction spectrum is marked with the thickness of the silicon substrate on the plot.

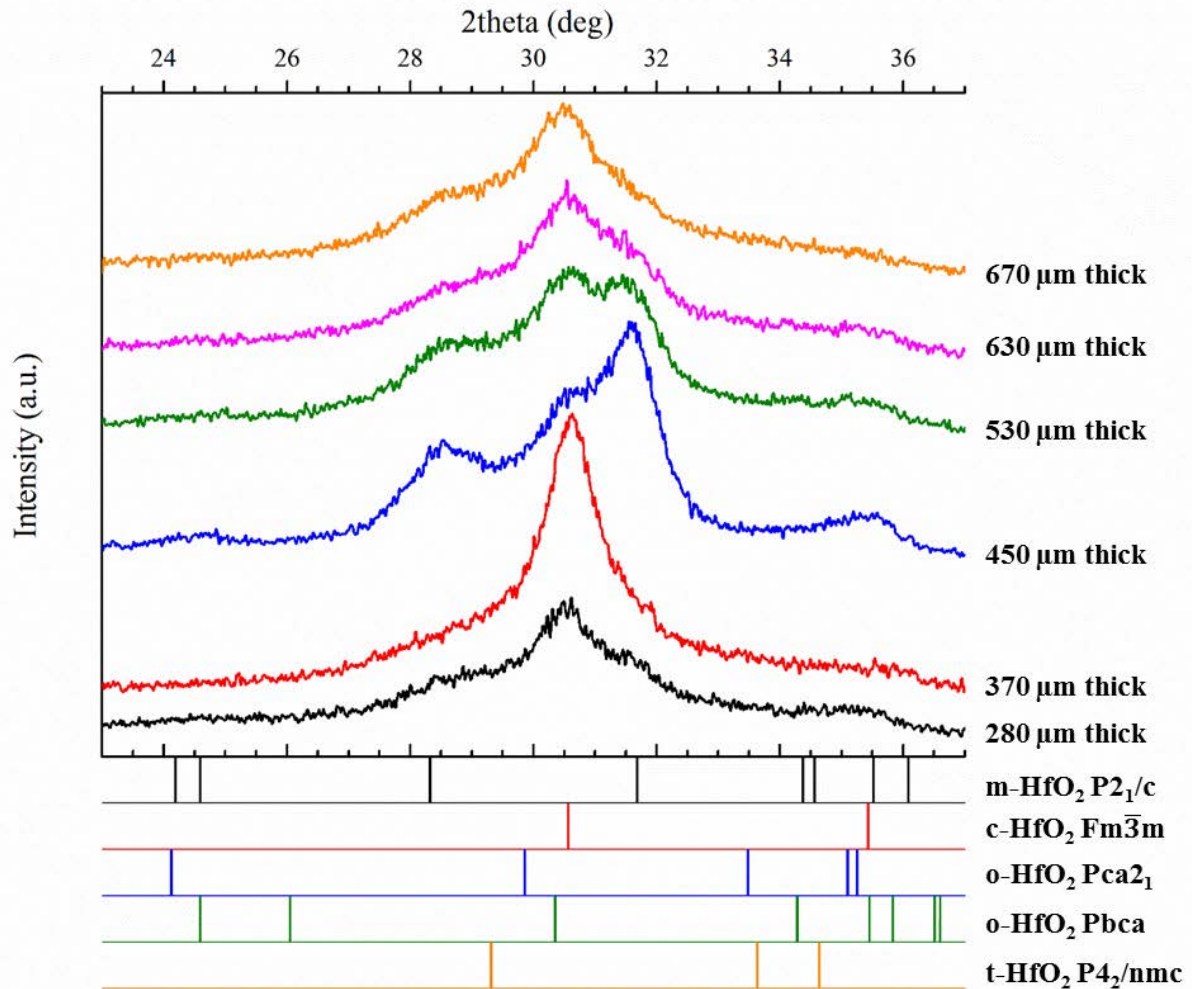


Figure 5.1 This is a plot of the diffraction spectra of a hafnia thin film on varying thicknesses of silicon. The thickness of the silicon substrate used is shown beside each diffraction spectrum. The standard peak positions for each space group of hafnia are also shown below the diffraction spectra with the space group marked.

Two pieces of information can be gleaned from this plot: substrate thickness affects phase formation and the hafnia thin film phase formed on silicon is different than that of the same thickness sapphire. One explanation that can explain both of these is thermal conductivity of the substrates. As seen in section 4.2, the heating rate plays a large role in the phase formation of the hafnia thin film. The thermal conductivity of silicon in the range of the

anneal goes between ~ 1.5 W/cm K to ~ 0.3 W/cm K [81] while the thermal conductivity of sapphire in the range of the anneal goes between ~ 0.4 W/cm K to ~ 0.1 W/cm K [82]. As seen in both Figure 4.1 and 4.4, if the heating rate or total amount of heat is too high, the phase formed is the monoclinic phase. As the thermal conductivity is higher in silicon for all temperatures, the thickness of the silicon substrate can be higher and still achieve the same kind of heating rate as seen in the $430\text{ }\mu\text{m}$ thick sapphire substrate. This is why the hafnia films grown on the thicker substrates ($630\text{ }\mu\text{m}$ and $670\text{ }\mu\text{m}$ thick) show the high symmetry phase similar to the sapphire substrates in chapter 4.

As the thickness of the silicon substrate decreases, the phase fraction of the monoclinic phase increases as evidenced by the increase in intensity of the monoclinic diffraction peaks.

However, an abrupt change occurs once the silicon substrate reaches the thickness of $370\text{ }\mu\text{m}$. At this thickness at with the thinner substrate ($280\text{ }\mu\text{m}$), the monoclinic diffraction peaks no longer show up in the diffraction spectrum. To confirm all of these results, 5 more hafnia thin films were grown on each thickness substrate and GIXRD was done to confirm the phase. With no exceptions, the diffraction data looked identical. The next possibility was due to the dopant concentration for each substrate. The hypothesis was that if the dopant concentration was significantly different, the thermal conductivity of the substrates could change drastically. However, a study done by M. Asheghi, et al. [83] showed that the thermal conductivity of silicon was independent of doping level above about 100 K. This discrepancy is phase is not understood and would require further study to elucidate the reasoning behind the appearance of the high symmetry phase in the thinnest of silicon samples.

Although thermal conductivity seems to be the most likely reason behind the difference in the hafnia film phase seen on the sapphire substrate and the silicon substrate of similar thickness, there exist two other possibilities that could be the reason behind this difference. The first could be the difference in lattice mismatch between the silicon-hafnia interface and the sapphire-hafnia interface. The lattice constant for the silicon is 5.43 Å [84]. The lattice constant for sapphire (a-direction) is 4.79 Å [85]. Hafnia has several polymorphs with varying lattice parameters. Because this film is most likely cubic, orthorhombic, or tetragonal, these are the lattice parameters which will be covered. Based on the work by J. Jaffe et al. [86], the lattice constant for cubic hafnia is 5.06 Å, for tetragonal hafnia is $a = 3.58$ Å, $c = 5.20$ Å, and for orthorhombic-I hafnia is $a = 9.83$ Å, $b = 5.17$ Å, and $c = 4.96$ Å. Due to the number of lattice parameters, the lattice mismatches are shown in table 5.1.

Table 5.1 This is a table showing the lattice mismatch between the different directions of the high symmetry phases of hafnia and both silicon and sapphire substrates.

	Si substrate	Al ₂ O ₃ substrate
cubic HfO ₂	6.8 %	-5.6 %
tetragonal HfO ₂ a-direction	34.0 %	25.3 %
tetragonal HfO ₂ c-direction	4.2 %	-8.6 %
orthorhombic HfO ₂ a-direction	-81.0 %	-105.2 %
orthorhombic HfO ₂ b-direction	4.8 %	-7.9 %
orthorhombic HfO ₂ c-direction	8.7 %	-3.4 %

As is seen from the table, most of the high symmetry phases would be in compression if epitaxially grown on sapphire where the phases would be in tension if epitaxially grown on

silicon. The difference between the two remains a possible reason for the variation in phase seen between the film grown on the sapphire and that on the substrate. The difference in coefficient of thermal expansion likely doesn't play a role in this scenario. The thermal expansion coefficient at room temperature for silicon is $3.0 \times 10^{-6} \text{ K}^{-1}$, for sapphire is $7.0 \times 10^{-6} \text{ K}^{-1}$ [87], and for hafnia is $4.6 \times 10^{-6} \text{ K}^{-1}$ [88]. If the amount of lattice mismatch relief is calculated based on these values, the amount of extra strain is negligible compared to the mismatch that is experienced at the interface of the films.

To test the effects of the lattice mismatch between the film and the substrate, an intermediary layer can be deposited between the two which will be covered in the next section. The high symmetry phase of hafnia can be grown on silicon substrates on multiple thicknesses. This allows for further testing of the films which will be covered in future sections.

5.2 Intermediary Layer Study

Based on section 5.1, it was seen that to grow the high symmetry phase of hafnia in thin film form on silicon, substrate thicknesses of 370 μm and 670 μm were most effective. To elucidate the extent to which lattice mismatch played a role in forming these phases, hafnia films were grown on 670 μm silicon substrates as received and with intermediary layers of platinum and titanium nitride. Additionally, the effects of a platinum intermediary layer on the phase formed on 370 μm thick silicon were also studied. The plain silicon substrates were purchased from University wafer. The platinized silicon wafers were purchased from MEMS Exchange. The silicon wafer with a TiN coating was given by NaMLabs out of Dresden,

Germany. They were unable to provide a 370 μm thick silicon wafer coated with TiN. As a result, these were the only substrates tested for this study. The GIXRD of the hafnia thin films on the 670 μm silicon is shown as Figure 5.2 and on the 370 μm silicon is shown as Figure 5.3. Further, the quality of the films was found by measuring their roughness with AFM. The height retraces for each film are shown on 670 μm thick silicon, 670 μm platinized silicon, 670 μm titanium nitride coated silicon, 370 μm silicon, and 370 μm platinized silicon as Figure 5.4. The roughness of each was 1.245 nm, 0.582 nm, 1.366 nm, 0.691 nm, and 1.000 nm, respectively.

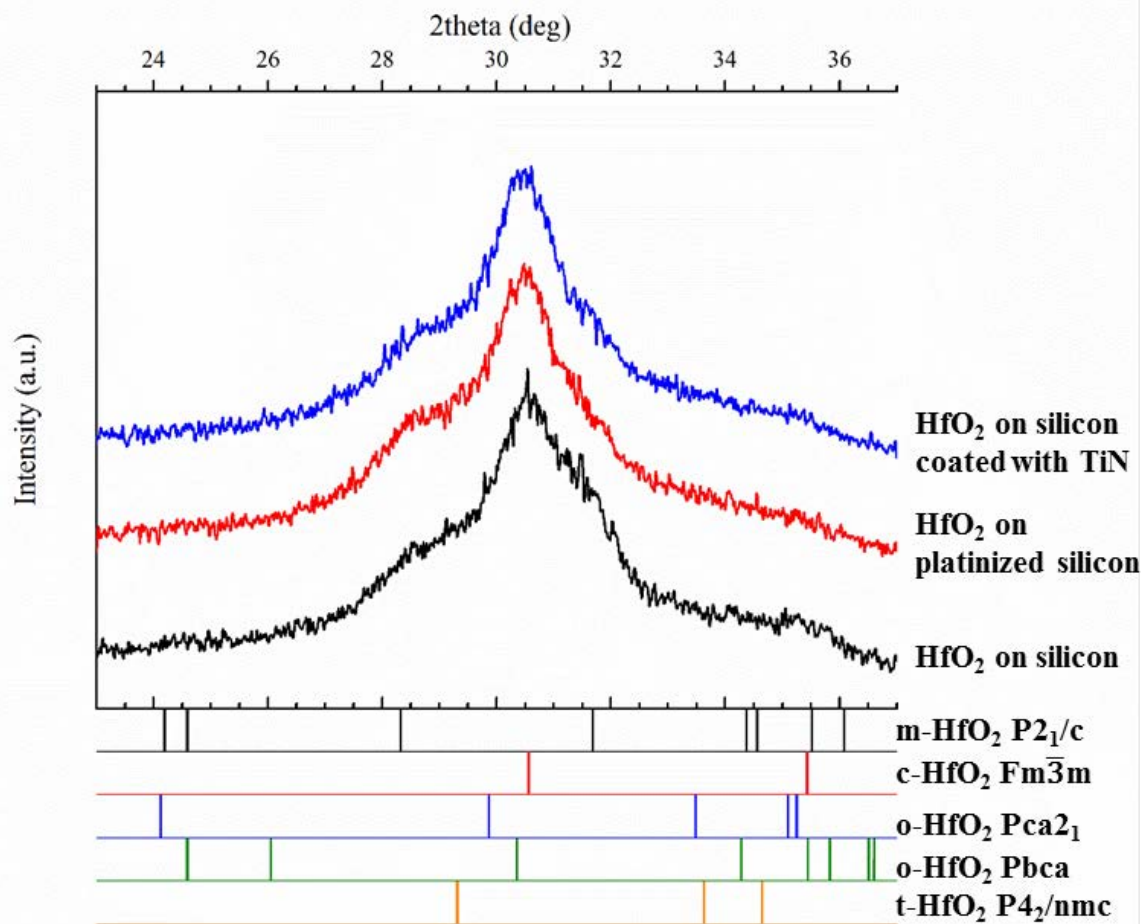


Figure 5.2 This is a plot of the diffraction spectra from hafnia films grown on 670 μm thick silicon substrates with different intermediary layers. The intermediary layers are marked next to each spectrum. The standard peak positions for each phase of hafnia is shown below the plot with the space group marked.

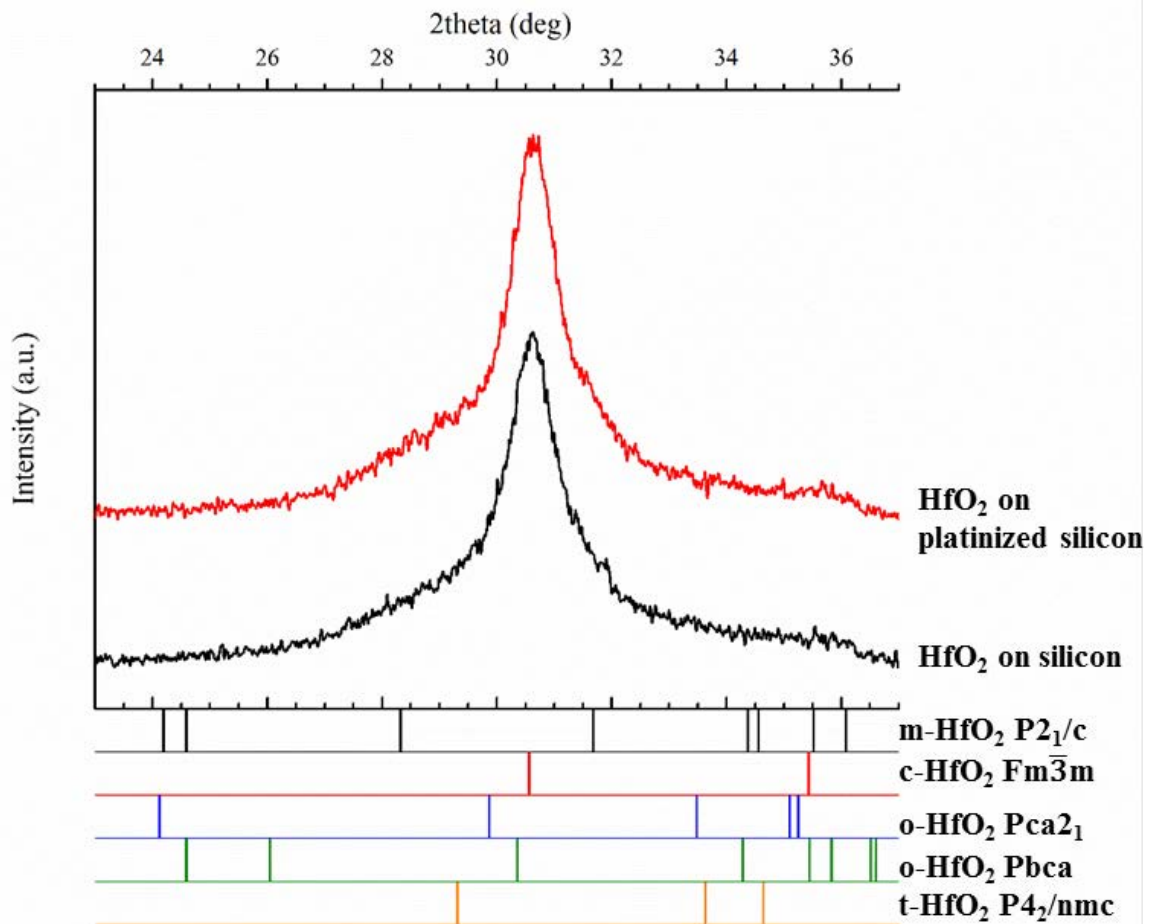


Figure 5.3 This is a plot of the diffraction spectra from hafnia films grown on 370 μm thick silicon substrates with different intermediary layers. The intermediary layers are marked next to each spectrum. The standard peak positions for each phase of hafnia is shown below the plot with the space group marked.

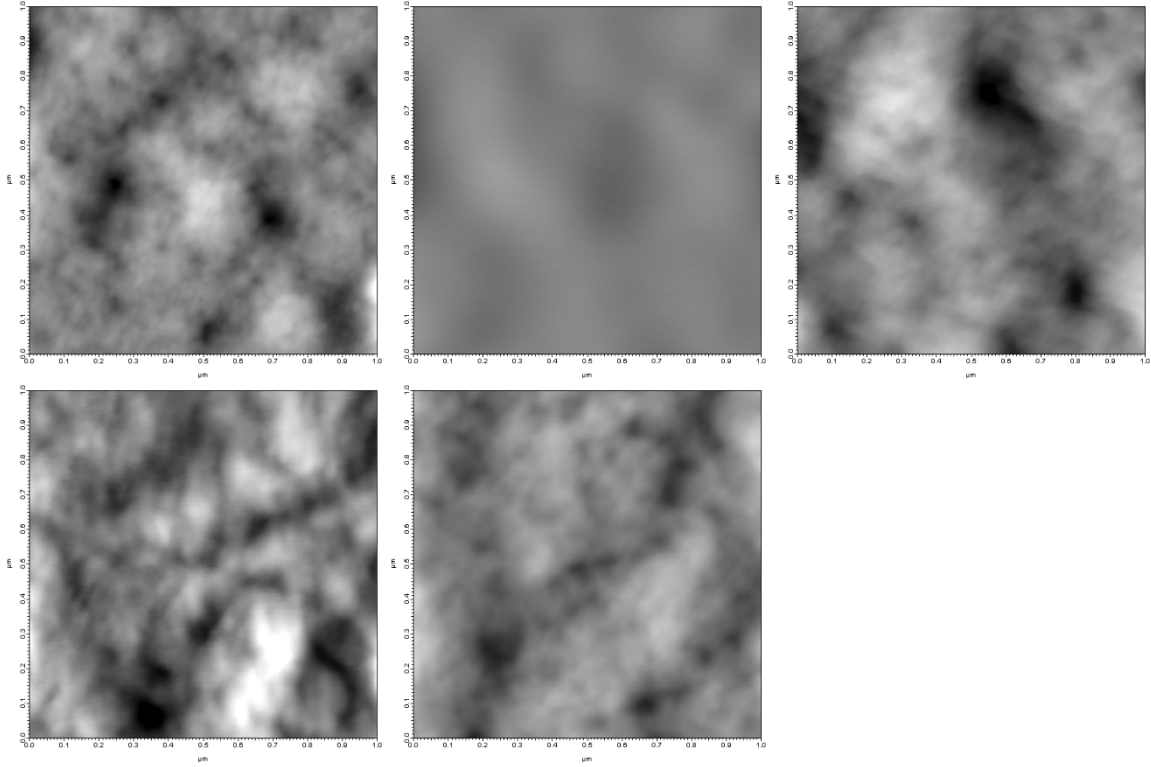


Figure 5.4 These are AFM height retraces of the hafnia layer on top of a) 670 μm silicon, b) 670 μm thick platinized silicon, c) 670 μm thick titanium nitride coated silicon, d) 370 μm thick silicon, and e) 370 μm thick platinized silicon.

These plots show that the bottom electrode does not affect the phase formation of the hafnia thin film. The platinum lattice parameter is 3.92 Å [89] and the titanium nitride lattice parameter is 4.24 Å [90] which correspond to a -29.1 % lattice mismatch and a -19.3 % lattice mismatch, respectively. The platinum layer on the platinized silicon for both 370 μm and 670 μm thick silicon was 100 nm thick and the titanium nitride layer was 12 nm thick. The thermal conductivity of platinum in the temperature range of this anneal was between 0.7 and 0.8 W/cm K [91]. The thermal conductivity of titanium nitride in the temperature range of the anneal is roughly constant at 0.2 W/cm K [92]. In comparison with the thickness of the silicon substrate, the thermal conductivity of the intermediary layers plays little role in

the phase formation of the hafnia film. From these data, it seems that the most important parameters are the thermal expansion coefficient and/or the thermal conductivity of the substrate which affects the heating rate of the hafnia film.

5.3 Electrical Properties of the High Symmetry Hafnia Films

To this point, x-ray diffraction has shown that the hafnia films grown on various substrates have a high symmetry phase. As mentioned in the introduction to chapter 4, this is of interest because of this phase's electrical properties. With the high symmetry phase now grown on silicon substrates with conductive intermediary layers, the electrical properties of these films became important to measure. Due to restricted access of a system that could deposit conductive TiN for use as a top electrode, the electrical properties of only the hafnia films grown on platinized silicon were measured. When platinum was used as a top electrode for the hafnia films grown on TiN coated silicon, the polarization curves looked like Figure 5.5 below regardless of voltage, frequency, or poling orientation across dozens of samples. This result is not understood and the mechanism behind it remains elusive. As a result, only the electrical properties of the hafnia films grown on 370 μm thick platinized silicon and 670 μm thick platinized silicon will be shown.

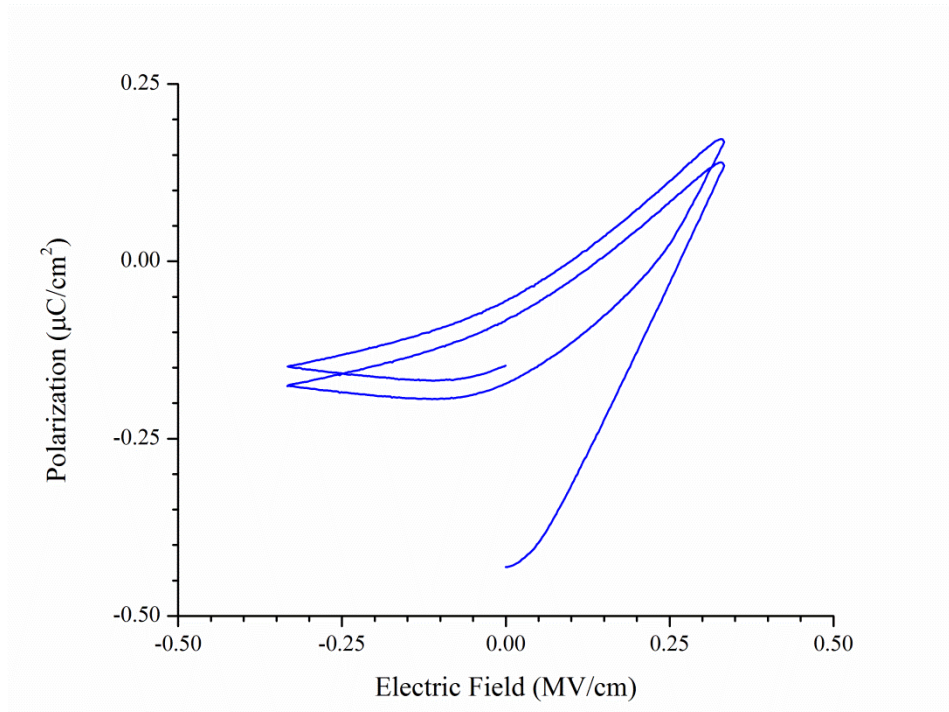


Figure 5.5 This is a plot of the polarization of a hafnia film grown on 670 μm thick silicon coated with TiN.

To measure the roughness and thickness of the hafnia film, AFM and XRR were used, respectively. The AFM height retraces are shown below as Figure 4.6a and 4.6b for the 670 μm and 370 μm thick silicon substrates. The scale bar for these height retraces is between -5 and 5 nm for the lowest and highest points, respectively. The roughness for the hafnia films grown on the 670 μm and 370 μm substrates over 1 μm^2 are 1.055 nm and 1.159 nm, respectively. The XRR data show that the film thickness for each hafnia film is about 75 nm. Those data are shown below as Figure 5.7. The AFM data show that the films are of fairly high quality with a roughness around 1 nm. The XRR data show the fringes dying off at low 2θ . This is probably due to the rough interface between the hafnia film and the platinum intermediary layer.

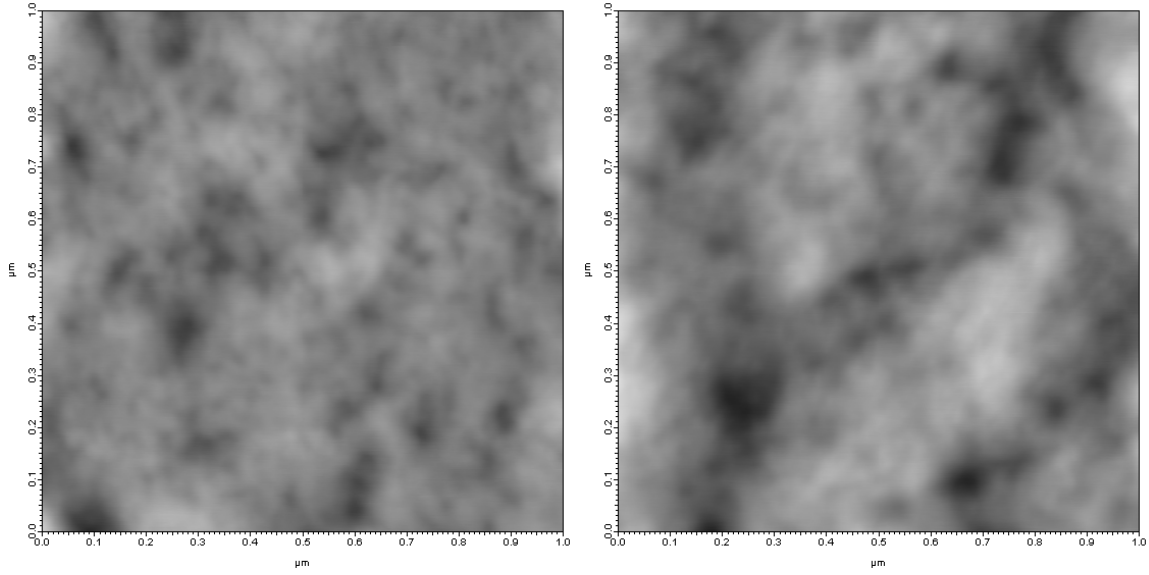


Figure 5.6 These are the height retraces from AFM of the hafnia film on a) 670 μm thick platinized silicon and b) 370 μm thick platinized silicon.

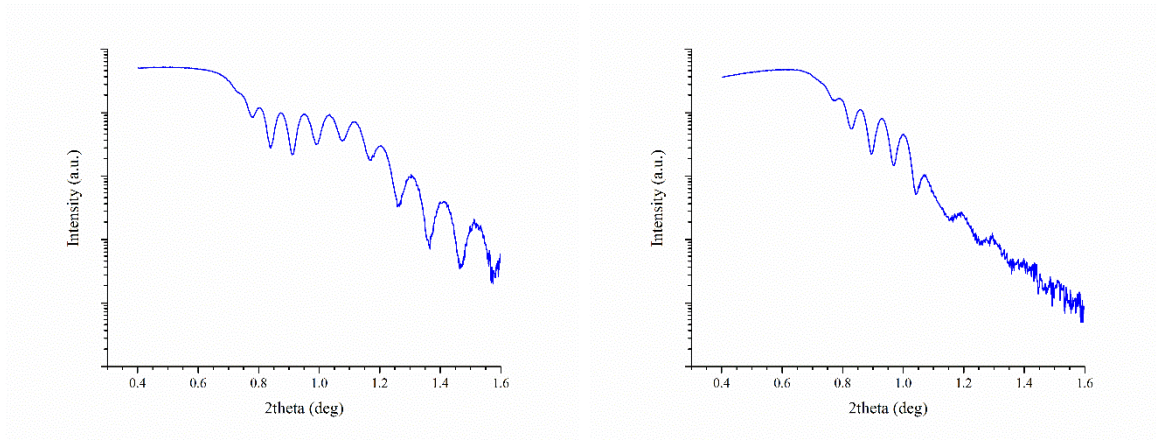


Figure 5.7 These are the XRR spectra for the hafnia film on a) 670 μm thick platinized silicon and b) 370 μm thick platinized silicon.

To measure electrical properties, platinum top electrodes had to be deposited onto the top of the hafnia films. This was achieved using shadow masks and a Kurt J. Lesker PVD 75 system. The platinum top electrodes were deposited to a thickness of 100 nm via e-beam deposition. The electrode areas were $10096.08 \mu\text{m}^2$ and $36543.93 \mu\text{m}^2$. The electrical properties were measured using a Keysight E4980A LCR meter and a Radiant Technologies

P-PMF system. The former system was used to measure the capacitance of the films at 1 V while varying the frequency and also measuring the dissipation factor. The latter was used to get polarization, transient current, and leakage current as a function of applied voltage. Plotted below is the capacitance and dissipation factor as a function of frequency for the hafnia film grown on the 670 μm substrate and the 370 μm substrate as Figure 5.8.

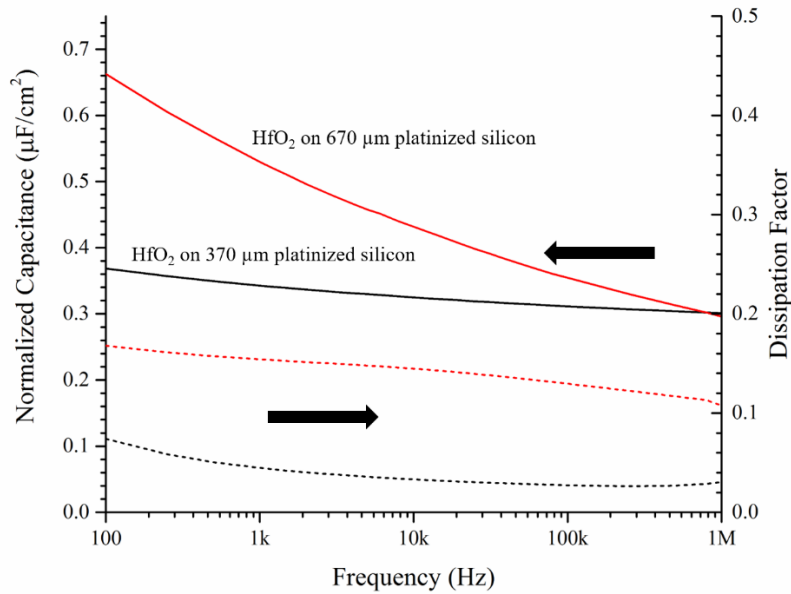


Figure 5.8 This is a plot of the normalized capacitance values and dissipation factor for the hafnia films grown on 670 μm thick platinized silicon and 370 μm thick platinized silicon. The solid lines correspond to the capacitance while the dashed lines correspond to the dissipation factor.

Taking the capacitance at 1 kHz, the dielectric constants of the films grown on 670 μm silicon and on 370 μm silicon were 47 and 30, respectively. However, the dissipation factor was so high for the film grown on the thicker substrate, that measuring the polarization curve and leakage weren't possible using the Radiant system. Therefore, the polarization, transient current, and leakage were only plotted for the film grown on 370 μm thick silicon. The plot

of the polarization and transient current are shown below as Figure 5.9 and the leakage current at 1.1 V and 1 MV/cm were $1.09 \mu\text{A}/\text{cm}^2$ and $620.84 \mu\text{A}/\text{cm}^2$, respectively. The leakage current was measured at 1.1 V because this is the goal voltage for silicon technologies. The results from the hafnia film grown on 370 μm thick platinized silicon are compared with values found in literature in table 5.2. This is because the leakage current and polarization of the hafnia film grown on the thicker platinized silicon substrate were unable to be measured. Additionally, the dissipation factor was so high at 1 kHz that comparing the dielectric constant would not be meaningful.

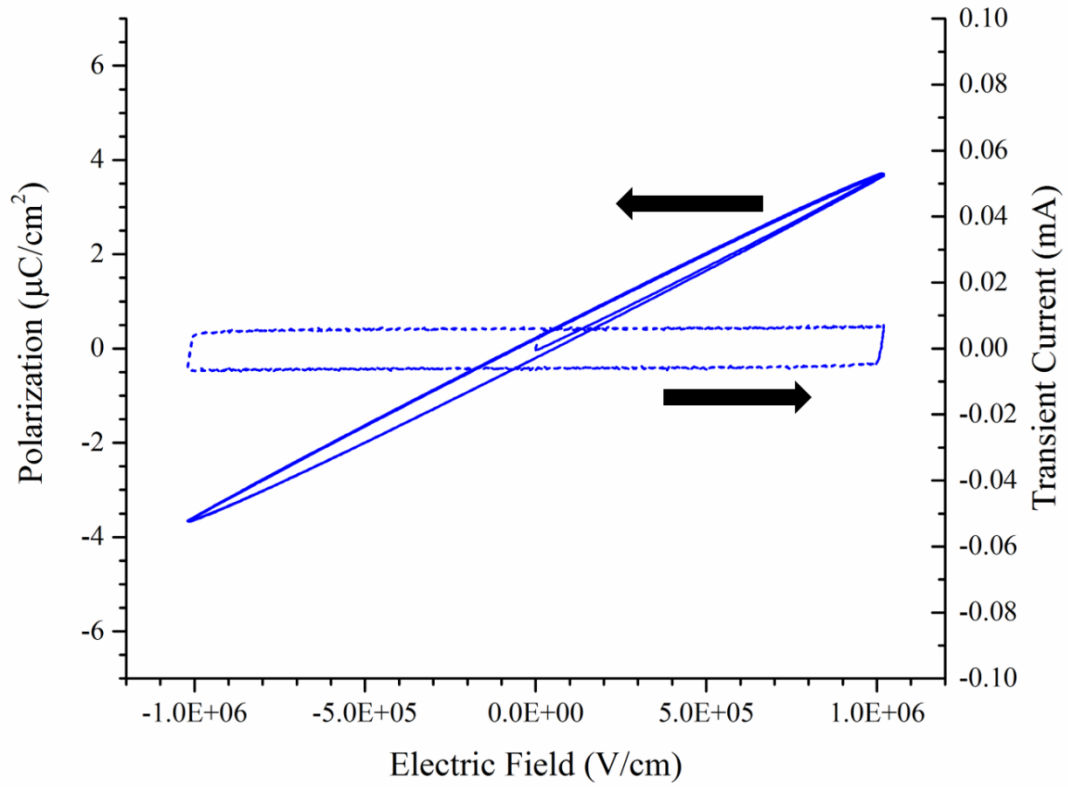


Figure 5.9 This is a plot of the polarization and the transient current for the hafnia film grown on 370 μm thick platinized silicon. The curves show good dielectric behavior with little losses. The small losses are indicated by near linear behavior in the polarization curve and the rectangular shape of the transient current plot.

Table 5.2 This is a table comparing some of the electrical properties of hafnia films in this work to the hafnia films found in literature.

	dielectric constant at 1 kHz	leakage current at 1 MV/cm
This work	30	$6.21 * 10^{-4} \text{ A/cm}^2$
Ref [93]	8.7 – 16.5	$3.9 - 5.8 * 10^{-8} \text{ A/cm}^2$
Ref [37]	23 – 42	$1.0 - 8.0 * 10^{-7} \text{ A/cm}^2$
Ref [94]	26	$>3.0 * 10^{-5} \text{ A/cm}^2$
Ref [95]	12.5 – 17.3	N/A

5.4 Multiple Coats Study

To date, thin films of pure hafnia that are of high symmetry phase (cubic, tetragonal, orthorhombic) have been grown almost exclusively via vacuum deposition techniques [96], [97]. Many other groups have utilized doping to achieve the higher symmetry phases of hafnia [1], [4], [98]. Additionally, S. Starschich has achieved higher symmetry phases of doped hafnia films using chemical solution deposition [5], [7], [46]. Recently, H. Liang et al. [37] were able to produce high symmetry phase hafnium oxide thin films via chemical solution deposition as pure hafnium oxide films and doped with yttria. They found that they were able to produce a nearly phase pure cubic/tetragonal phase hafnia film with and without dopants. It was found that with the yttria dopant, nearly phase pure cubic/tetragonal could be maintained even up to 23 nm film thicknesses. With the pure hafnia films, the high symmetry phases could be maintained up to about 16 nm thicknesses. In the case of pure hafnia, with higher thicknesses, the monoclinic phase began to appear in higher phase fractions. They were able to achieve all of this using a layer by layer approach. This involved spinning a layer of the oxide, annealing the film, and repeating the process until the desired thickness was achieved. By 40 nm thickness with pure hafnia, the cubic/tetragonal character was merely a shoulder on the 111 monoclinic hafnia peak.

The previous sections have shown that high symmetry phase of hafnia could be produced via spin coating with no dopants. However, outside of section 4.1, all of the prior work was done using one coat of hafnia which gave a film thickness of 75 nm. In this work, the high symmetry phase of hafnia is seen in film thicknesses significantly larger than that of [37].

However, due to the discrepancy between their seeing the high symmetry phase die off after the layer by layer processing to higher thicknesses, the aim of this study was to use layer by layer processing to achieve much thicker films with entirely high symmetry phase of hafnia. Based on the previous sections, a 2 M solution of hafnium oxychloride and glycine was synthesized to use as the precursor solution. This solution was filtered through a 0.2 μm PTFE filter to ensure all contaminants were removed from the solution. This solution was statically dropped onto a substrate and spun at 6000 rpm for 30 seconds with an acceleration of 1064 rpm/s. The samples were immediately annealed in air in a tube furnace to 725 °C for 3 minutes. The samples were then cooled quickly on a metal block at room temperature. To add more layers, the process was simply repeated for the desired number of layers. The substrates used were 100 nm platinized silicon substrates from MEMS Exchange with a 7 nm Ti adhesion layer on 370 μm thick silicon. All samples had 100 nm platinum top electrodes deposited onto them using a Kurt Lesker PVD 75 e-beam deposition system and shadow masks with electrode sizes of 10096.08 μm^2 and 36543.93 μm^2 .

The phase of the thin films was measured using a Rigaku SmartLab X-ray diffractometer in grazing incidence. For every measurement, omega was fixed at 1.5 °. For all XRR measurements, which was used to get film thickness and roughness, a PANalytical Empyrean X-ray Diffractometer was used and the data were analyzed using X'pert Reflectivity Software. To corroborate the roughness data from the XRR data, AFM was done on each sample using an Asylum Research Cypher Scanning Probe Microscope in tapping mode. For the electrical measurements, a Radiant Technologies P-MFP system was used to collect the

polarization loops and measure the leakage current in the samples while a Keysight E4980A LCR meter was used for the capacitance and dissipation factor measurements all done at 1 V with varying frequencies from 100 Hz to 1 MHz.

The roughness and texture of the starting platinized silicon substrates were measured. The roughness of the platinum was 1.067 nm RMS roughness (over $100\ \mu\text{m}^2$ area). The platinum was found to be textured (111) with a grain size of around 30 nm as measured by the Scherrer equation and confirmed with SEM. The hafnia films were deposited onto the platinized silicon substrates and annealed as discussed previously. The GIXRD plot showing the diffraction data of the hafnia films at different thicknesses is shown as Figure 5.10. The phase of the films appears to be cubic up to 300 nm thickness. At all thicknesses, the monoclinic peaks at 28.5° and 31.6° , corresponding to the (-111) and (111) monoclinic peaks appear as a shoulder on the pronounced (111) cubic peak for the hafnium oxide film. Doing a survey scan of the films, the only peaks that appear are from the cubic phase of hafnia and the platinum substrate with only slight peaks from the monoclinic phase. Using the Scherrer equation and following a Pseudo-Voigt model, the grain sizes were estimated for the films to be about 7.35 nm.

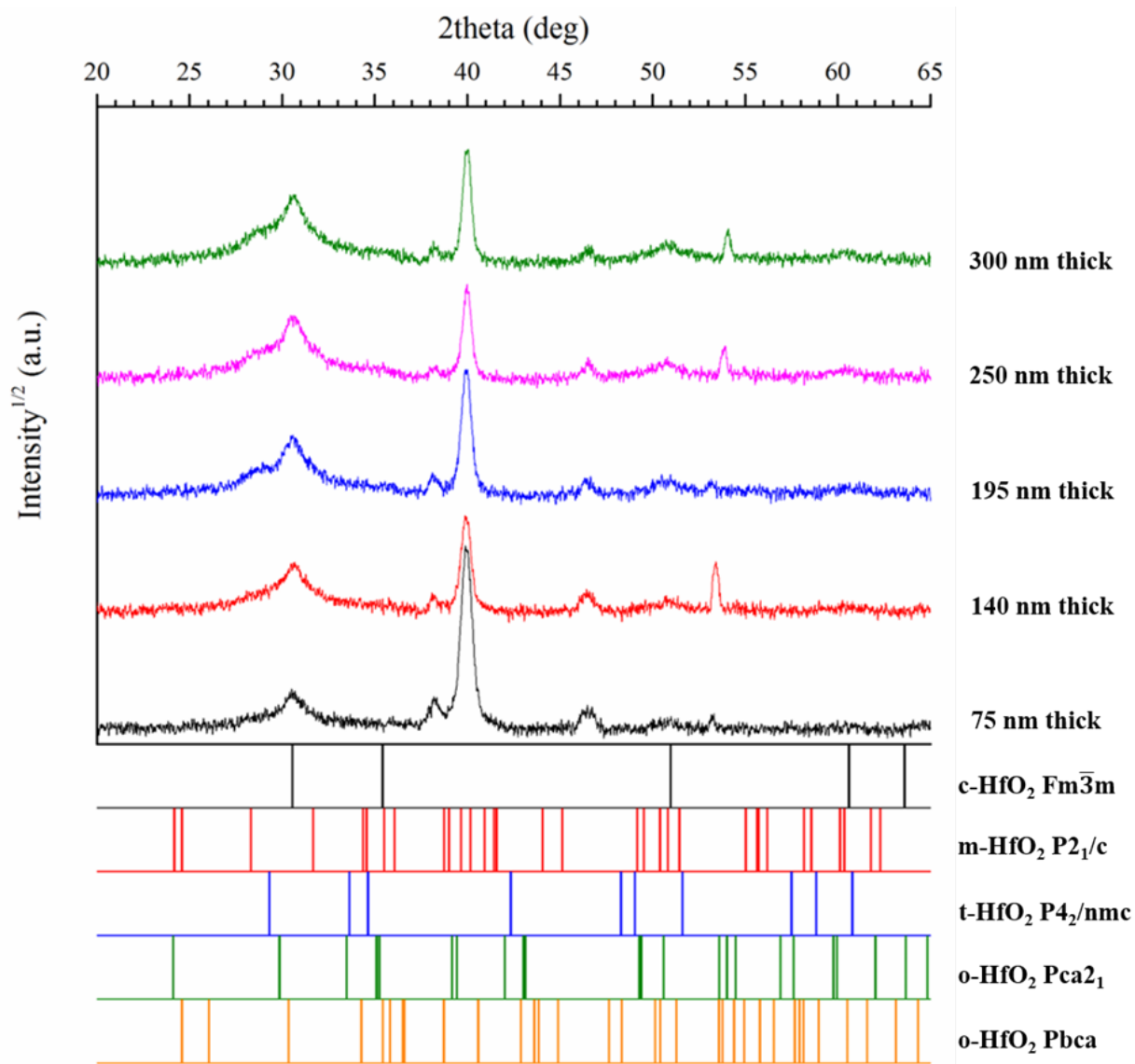


Figure 5.10 This is a plot of the GIXRD spectrum for the hafnia films at different thicknesses. The diffraction data for each film is marked with the thickness of the film. The standard peak positions are also shown below the spectra with the space groups listed.

This shows that the grain sizes of the films were extremely small and corroborate the cubic phase of hafnia. X-ray reflectivity spectra are shown for each of the films as Figure 5.11. The thickness of each film was 78.4 nm for 1 coat, 139.7 nm for 2 coats, 195.3 nm for 3 coats, 253.6 nm for 4 coats, and 298.7 nm for 5 coats. The thickness measured using XRR

was verified using SEM. To further analyze the microstructural quality of the films, AFM was done to measure the roughness of the films. The 3D representations of the height retraces of each of the films is shown as Figure 5.12 for $1\ \mu\text{m}^2$ areas and $900\ \mu\text{m}^2$ areas with the roughness values shown beneath each. From the GIXRD spectra, XRR spectra, and AFM images, these films appear to be of good quality with small grain sizes and nearly phase pure cubic crystal structure hafnia.

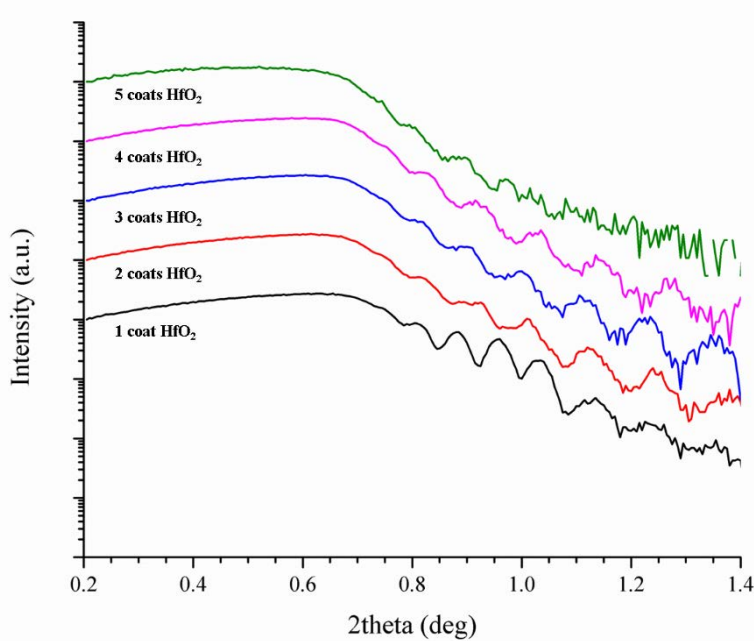


Figure 5.11 These are the XRR spectra for the hafnia layer on $370\ \mu\text{m}$ thick platinized silicon with the number of coats marked by each spectra.

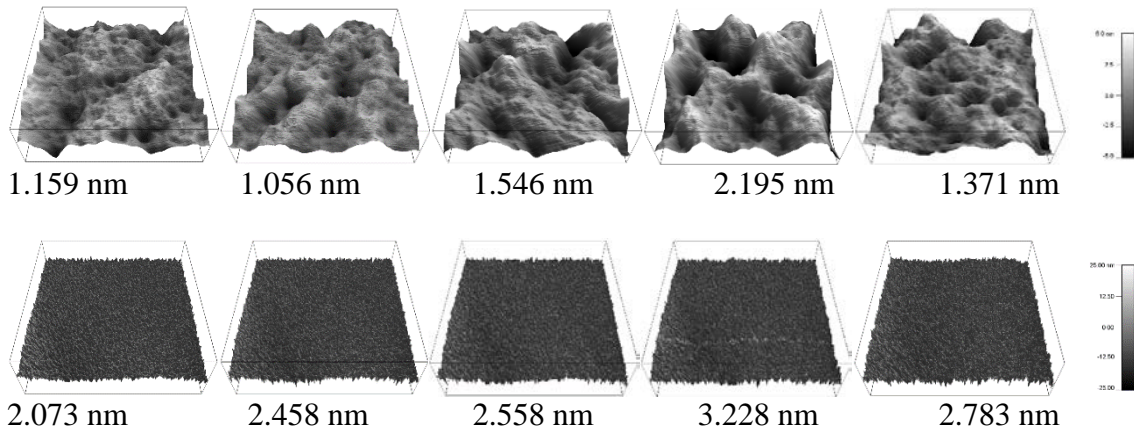


Figure 5.12 These are the 3D representations of the height retraces of the hafnia films on 370 μm thick platinized silicon. The RMS roughness values are shown below each figure.

The relative permittivity along with the dissipation factor for each film are shown measured with 1 V bias at 1 kHz frequency. The relative permittivities of the thinner films (78 nm and 140 nm) are among the highest ever seen for undoped hafnium oxide thin films made by chemical solution deposition. These values are shown in table 5.3 below along with their leakage current at 1.1 V and 1 MV/cm. These values can be compared with those seen in table 5.2. The dissipation factor at this voltage and frequency also shows a decently good quality film. The polarization of each film is plotted as Figure 5.13 and each shows dielectric behavior.

Table 5.3 Shown in this table are the thickness of the hafnia film, the relative permittivity, and the leakage currents at 1.1 V and 1 MV/cm.

thickness of film	relative permittivity	leakage current at 1.1 V	leakage current at 1 MV/cm
78.4 nm	30.4	1.09 $\mu\text{A}/\text{cm}^2$	620.84 $\mu\text{A}/\text{cm}^2$
139.7 nm	32.6	365.78 nA/cm ²	618.01 $\mu\text{A}/\text{cm}^2$
195.3 nm	19.5	97.36 nA/cm ²	311.95 $\mu\text{A}/\text{cm}^2$
253.6 nm	18.5	58.52 nA/cm ²	254.63 $\mu\text{A}/\text{cm}^2$
298.7 nm	20.3	13.15 nA/cm ²	129.10 $\mu\text{A}/\text{cm}^2$

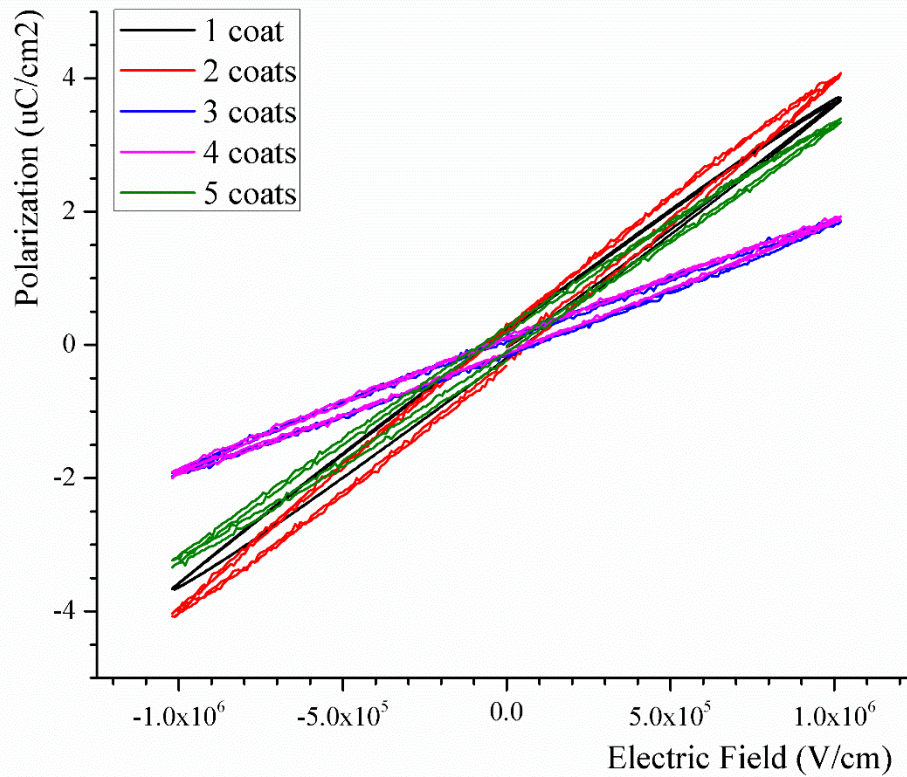


Figure 5.13 These are the polarization curves for each hafnia film up to 1 MV/cm.

For the first time ever, a thin film of hafnia with a high symmetry phase was able to be produced using chemical solution deposition with no dopants with thicknesses greater than 50 nm. These films have among the highest relative permittivities ever seen in hafnia thin films with no dopants and show good leakage behavior and low dissipation factor at the voltage levels used in IC technology. These high symmetry phases were able to be maintained even up to 300 nm thickness which is an order of magnitude more than has ever been seen before.

CHAPTER 6

PRELIMINARY WORK ON THE EFFECTS OF COMPOSITE

HETEROSTRUCTURE ON THE PHASE OF HAFNIA

AND MAGNETIC PROPERTIES OF FERRITE

One of the most interesting properties of hafnium dioxide is that it has been shown that this material is ferroelectric when the correct phase is produced. This material, in ferroelectric form, has been shown to be useful for integration into the FeRAM sector of ICs because of its good temperature stability, electrical and chemical compatibility with silicon, and due to its high coercivity. However, as is a problem with FeRAM, this material would have to be poled in order to read the bit. This would mean destroying the bit in order to access the information stored in each ferroelectric capacitor. In order to work around this, stacking ferroelectric hafnia with nickel ferrite, a good magnetostrictive material, would allow the computer to non-destructively read off the bit. To investigate the compatibility of nickel ferrite and hafnium dioxide, initial studies were done to 1) see how processing the composite affects the non-equilibrium phase of hafnia (using the high symmetry phase previously produced as an example) 2) verify that the magnetic properties of the nickel ferrite layer were either unaffected or improved and 3) to ensure that the two films interfaced well.

In this chapter, the phase retention of hafnium oxide will be studied with and without the stacking of a nickel ferrite layer. This will be qualified by using x-ray diffraction. The magnetic properties of the nickel ferrite layer will then be measured with SQUID and the effect of the composite on these magnetic properties will be seen. Finally, the interface

between the nickel ferrite layer and the hafnia layer will be looked at with cross-sectional TEM. This will inform the ability of these two materials to interface through chemical solution deposition.

6.1 Phase Retention of Hafnia in Composite

To start this study, it was important to start off by spin coating nickel ferrite onto the 370 μm platinized silicon substrate, the 670 μm thick platinized silicon substrate, and the 670 μm thick silicon substrate coated with TiN. The solution chemistry used to synthesize the nickel ferrite precursor solution was to take 1.8174 g of nickel nitrate hexahydrate, 5.05 g of iron nitrate nonahydrate, and 25 mL of 2-methoxyethanol and mix them into a clean 50 mL beaker at 70 $^{\circ}\text{C}$ for 120 min. One major potential pitfall from this synthesis was the formation of Fe_2O_3 . To get rid of any Fe_2O_3 which would precipitate out of solution, the entire solution was centrifuged to 10,000 rpm for 20 minutes. This process pushed the Fe_2O_3 to the bottom of the test tube and allowed for the extraction of only the nickel ferrite solution. Additionally, the entire solution was filtered through a 0.2 μm PTFE filter. This solution was statically dropped onto the platinized silicon, spun at 6000 rpm for 30 seconds with an acceleration of 1064 rpm/s, and then placed into a tube furnace with the exact same annealing conditions that were found in the optimal way to grow high symmetry phase hafnia in section 5.3. The sample was cubic and appeared to have no texture. The GIXRD plots for the nickel ferrite film on 370 μm thick platinized silicon, 670 μm thick platinized silicon, and 670 μm thick silicon coated with TiN are shown as Figure 6.1. The thickness of the film was measured to be 26.3 nm in each case and the XRR plots for these films are shown as Figure

6.2. The roughness of each nickel ferrite film was measured and the AFM height retraces along with their roughnesses are shown as Figure 6.3.

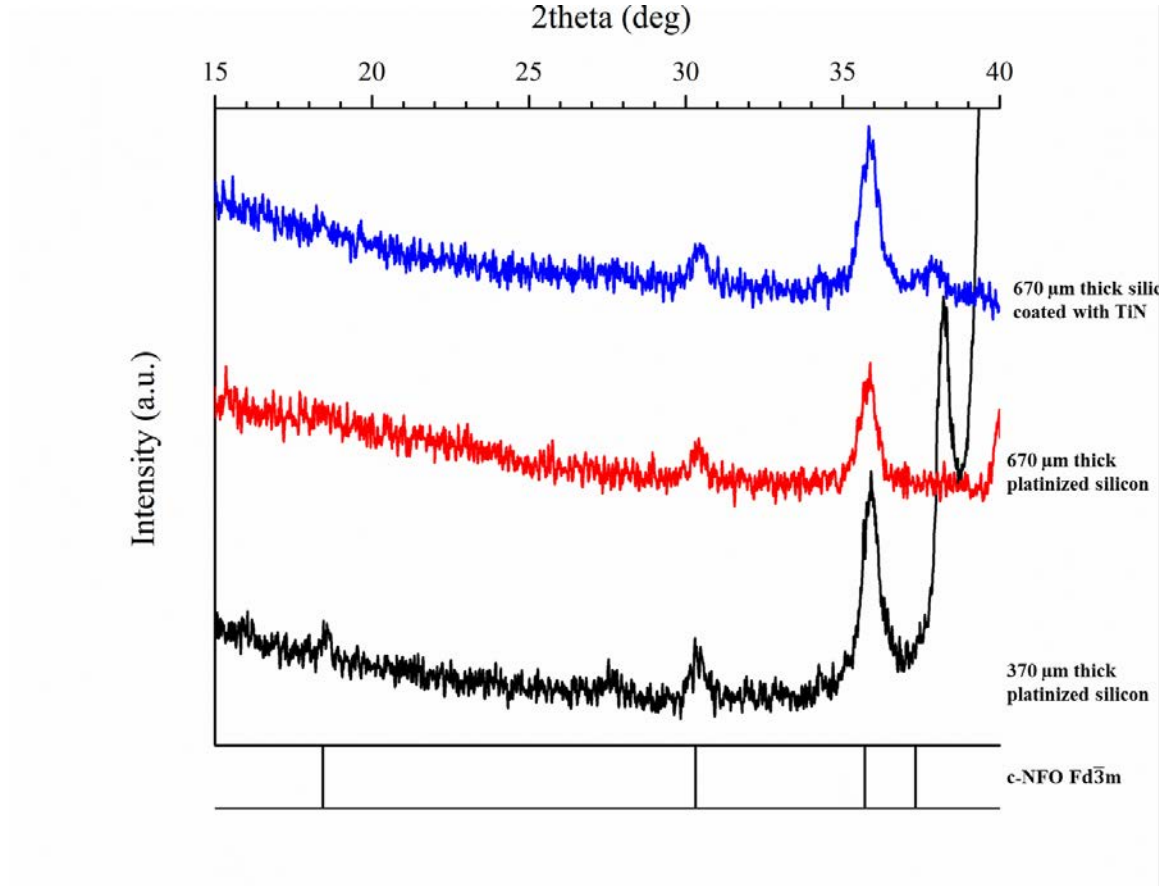


Figure 6.1 This is the GIXRD plot of the nickel ferrite film on various substrates. Shown below the diffraction data are the standard peak positions of the nickel ferrite.

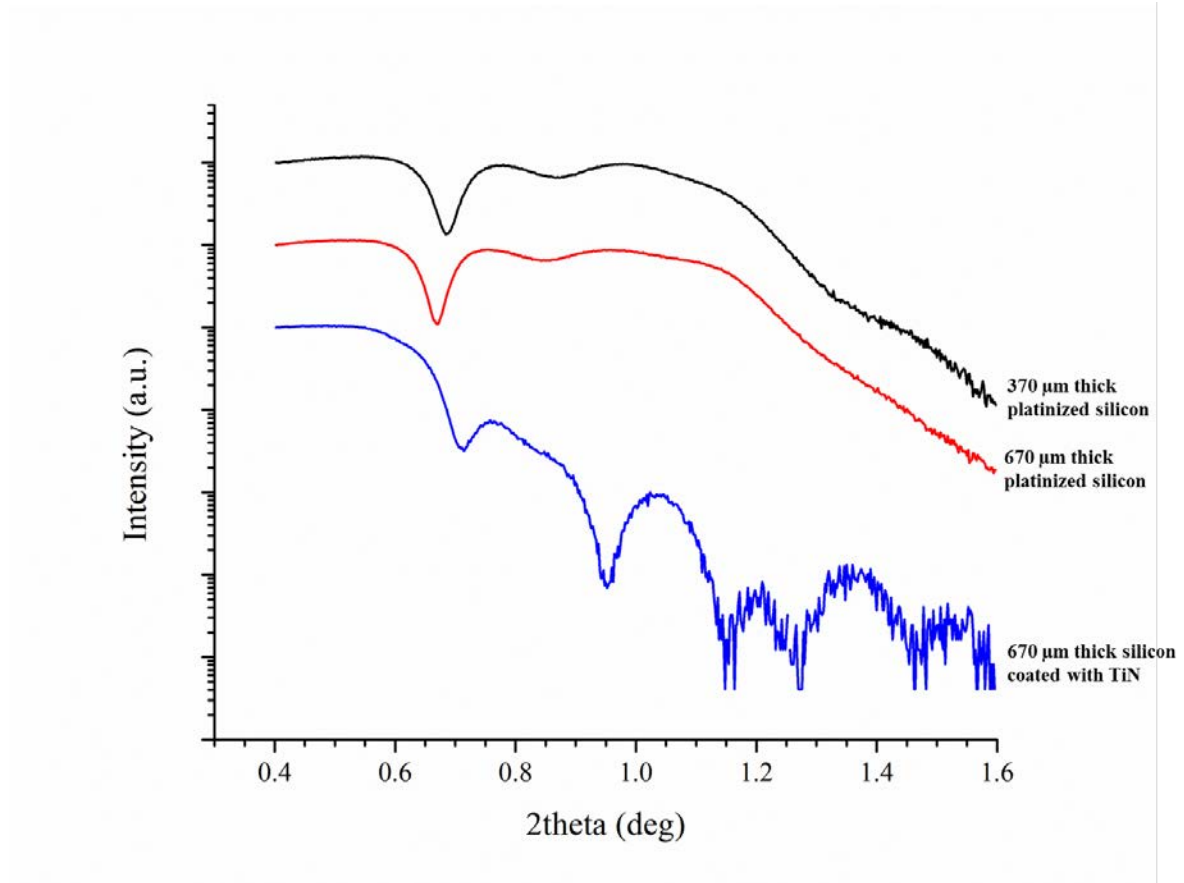


Figure 6.2 This is the XRR spectra for the nickel ferrite film on the marked substrates.

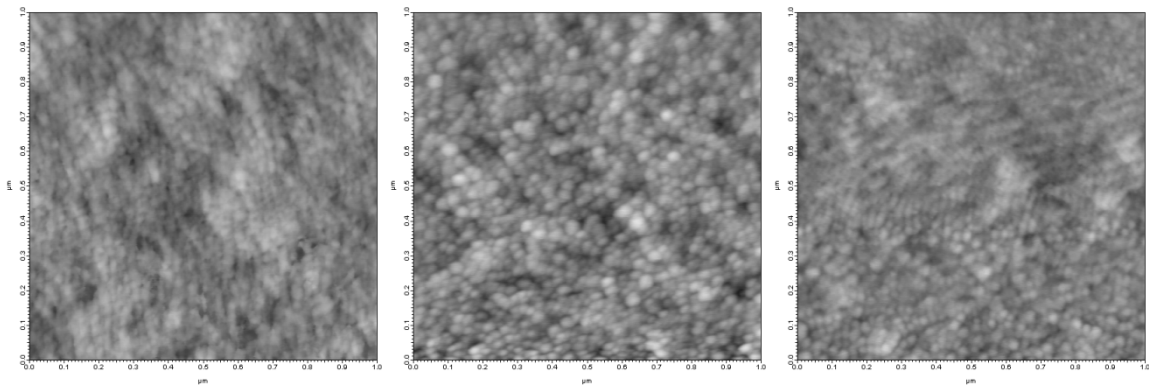


Figure 6.3 These are the height retraces of the nickel ferrite film on a) 370 μm thick platinized silicon, b) 670 μm thick platinized silicon, and c) 670 μm thick silicon coated with TiN.

The composite was formed by coating the platinized silicon substrate with the hafnia film and annealing the film to form the high symmetry phase. The sample was then coated with nickel ferrite using the same annealing procedure. This order was chosen because the glycine in the hafnium oxychloride precursor solution would react with the nickel ferrite layer. Glycine is commonly used as the fuel for a combustion reaction [99] to form nickel ferrite nanopowders and as such limited the stacking order of the hafnia and nickel ferrite. To qualify how the composite affected the phase of the hafnia film, GIXRD was used. Unfortunately, the peaks for nickel ferrite and cubic hafnia overlap (for NFO the 220 diffraction peak is at 30.31° and the 311 is at 35.70° ; for hafnia the 111 diffraction peak is at 30.56° and the 200 is at 35.43°). Due to these diffraction peak position overlaps, the easiest way of knowing how the composite affected the phase was to look at the change in intensity for the monoclinic peaks of hafnia. The diffraction data for the composite is shown below as Figure 6.4. From these data, it appears as though stacking the nickel ferrite causes a phase change in the hafnia toward the monoclinic phase. There still exist small diffraction peaks that coincide with the position of peaks for cubic hafnia but it is difficult to elucidate whether these are nickel ferrite peaks or from the hafnia thin film.

To verify whether the phase change came from an additional heat treatment or from the nickel ferrite layer being stacked on top, a hafnia film was synthesized and given an additional heat treatment with only one coat. These data are shown below as Figure 6.5, Figure 6.6, and Figure 6.7 for hafnia grown on $370\ \mu\text{m}$ thick platinized silicon, $670\ \mu\text{m}$ thick platinized silicon, and $670\ \mu\text{m}$ thick silicon with a TiN coating, respectively. These data

show that the hafnia film grown on the 370 μm thick platinized silicon remained unchanged even after the second heat treatment. The phase of the hafnia film grown on the other two substrates did change to a nearly pure monoclinic phase. This result shows that the phase change seen in the composite on the 370 μm thick platinized silicon substrate is most likely due to the additional layer on top of the hafnia and not due to the additional energy given to the system. The reasoning behind this is not understood. Although the lattice mismatch between the hafnia and nickel ferrite layer is large (lattice parameters for hafnia given in section 5.1, lattice constant for NFO is 8.34 Å [100]), the effect of a large lattice mismatch doesn't affect the hafnia phase formed. The phase change seen in the composites grown on the thicker substrates can be understood to be from an additional heat treatment although stacking the NFO on top of the hafnia layer may also affect the phase change.

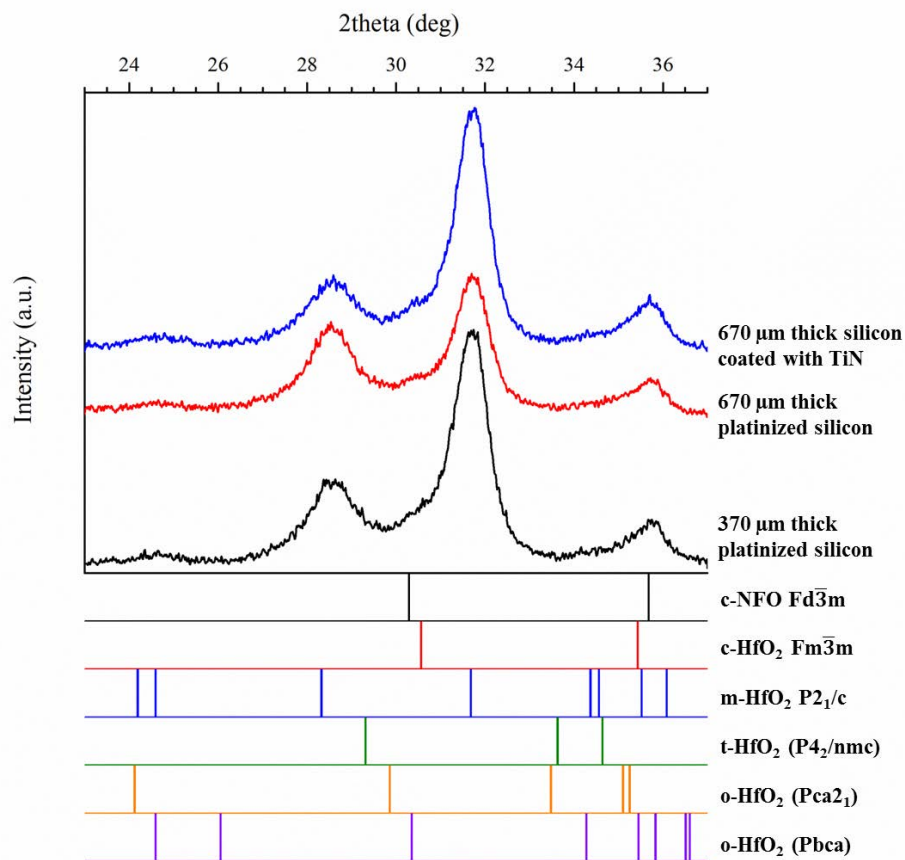


Figure 6.4 This is a set of GIXRD plots for the nickel ferrite thin film stacked on top of the hafnia film. The substrate for each GIXRD plot is shown. Also shown are the standard peak positions for the nickel ferrite film and the phases of hafnia all marked with the appropriate space group.

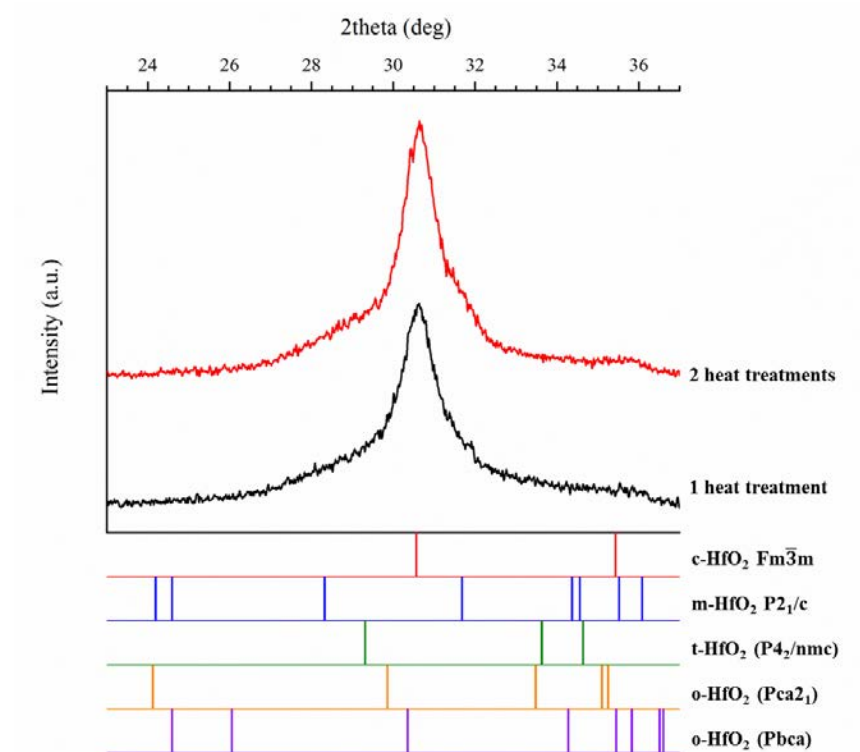


Figure 6.5 This is the GIXRD plot of hafnia films on 370 μm thick platinized silicon that have been annealed once and twice as marked on the plot. Shown below the plot are the standard peak positions for each phase of hafnia.

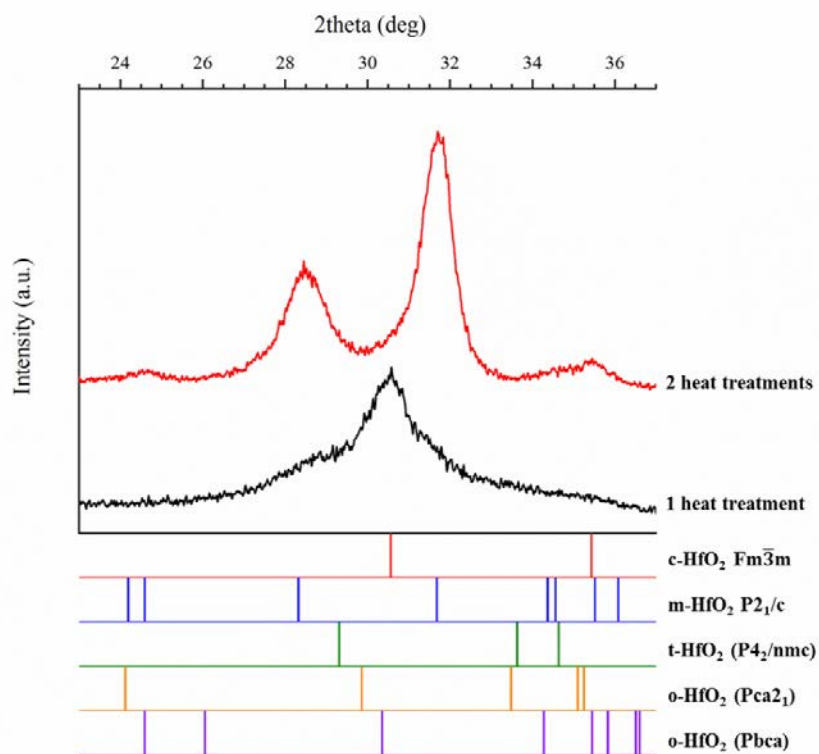


Figure 6.6 This is the GIXRD plot of hafnia films on 670 μm thick platinized silicon that have been annealed once and twice as marked on the plot. Shown below the plot are the standard peak positions for each phase of hafnia.

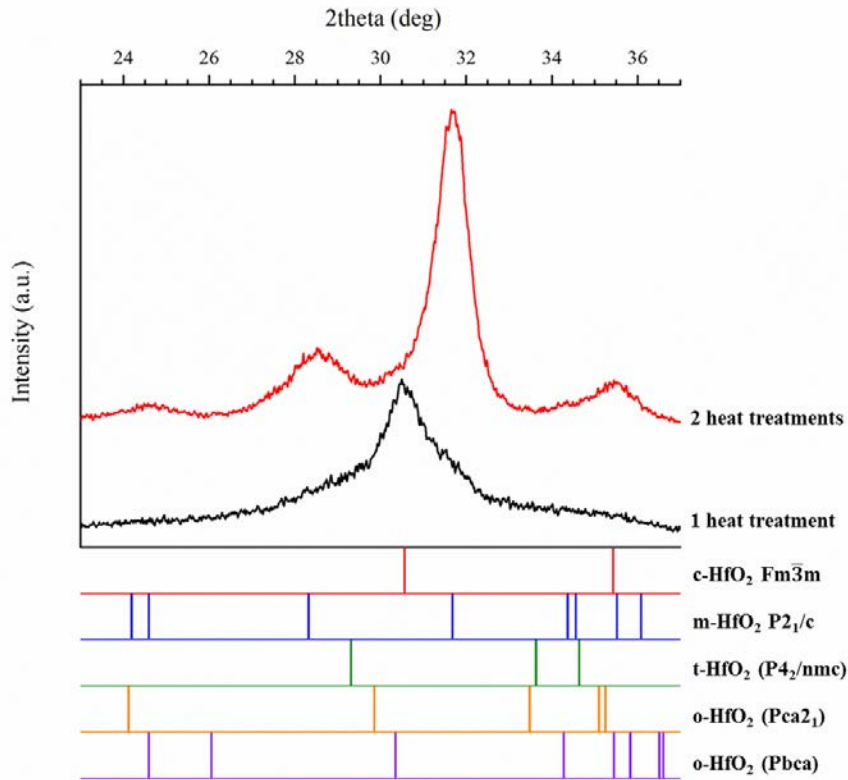


Figure 6.7 This is the GIXRD plot of hafnia films on 670 μm thick silicon with a TiN coating that have been annealed once and twice as marked on the plot. Shown below the plot are the standard peak positions for each phase of hafnia.

Although the phase of the hafnia film changed to mostly monoclinic in all the composites, the properties of the film were measured to gain an understanding into the phase change. The quality was measured by doing AFM on the composite and cross-sectional TEM to see the interface. The height retraces from the AFM are shown as Figure 6.8 and the roughness values are shown for each composite. The AFM height retraces show that the composite grown on the 370 μm thick platinized silicon substrate have a larger roughness than just the hafnia layer. The roughnesses of the composite on the other two substrates don't seem to have an increase in surface roughness. The fact that the phase change in the hafnia layer in the composite on the 370 μm thick platinized silicon is accompanied by a large roughness

increase and that the phase doesn't change on this thickness substrate from an additional heat treatment alludes to the fact that there may be a reaction between the layers. With the larger thickness substrates, this interaction doesn't seem to occur because the roughness remains the same. To try to understand this interaction, an image of the TEM cross-section of the composite grown on 370 μm thick platinized silicon is shown as Figure 6.9. The layers are labeled in the image. The microstructure of the hafnia layer appears as though the grain structure is very fine. The grain structure of the ferrite layer shows fairly large grains. The interface between the two layers is poor and it appears as though the layers do not interface well. This is evidenced by the white spots in the image which are indicative of pure transmission of the electrons with no scattering. Therefore, this method of deposition of the layers is not effective for a ferromagnetic and ferroelectric layer comprised of ferrites and hafnia.

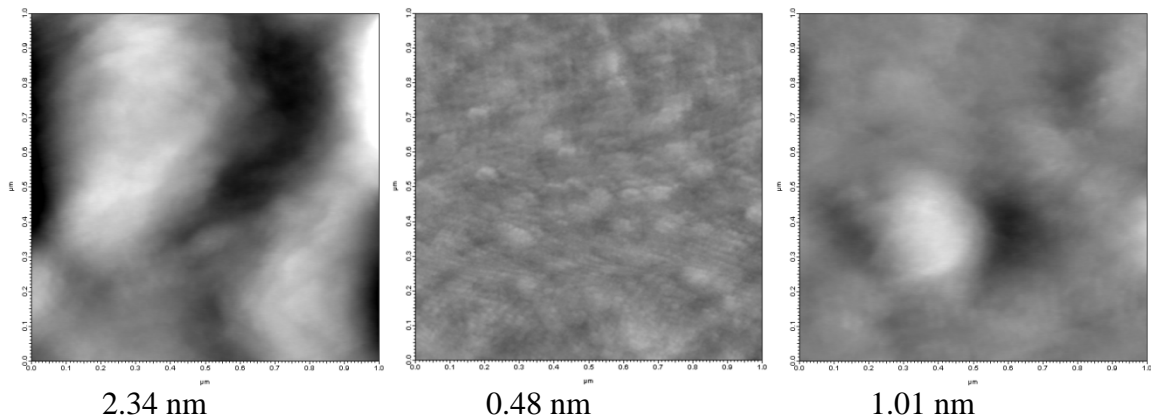


Fig 6.8 These are the height retraces of the nickel ferrite layer stacked on top of the hafnia layer on a) a 370 μm thick platinized silicon substrate, b) a 670 μm thick platinized silicon substrate, and c) a 670 μm thick silicon substrate coated with TiN.

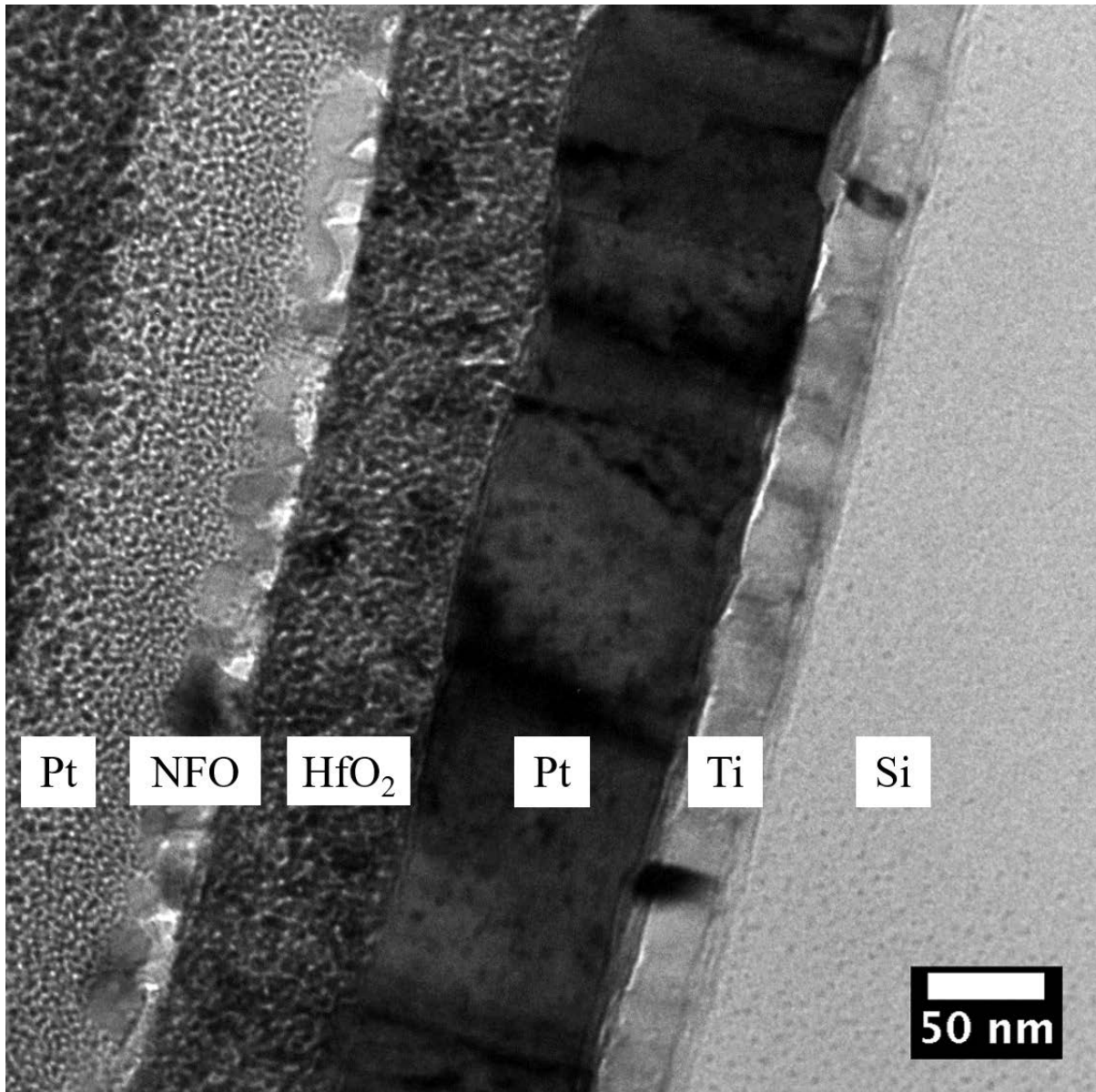


Figure 6.9 This is a bright field TEM cross section of the composite. Each layer is labeled. The platinum layer shows large grains while the hafnium dioxide layer is very fine grained. The nickel ferrite layer does not appear to interface well with the hafnia as evidenced by the bright spots which are indicative of voids. The grain structure of the nickel ferrite is also much larger than that of the hafnia.

6.2 Effects of Composite on Magnetic Properties

The magnetic properties of these ferrite films was measured using the SQUID. The sample was measured in VSM mode at 300 K. The magnetic hysteresis curves are shown below as Fig 6.10, Figure 6.11, and Figure 6.12 for the plain nickel ferrite film and the composite on 370 μm thick platinized silicon, 670 μm platinized silicon, and 670 μm thick silicon coated with TiN, respectively. Extracted from these curves are the saturation magnetization, the remanent magnetization, and the coercivity of the plain NFO film and the composite for each substrate. These data are shown below in table 6.1.

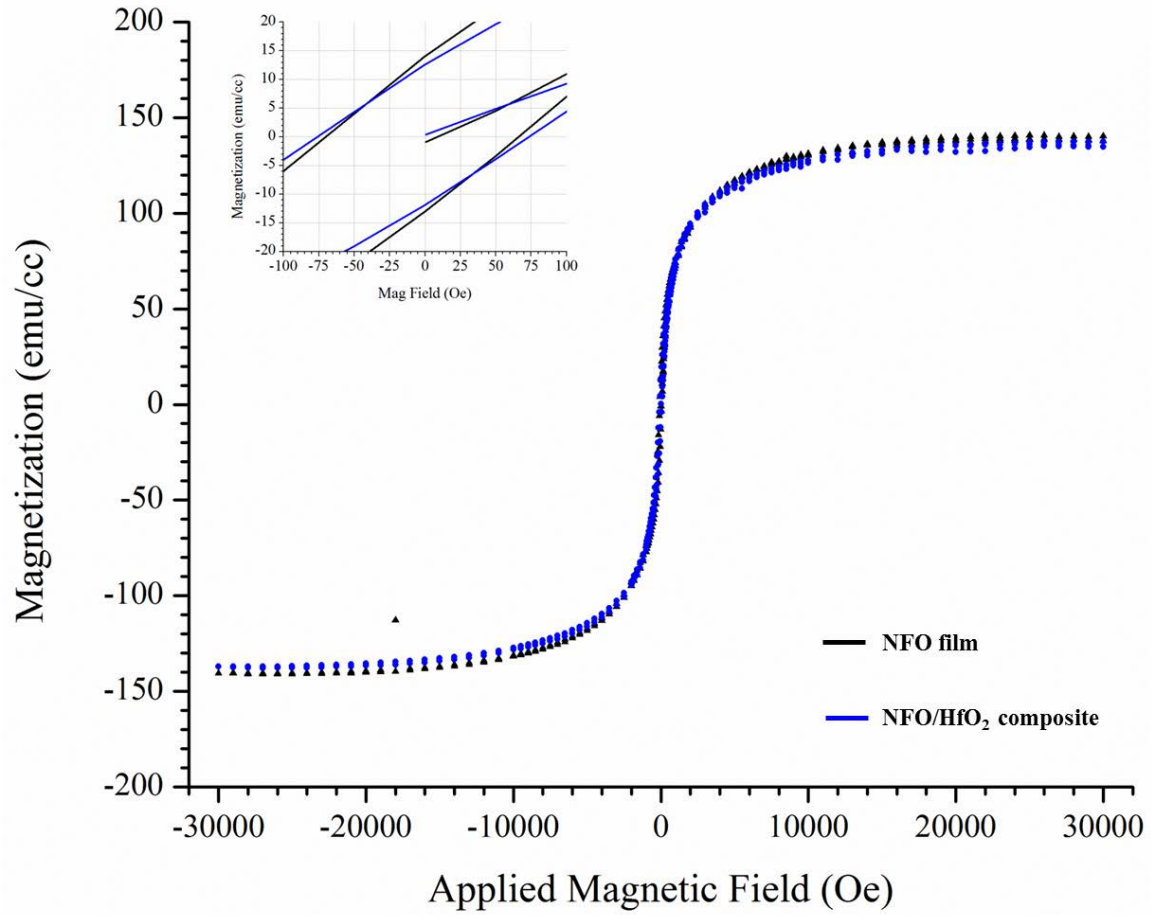


Figure 6.10 This is a plot of the magnetization of pure nickel ferrite and the nickel ferrite/hafnia composite on 370 μm thick platinized silicon with an inset showing the remanent magnetization and coercive fields.

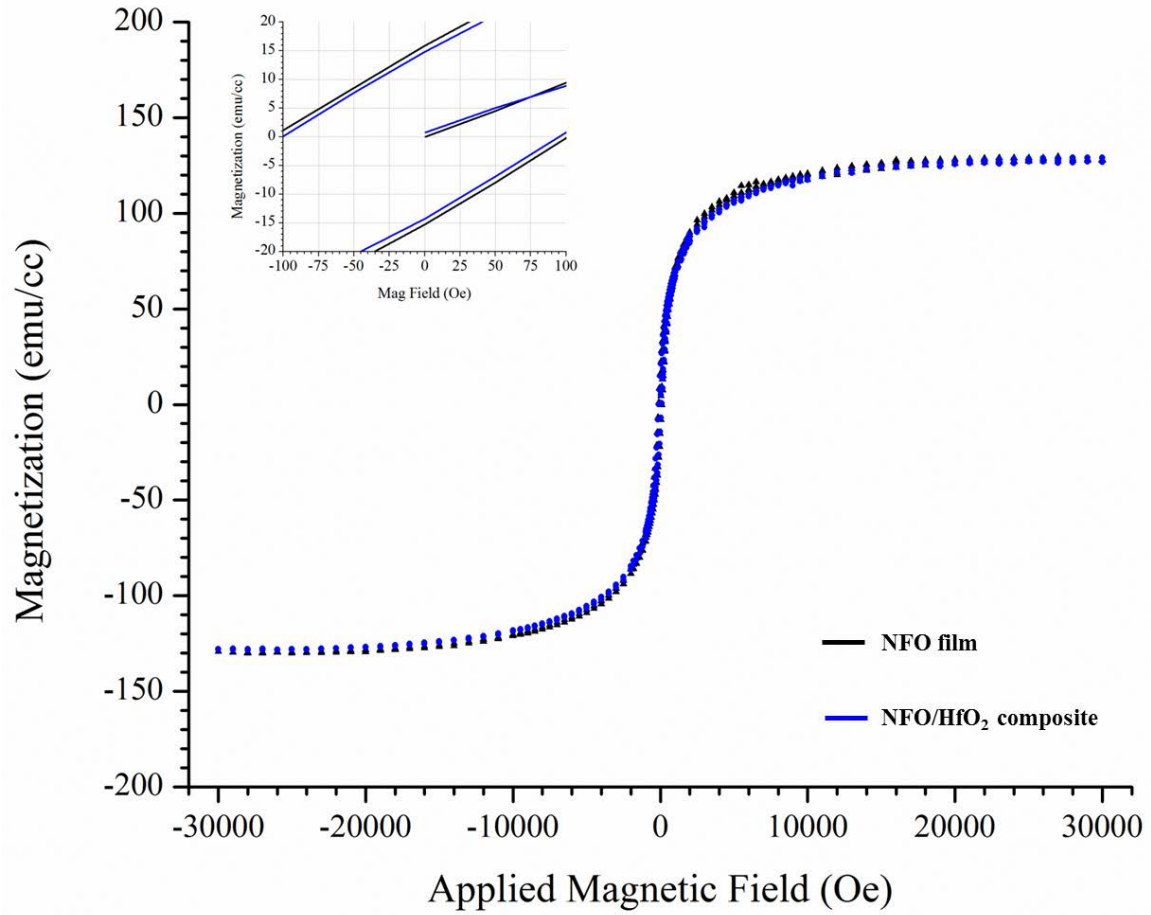


Figure 6.11 This is a plot of the magnetization of pure nickel ferrite and the nickel ferrite/hafnia composite on 670 μm thick platinized silicon with an inset showing the remanent magnetization and coercive fields.

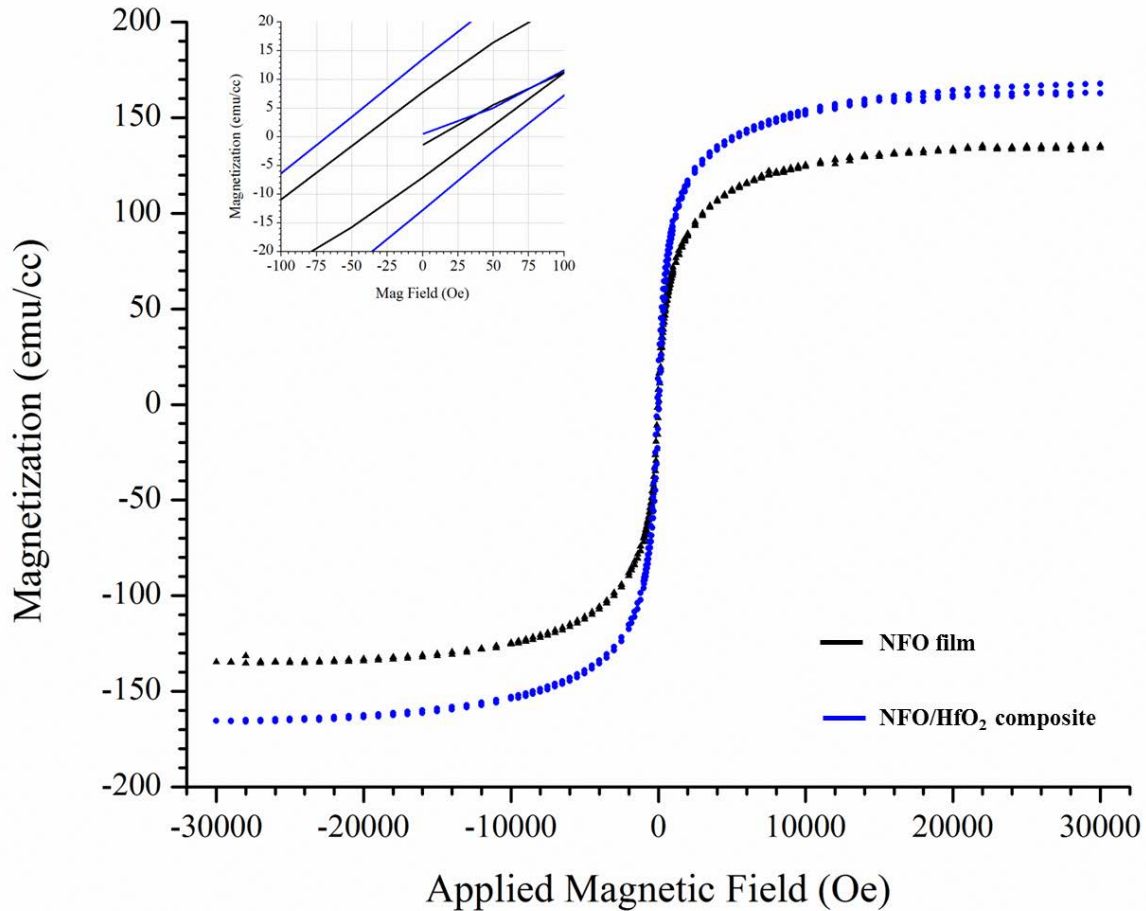


Figure 6.12 This is a plot of the magnetization of pure nickel ferrite and the nickel ferrite/hafnia composite on 670 μm thick silicon coated with TiN with an inset showing the remanent magnetization and coercive fields.

The magnetic properties of the ferrite layer barely changed between the ferrite film alone versus the composite when the films were grown on platinized silicon regardless of the thickness. The magnetic properties of the composite change drastically as compared to the plain nickel ferrite layer when the stack was grown on the titanium nitride coated silicon. The reason behind this is not understood and would require further study to elucidate the reason. The variation in magnetic properties between the NFO films on each substrate is also not fully understood and would require further study.

Table 6.1 This table shows the magnetization data pulled from the hysteresis curves for NFO and the NFO/HfO₂ composites.

	Coercivity (Oe)	Remanent Magnetization (emu/cc)	Saturation Magnetization (emu/cc)
NFO on 370 μm platinized Si	68.3 ± 5.2	13.7 ± 1.3	138.5 ± 6.7
composite on 370 μm platinized Si	75.0 ± 11.1	12.2 ± 1.8	134.8 ± 17.9
NFO on 670 μm platinized Si	105.5 ± 16.0	15.7 ± 0.3	128.5 ± 9.6
composite on 670 μm platinized Si	99.0 ± 18.4	14.6 ± 1.4	136.8 ± 14.9
NFO on 670 μm TiN coated Si	40.4 ± 3.9	7.5 ± 1.4	134.0 ± 12.7
composite on 670 μm TiN coated Si	63.0 ± 23.0	13.3 ± 1.8	178.23 ± 33.8

Based on these values, the saturation magnetization in all plain nickel ferrite films was about half that of the bulk value from literature stated earlier yet higher than that reported by [101]. This means there is likely still a lot of amorphous phase left in the film. The coercivity in most of these cases was lower than that of nickel ferrite films reported in literature without heavy processing optimization. These values of coercivity are ~ 100 Oe and ~ 200 Oe reported by [101], [102], respectively.

Although this work is very preliminary, the results of this chapter bring up several questions which are interesting to investigate. The data here show that the nickel ferrite layer heavily affects the phase stability of the hafnia phase. Because the TEM cross-section shows an incoherent interface between the hafnia and the ferrite, it is not understood why this phase change occurs. Further study here would show whether these two materials can be well interfaced for future use in magnetoelectrics or other applications.

The magnetic properties of the nickel ferrite layer seem to be unaffected by the addition of the hafnia layer. However, when the composite is grown on a silicon substrate with a TiN intermediary layer, the magnetic properties are greatly affected. This difference is worth studying as most work with hafnia uses a titanium nitride electrode [6], [103], [104].

CHAPTER 7

SUMMARY OF WORK

The high symmetry phases of hafnium dioxide have applications as a high-k dielectric which is commonly used as a gate oxide in CMOS and as the insulating material between plates in a capacitor due to the higher relative permittivities seen in the high symmetry phases (cubic, tetragonal, orthorhombic). It is also believed that the higher symmetry phases can be electric field cycled to form the non-centrosymmetric phase of hafnia which has been shown to be ferroelectric. A facile method for producing the high symmetry phases is desired because the cost of vacuum based deposition techniques is high and the ability to quickly vary stoichiometry is difficult. What has been shown in the preceding chapters is a way to produce these high symmetry phases of hafnia without dopants using chemical solution deposition. Additionally, these high symmetry phases of hafnia are maintained at large thicknesses (300 nm) which have never been seen before.

In chapter 4, the optimization of the production of these high symmetry phase thin films of hafnia was studied. To begin, a solution contacting hafnium oxychloride and glycine in deionized water was synthesized. This 1.8 M solution was then spun onto c-cut sapphire substrates and annealed at a variety of temperatures via rapid thermal processing. The qualification for success was the appearance of a diffraction peak in XRD corresponding to the high symmetry phases of hafnia. This was achieved at 725 °C in air when annealed for 3 minutes. For further optimization, the necessary ramp rate to achieve these phases was studied. This was done by assuming that the alumina boat was the main source of heat to the

sample. This was a safe assumption since the sample was in direct contact with a preheated alumina boat. To vary the ramp rate, the alumina boat was preheated and then allowed to cool to a certain temperature. The sample was then placed in the boat. This study showed that the appropriate ramp rate was to go from room temperature to 480 °C in a matter of seconds. The second thing that the study showed is that the phase of the thin film was very sensitive to small changes in that ramp rate. When going from room temperature to 520 °C in a few seconds, the monoclinic phase of hafnia began to be produced in appreciable quantities. The last portion of chapter 3 focused on the effect of solution concentration on the phase produced in the thin film. This showed that with low concentrations, the character of the film was mostly amorphous. When the concentration was too high, the monoclinic phase appeared in large quantities. At a 2 M concentration, the high symmetry phase diffraction peak for hafnia appeared while suppressing the monoclinic phase.

Chapter 5 focused on further optimization of the hafnia thin films except deposited on silicon instead of sapphire. This is because the desire for devices is to interface the hafnia with silicon. The electrical properties of the hafnia films were then measured to qualify the films followed by a look into phase retention at high thin film thicknesses. Because the thermal conductivity and lattice parameter of silicon is different than that of sapphire, the hafnium oxychloride solution was deposited onto the substrate and the phase was measured as a function of substrate thickness (to understand the effects of thermal conductivity) and with different intermediary layers (to understand the effects of lattice parameters). Due to the higher thermal conductivity of silicon, it was expected that to achieve the same phase of

hafnia as seen in the sapphire, a greater thickness of silicon was needed. This was found to be the case as the hafnia film deposited on 670 μm thick silicon yielded the high symmetry phase and the hafnia film deposited on 450 μm thick silicon (the same thickness as the sapphire) showed a large portion of monoclinic phase. Unexpectedly, the hafnia films deposited on even thinner silicon substrates (370 μm and 280 μm thick silicon) did not show the monoclinic phase in x-ray diffraction. Instead, these films showed the high symmetry phase of hafnia as well.

To verify whether the lattice parameters also played a role in the phase produced in the hafnia thin films, intermediary layers of platinum and titanium nitride were deposited on the silicon substrates. This portion of the study showed that there was little to no effect on the phase produced with different intermediary layers insinuating that the lattice parameter either played no role in the phase produced or such a small role that it was not noticeable.

The electrical properties of the films were then measured by deposited top electrodes on the hafnia film and then measuring the capacitance, dissipation factor, leakage current, polarization, and the transient current. These measurements showed that the hafnia films deposited on the thicker platinized silicon showed very high dielectric constant (~ 59 at 100 Hz to ~ 26 at 1 MHz) although the dissipation factor made these films unusable. The hafnia films deposited on the thinner platinized silicon showed high dielectric constant (~ 33 at 100 Hz to ~ 27 at 1 MHz) while having a small dissipation factor which make these films electrically high quality. Additionally, the roughness and thickness of all of these films were

measured using AFM and XRR, respectively. The leakage currents of these films showed that they were higher than that of the best hafnia films produced in literature. The leakage current, at 10^{-4} A/cm², is still low enough for use as a gate oxide.

The thickness of these films was then increased by utilizing a layer by layer process up to 300 nm. The films showed a high symmetry phase still present even at larger thicknesses. However, the electrical properties showed a dielectric constant in the range of 30 with film thicknesses up to 150 nm while the thicker films showed a dielectric constant in the range of 20. This means that there is, most likely, the presence of the monoclinic phase in these thicker films. The leakage currents of each of these stayed in the range of 10^{-4} A/cm².

In chapter 6, some preliminary work into the properties of a composite structure of the hafnia and nickel ferrite was done. This showed that the nickel ferrite, by itself, showed similar magnetic properties when compared to literature. This film was also polycrystalline and had low roughness values. When the nickel ferrite was stacked on top of the high symmetry phase thin film of hafnia, there was a phase change in the hafnia film to the monoclinic phase. To verify whether it was a product of the composite or the additional heat treatment, hafnia films grown on 370 μ m thick platinized silicon, 670 μ m thick platinized silicon, and 670 μ m thick silicon coated with TiN were subjected to an additional heat treatment. X-ray diffraction showed that the phase of the hafnia film grown on the 370 μ m thick platinized silicon did not change with the additional heat treatment. The phase of the hafnia film did change with the additional heat treatment on the thicker substrates. This means that, for the

composite on the 370 μm thick platinized silicon substrate, the phase change is probably due entirely to the addition of the nickel ferrite layer and not due to the extra thermal energy delivered to the system.

Although the phase of the hafnia film changed with the addition of the ferrite film, the magnetic properties of the ferrite film were unchanged from the plain nickel ferrite film to the composite structure. This is indicative of a similar microstructure and unchanged stoichiometry in the ferrite film. Because of this, it is likely that there is no diffusion of elements between the nickel ferrite and the hafnia layer.

To qualify the quality of the deposition and the interface between the two layers, the composite was analyzed with TEM. This showed that the hafnia film had a very small grain structure and interfaced well with the platinum layer on the silicon. The ferrite layer, however, appeared to have voids in the film and voids along the hafnia ferrite interface. This is indicative of poor coupling between the two layers and means further work must be done to optimize these two layers.

For further study, the chemistry of the nickel ferrite and hafnium dioxide precursor solutions could be changed to allow for better interfacing of the two materials. Once these two materials interface well, the magnetic properties would be examined to ensure no negative effects to the ferrite layer and then secondary ion mass spectroscopy would be used to confirm no diffusion between the films. If these two materials interfaced well together, the

ferroelectric form of hafnia could be combined with a nickel ferrite thin film for use in a non-destructive read processing for ferroelectric RAM. This would expedite the use of hafnia for FeRAM in consumer devices. Additionally, the magnetodielectric properties of this composite should be studied. Magnetodielectrics are useful for antenna applications as their dielectric constant changes as a function of applied magnetic field. Lastly, due to the stability of the high symmetry phase of hafnia on the 370 μm thick silicon substrates, a titanium nitride intermediary layer should be used instead of platinum to induce the ferroelectric phase. It has been theorized that the ferroelectric phase of hafnia can't be induced on metal bottom electrodes unless the grain size of the electrode is smaller than 30 nm. The platinized silicon in this study had a grain size of greater than 30 nm which may preclude the formation of the ferroelectric phase of hafnia.

REFERENCES

- [1] V. V. Kaichev, T. P. Smirnova, L. V. Yakovkina, E. V. Ivanova, M. V. Zamoryanskaya, A. A. Saraev, V. A. Pustovarov, T. V. Perevalov, and V. A. Gritsenko, “Structure, chemistry and luminescence properties of dielectric $\text{La}_{0.9}\text{Hf}_{0.1}\text{O}_3$ films,” *Mater. Chem. Phys.*, vol. 175, pp. 200–205, 2016.
- [2] U. Schroeder, T. Schenk, H. Mulaosmanovic, S. Slesazeck, J. Ocker, C. Richter, E. Yurchuk, K. Khullar, P. Polakowski, E. D. Grimley, J. M. Lebeau, S. Flachowsky, S. Jansen, S. Kolodinski, R. Van Bentum, A. Kersch, and T. Mikolajick, “Impact of field cycling on HfO_2 based non-volatile memory devices,” pp. 364–368, 2016.
- [3] S. Uwe, Y. Ekaterina, M. Johannes, M. Dominik, S. Tony, P. Patrick, A. Christoph, I. P. Mihaela, V. K. Sergei, and M. Thomas, “Impact of different dopants on the switching properties of ferroelectric hafniumoxide,” *Jpn. J. Appl. Phys.*, vol. 53, no. 8S1, p. 08LE02, 2014.
- [4] M. Hoffmann, U. Schroeder, T. Schenk, T. Shimizu, H. Funakubo, O. Sakata, D. Pohl, M. Drescher, C. Adelmann, R. Materlik, A. Kersch, and T. Mikolajick, “Stabilizing the ferroelectric phase in doped hafnium oxide,” *J. Appl. Phys.*, vol. 118, no. 7, 2015.
- [5] S. Starschich and U. Boettger, “An extensive study of the influence of dopants on the ferroelectric properties of HfO_2 ,” *J. Mater. Chem. C*, 2017.
- [6] P. Polakowski, J. Müller, and J. Muller, “Ferroelectricity in undoped hafnium oxide,” *Appl. Phys. Lett.*, vol. 106, no. 23, p. 232905, 2015.
- [7] S. Starschich, D. Griesche, T. Schneller, and U. Böttger, “Chemical Solution Deposition of Ferroelectric Hafnium Oxide for Future Lead Free Ferroelectric

- Devices,” *ECS J. Solid State Sci. Technol.*, vol. 4, no. 12, pp. P419–P423, 2015.
- [8] A. Pal, V. K. Narasimhan, S. Weeks, K. Littau, D. Pramanik, and T. Chiang, “Enhancing ferroelectricity in dopant-free hafnium oxide,” *Appl. Phys. Lett.*, vol. 110, no. 2, p. 22903, 2017.
- [9] G. Gautschi, “Piezoelectric Sensors,” in *Piezoelectric Sensorics: Force Strain Pressure Acceleration and Acoustic Emission Sensors Materials and Amplifiers*, Berlin, Heidelberg: Springer Berlin Heidelberg, 2002, pp. 73–91.
- [10] E. F. CRAWLEY and J. DE LUIS, “Use of piezoelectric actuators as elements of intelligent structures,” *AIAA J.*, vol. 25, no. 10, pp. 1373–1385, Oct. 1987.
- [11] J. Rastegar, C. Pereira, and H.-L. Nguyen, “Piezoelectric-based power sources for harvesting energy from platforms with low-frequency vibration,” 2006, vol. 6171, pp. 617101–617107.
- [12] K. N. and M. A. and C.-N. X. and T. H. and M. K. and A. Takase, “Enhanced Photovoltaic Response in Lead Lanthanum Zirconate-Titanate Ceramics with A-Site Deficient Composition for Photostrictor Application,” *Jpn. J. Appl. Phys.*, vol. 39, no. 9R, p. 5144, 2000.
- [13] I. K. Yoo and S. B. Desu, “Mechanism of Fatigue in Ferroelectric Thin Films,” *Phys. Status Solidi*, vol. 133, no. 2, pp. 565–573, 1992.
- [14] K. OKAZAKI and K. NAGATA, “Effects of Grain Size and Porosity on Electrical and Optical Properties of PLZT Ceramics,” *J. Am. Ceram. Soc.*, vol. 56, no. 2, pp. 82–86, Feb. 1973.
- [15] J. F. Scott, *Ferroelectric Memories*. Springer-Vellag Berlin Heidelberg, 2000.

- [16] P. G. Dargie, N. R. Harris, N. M. White, J. K. Atkinson, and R. P. Sion, "Characterisation of screen printable piezoelectric thick-films," in *Eighth Conference on Sensors and their Applications*, 2007.
- [17] Q. M. Zhang, W. Y. Pan, and L. E. Cross, "Laser interferometer for the study of piezoelectric and electrostrictive strains," *J. Appl. Phys.*, vol. 63, no. 8, pp. 2492–2496, 1988.
- [18] B. D. Cullity and C. D. Graham, *Introduction to Magnetic Materials*. 2009.
- [19] Y. Suzuki, G. Hu, R. B. B. van Dover, and R. J. J. Cava, "Magnetic anisotropy of epitaxial cobalt ferrite thin films," *J. Magn. Magn. Mater.*, vol. 191, no. 1–2, pp. 1–8, 1999.
- [20] E. R. Callen and H. B. Callen, "Static Magnetoelastic Coupling in Cubic Crystals," *Phys. Rev.*, vol. 129, no. 2, pp. 578–593, 1963.
- [21] C. W. Nan, M. I. Bichurin, S. Dong, D. Viehland, and G. Srinivasan, "Multiferroic magnetoelectric composites: Historical perspective, status, and future directions," *J. Appl. Phys.*, vol. 103, no. 3, 2008.
- [22] I. E. Dzyaloshinskii, "On the Magneto-Electrical Effect in Antiferromagnets," *Sov. Phys. J. Explor. Theor. Phys.*, vol. 37, no. 3, pp. 881–882, 1960.
- [23] D. N. Astrov, "The Magnetoelectric Effect in Antiferromagnetics," *Sov. Phys. J. Explor. Theor. Phys.*, vol. 11, no. 3, pp. 984–985, 1960.
- [24] N. A. Hill, "Why Are There so Few Magnetic Ferroelectrics?," *J. Phys. Chem. B*, vol. 104, no. 29, pp. 6694–6709, 2000.
- [25] T. Kimura, T. Goto, H. Shintani, K. Ishizaka, T. Arima, and Y. Tokura, "Magnetic

- control of ferroelectric polarization,” *Nature*, vol. 426, no. 6962, pp. 55–58, Nov. 2003.
- [26] T. Goto, T. Kimura, G. Lawes, A. P. Ramirez, and Y. Tokura, “Ferroelectricity and Giant Magnetocapacitance in Perovskite Rare-Earth Manganites,” *Phys. Rev. Lett.*, vol. 92, no. 25, p. 257201, Jun. 2004.
- [27] W. P. and M. P. S. and P. Murugavel, “The single-phase multiferroic oxides: from bulk to thin film,” *J. Phys. Condens. Matter*, vol. 17, no. 30, p. R803, 2005.
- [28] J. Wang, J. B. Neaton, H. Zheng, V. Nagarajan, S. B. Ogale, B. Liu, D. Viehland, V. Vaithyanathan, D. G. Schlom, U. V. Waghmare, N. A. Spaldin, K. M. Rabe, M. Wuttig, and R. Ramesh, “Epitaxial BiFeO₃ Multiferroic Thin Film Heterostructures,” *Science* (80-.), vol. 299, no. 5613, pp. 1719–1722, 2003.
- [29] P. Lukashev, R. F. Sabirianov, and K. Belashchenko, “Theory of the piezomagnetic effect in Mn-based antiperovskites,” *Phys. Rev. B*, vol. 78, p. 184414, 2008.
- [30] A. M. J. G. Van Run, D. R. Terrell, and J. H. Scholing, “An in situ grown eutectic magnetoelectric composite material - Part 2 Physical properties,” *J. Mater. Sci.*, vol. 9, no. 10, pp. 1710–1714, 1974.
- [31] G. Srinivasan, C. P. DeVreugd, R. Hayes, M. I. Bichurin, and V. M. Petrov, “Magnetoelectric Effects in Ferromagnetic and Piezoelectric Multilayer Composites,” in *Magnetoelectric Interaction Phenomena in Crystals*, 2004, pp. 35–55.
- [32] M. J. Dapino, F. T. Calkins, and A. B. Flatau, “On identification and analysis of fundamental issues in Terfenol-D transducer modeling,” in *Proceedings SPIE Smart Structural Materials Conference*, 1998.

- [33] C. Nan, M. Li, and J. Huang, “Calculations of giant magnetoelectric effects in ferroic composites of rare-earth–iron alloys and ferroelectric polymers,” *Phys. Rev. B*, vol. 63, pp. 1–9, 2001.
- [34] S. Masui, W. Yokozeki, M. Oura, T. Ninomiya, K. Mukaida, Y. Takayama, and T. Teramoto, “Design and applications of ferroelectric nonvolatile SRAM and flip-flop with unlimited read/program cycles and stable recall,” in *IEEE Custom Integrated Circuits Conference*, 2003, p. 403.
- [35] T. D. Huan, V. Sharma, G. A. Rossetti, and R. Ramprasad, “Pathways towards ferroelectricity in hafnia,” *Phys. Rev. B*, vol. 90, no. 6, p. 64111, 2014.
- [36] J. Robertson, “High dielectric constant gate oxides for metal oxide Si transistors,” *Reports Prog. Phys.*, vol. 69, no. 2, pp. 327–396, 2005.
- [37] H. Liang, J. Xu, D. Zhou, X. Wang, X. Liu, S. Chu, and X. Liu, “Structure and electrical properties of pure and yttrium-doped HfO₂ films by chemical solution deposition through layer by layer crystallization process,” *Mater. Des.*, vol. 120, pp. 376–381, 2017.
- [38] T. S. Böske, J. Müller, D. Bräuhäus, U. Schröder, and U. Böttger, “Ferroelectricity in hafnium oxide thin films,” *Appl. Phys. Lett.*, vol. 99, no. 10, p. 102903, 2011.
- [39] X. Sang, E. D. Grimley, T. Schenk, U. Schroeder, and J. M. LeBeau, “On the structural origins of ferroelectricity in HfO₂ thin films,” *Appl. Phys. Lett.*, vol. 106, no. 16, p. 162905, 2015.
- [40] E. D. Grimley, T. Schenk, X. Sang, M. Pešić, T. Mikolajick, and J. M. Lebeau, “Structural Changes Underlying Field-Cycling Phenomena in Ferroelectric HfO₂

- Thin Films,” *Adv. Electron. Mater.*, 2016.
- [41] R. Batra, T. D. Huan, J. L. Jones, G. A. Rossetti, and R. Ramprasad, “Factors Favoring Ferroelectricity in Hafnia: A First Principles Computational Study,” *J. Phys. Chem. C*, p. acs.jpcc.6b11972, 2017.
- [42] J. Müller, T. S. Böske, D. Bräuhäus, U. Schröder, U. Böttger, J. Sundqvist, P. Kücher, T. Mikolajick, and L. Frey, “Ferroelectric Zr_{0.5}Hf_{0.5}O₂ thin films for nonvolatile memory applications,” *Appl. Phys. Lett.*, vol. 99, no. 11, p. 112901, 2011.
- [43] Y. W. Lu, J. Shieh, and F. Y. Tsai, “Induction of ferroelectricity in nanoscale ZrO₂ / HfO₂ bilayer thin films on Pt / Ti / SiO₂ / Si substrates,” *Acta Mater.*, vol. 115, pp. 68–75, 2016.
- [44] E. Yurchuk, J. Müller, S. Knebel, J. Sundqvist, A. P. Graham, T. Melde, U. Schröder, and T. Mikolajick, “Impact of layer thickness on the ferroelectric behaviour of silicon doped hafnium oxide thin films,” *Thin Solid Films*, vol. 533, pp. 88–92, 2013.
- [45] T. Olsen, U. Schroeder, S. Muller, A. Krause, D. Martin, A. Singh, J. Muller, M. Geidel, and T. Mikolajick, “Co-sputtering yttrium into hafnium oxide thin films to produce ferroelectric properties,” *Appl. Phys. Lett.*, vol. 101, no. 8, pp. 3–7, 2012.
- [46] S. Starschich, D. Griesche, T. Schneller, R. Waser, and U. Böttger, “Chemical solution deposition of ferroelectric yttrium-doped hafnium oxide films on platinum electrodes,” *Appl. Phys. Lett.*, vol. 104, no. 20, pp. 1–5, 2014.
- [47] J. Singh, C. Singh, D. Kaur, S. Bindra Narang, R. Jotania, and R. Joshi, “Investigation on structural and microwave absorption property of Co²⁺ and Y³⁺ substituted M-type Ba-Sr hexagonal ferrites prepared by a ceramic method,” *J. Alloys Compd.*, 2016.

- [48] R. Kinet Mech Cat, M. Rahim Uddin, M. R. Khan, M. Wasikur Rahman, A. Yousuf, and C. Kui Cheng, "Photocatalytic reduction of CO₂ into methanol over CuFe₂O₄/TiO₂ under visible light irradiation," *React. Kinet. Mech. Catal.*, vol. 10, no. 10, pp. 1174–1181, 2016.
- [49] P. Rao, R. V. Godbole, and S. Bhagwat, "Nanocrystalline pd:NiFe₂O₄ thin films: A selective ethanol gas sensor," *J. Magn. Magn. Mater.*, 2016.
- [50] G. O. WHITE and C. E. PATTON, "MAGNETIC-PROPERTIES OF LITHIUM FERRITE MICROWAVE MATERIALS," *J. Magn. Magn. Mater.*, vol. 9, no. 4, pp. 299–317, 1978.
- [51] A. T. Raghavender, D. Pajic, K. Zadro, T. Milekovic, P. V. Rao, K. M. Jadhav, and D. Ravinder, "Synthesis and magnetic properties of NiFe_{2-x}Al_xO₄ nanoparticles," *J. Magn. Magn. Mater.*, vol. 316, no. 1, pp. 1–7, Sep. 2007.
- [52] S.-Y. Bae, C.-S. Kim, and Y.-J. Oh, "Magnetic properties of sol-gel derived Ni–Zn ferrite thin films on yttria stabilized zirconia buffered Si(100)," *J. Appl. Phys.*, vol. 85, no. 8, pp. 5226–5228, 1999.
- [53] N. Hosni, K. Zehani, T. Bartoli, L. Bessais, and H. Maghraoui-Meherzi, "Semi-hard magnetic properties of nanoparticles of cobalt ferrite synthesized by the co-precipitation process," *J. Alloys Compd.*, 2016.
- [54] S. Seifikar, T. Rawdanowicz, W. Straka, C. Quintero, N. Bassiri-Gharb, and J. Schwartz, "Structural and magnetic properties of sol–gel derived NiFe₂O₄ thin films on silicon substrates," *J. Magn. Magn. Mater.*, vol. 361, no. 3, pp. 255–261, 2014.
- [55] J. Z. Jiang, G. F. Goya, and H. R. Rechenberg, "Magnetic properties of nanostructured

- CuFe₂O₄,” *J. PHYSICS-CONDENSED MATTER*, vol. 11, no. 20, pp. 4063–4078, May 1999.
- [56] C. Liu, B. S. Zou, A. J. Rondinone, and J. Zhang, “Chemical control of superparamagnetic properties of magnesium and cobalt spinel ferrite nanoparticles through atomic level magnetic couplings,” *J. Am. Chem. Soc.*, vol. 122, no. 26, pp. 6263–6267, Jul. 2000.
- [57] J. Peng, M. Hojamberdiev, Y. Xu, B. Cao, J. Wang, and H. Wu, “Hydrothermal synthesis and magnetic properties of gadolinium-doped CoFe₂O₄ nanoparticles,” *J. Magn. Magn. Mater.*, vol. 323, no. 1, pp. 133–137, Jan. 2011.
- [58] P. C. DORSEY, S. E. BUSHNELL, R. G. SEED, and C. VITTORIA, “EPITAXIAL YTTRIUM-IRON-GARNET FILMS GROWN BY PULSED-LASER DEPOSITION,” *J. Appl. Phys.*, vol. 74, no. 2, pp. 1242–1246, Jul. 1993.
- [59] J. P. Chen, C. M. Sorensen, K. J. Klabunde, G. C. Hadjipanayis, E. Devlin, and A. Kostikas, “Size-dependent magnetic properties of MnFe₂O₄ fine particles synthesized by coprecipitation,” *Phys. Rev. B*, vol. 54, no. 13, pp. 9288–9296, Oct. 1996.
- [60] J. Smit and H. P. Wijn, *Ferrites: physical properties of ferrimagnetic oxides in relation to their technical applications*. New York: Wiley, 1959.
- [61] M. M. El-Okr, A. Ashery, M. F. Zawrah, and A. B. A. Hammad, “Structural and Magnetic Analysis on Spinel (NiFe₂O₄) Prepared By Sol Gel Process at Different Calcinations Temperatures Structural and Magnetic Analysis on Spinel (NiFe₂O₄) Prepared,” *IOSR J. Appl. Phys.*, vol. 8, no. 3, pp. 15–19, 2016.
- [62] P. O. HOFFMANN, “Magnetic and Magnetostrictive Properties of Magnesium Nickel

- Ferrites,” *J. Am. Ceram. Soc.*, vol. 40, no. 7, pp. 250–252, 1957.
- [63] B. Sarkar, B. Dalal, V. D. Ashok, K. Chakrabarti, A. Mitra, and S. K. De, “Magnetic properties of mixed spinel BaTiO₃-NiFe₂O₄ composites,” *J. Appl. Phys.*, vol. 115, no. 12, p. 123908, Mar. 2014.
- [64] I. C. Nlebedim, Y. Melikhov, and D. C. Jiles, “Temperature dependence of magnetic properties of heat treated cobalt ferrite,” *J. Appl. Phys.*, vol. 115, no. 4, p. 43903, 2014.
- [65] I. C. Nlebedim and D. C. Jiles, “Dependence of the magnetostrictive properties of cobalt ferrite on the initial powder particle size distribution,” *J. Appl. Phys.*, vol. 115, no. 17, p. 17A928, 2014.
- [66] J. Barbosa, B. Almeida, A. M. Pereira, J. P. Araújo, I. Gomes, and J. Mendes, “Stress induced magnetic anisotropy on BaTiO₃-CoFe₂O₄ nanogranular composite thin films,” *J. Non. Cryst. Solids*, vol. 354, no. 47–51, pp. 5250–5252, Dec. 2008.
- [67] R. Nongjai, S. Khan, K. Asokan, H. Ahmed, and I. Khan, “Magnetic and electrical properties of In doped cobalt ferrite nanoparticles,” *J. Appl. Phys.*, vol. 112, no. 8, p. 84321, 2012.
- [68] R. M. Cornell and h. c. U. Schwertmann, *The iron oxides: structure, properties, reactions, occurences and uses*, 2nd ed. Wiley-VCH Verlag, 2003.
- [69] J. M. D. Coey, *Magnetism and Magnetic Materials*. Cambridge University Press, 2009.
- [70] R. W. Schwartz, “Chemical Solution Deposition of Perovskite Thin Films,” *Chem. Mater.*, vol. 9, no. 11, pp. 2325–2340, 1997.

- [71] K. W. Kim, P. S. Cho, S. J. Kim, J. H. Lee, C. Y. Kang, J. S. Kim, and S. J. Yoon, "The selective detection of C₂H₅OH using SnO₂-ZnO thin film gas sensors prepared by combinatorial solution deposition," *Sensors Actuators, B Chem.*, vol. 123, no. 1, pp. 318–324, 2007.
- [72] D. B. Hall, P. Underhill, and J. M. Torkelson, "Spin Coating of Thin and Ultrathin Polymer Films," *Polym. Eng. Sci.*, vol. 38, no. 12, pp. 2039–2045, 1998.
- [73] G. H. Kim, H. J. Lee, A. Q. Jiang, M. H. Park, and C. S. Hwang, "An analysis of imprinted hysteresis loops for a ferroelectric Pb(Zr,Ti)O₃ thin film capacitor using the switching transient current measurements," *J. Appl. Phys.*, vol. 105, no. 4, p. 44106, 2009.
- [74] F. Wang and S. Leppavuori, "Properties of epitaxial ferroelectric PbZr_{0.56}Ti_{0.44}O₃ heterostructures with La_{0.5}Sr_{0.5}CoO₃ metallic oxide electrodes," *J. Appl. Phys.*, vol. 82, no. 3, pp. 1293–1298, 1997.
- [75] J. Thongrueng, T. Tsuchiya, Y. Masuda, S. Fujita, and K. Nagata, "Properties and Degradation of Polarization Reversal of Soft BaTiO₃ Ceramics for Ferroelectric Thin-Film Devices," *Jpn. J. Appl. Phys.*, vol. 38, pp. 5309–5313, 1999.
- [76] Z. Bazhan, F. E. Ghodsi, and J. Mazloom, "Surface morphology, optical, and electrochromic properties of nanostructured nickel ferrite (NiFe₂O₄) prepared by sol–gel method: effects of Ni/Fe molar ratios," *Appl. Phys. A*, vol. 122, no. 5, p. 551, 2016.
- [77] J. H. Hubbell and S. M. Seltzer, "X-Ray Mass Attenuation Coefficients." [Online]. Available: <https://www.nist.gov/pml/x-ray-mass-attenuation-coefficients>.
- [78] D. Damjanovic, "Ferroelectric, dielectric and piezoelectric properties of ferroelectric

- thin films and ceramics,” *Rep. Prog. Phys.*, vol. 61, pp. 1267–1324, 1998.
- [79] B. J. Norris, “Low-cost deposition methods for transparent thin-film transistors,” Oregon State University, 2003.
- [80] R. E. Simpson, M. Krbal, P. Fons, A. V Kolobov, J. Tominaga, T. Uruga, and H. Tanida, “Toward the Ultimate Limit of Phase Change in $\text{Ge}_2\text{Sb}_2\text{Te}_5$,” *Nano. Lett.*, vol. 10, no. 2, pp. 414–419, 2010.
- [81] C. J. Glassbrenner and G. A. Slack, “Thermal Conductivity of Silicon and Germanium from 3°K to the Melting Point,” *Phys. Rev.*, vol. 134, no. 4A, pp. A1058–A1069, 1964.
- [82] Kyocera, “Single Crystal Sapphire.” [Online]. Available: http://global.kyocera.com/prdct/fc/product/pdf/s_c_sapphire.pdf.
- [83] M. Asheghi, K. Kurabayashi, R. Kasnavi, and K. E. Goodson, “Thermal conduction in doped single-crystal silicon films,” *J. Appl. Phys.*, vol. 91, no. 8, pp. 5079–5088, 2002.
- [84] Y. Okada and Y. Tokumaru, “Precise determination of lattice parameter and thermal expansion coefficient of silicon between 300 and 1500 K,” *J. Appl. Phys.*, vol. 56, no. 2, pp. 314–320, 1984.
- [85] V. Pishchik, L. A. Lytvynov, and E. R. Dobrovinskaya, *Sapphire*. 2009.
- [86] J. E. Jaffe, R. A. Bachorz, and M. Gutowski, “Low-temperature polymorphs of ZrO_2 and HfO_2 : A density-functional theory study,” *Phys. Rev. B - Condens. Matter Mater. Phys.*, vol. 72, no. 14, pp. 1–9, 2005.
- [87] W. M. Yim and R. J. Paff, “Thermal expansion of AlN , sapphire, and silicon,” *J. Appl. Phys.*, vol. 45, no. 3, pp. 1456–1457, 1974.

- [88] S. R. Skaggs, “Zero and low coefficient of thermal expansion of polycrystalline oxides,” *Tech. Rep. LA-6918 MS, Los Alamos Sci. Lab*, 1977.
- [89] J. W. Arblaster, “Crystallographic properties of platinum,” *Platin. Met. Rev.*, vol. 41, no. 1, pp. 12–21, 1997.
- [90] M. Marlo and V. Milman, “Density-functional study of bulk and surface properties of titanium nitride using different exchange-correlation functionals,” *Phys. Rev. B*, vol. 62, no. 4, pp. 2899–2907, 2000.
- [91] C. W. C., “Thermophysical Data on Platinum,” *Platin. Met. Rev.*, vol. 28, no. 4, pp. 164–165, 1984.
- [92] J. Mukerji and S. K. Biswas, “Synthesis, Properties, and Oxidation of Alumina-Titanium Nitride Composites,” *J. Am. Ceram. Soc.*, vol. 73, no. 1, pp. 142–145, 1990.
- [93] J. Weng, W. Chen, W. Xia, J. Zhang, Y. Jiang, and G. Zhu, “Low-temperature solution-based fabrication of high-k HfO₂ dielectric thin films via combustion process,” *J. Sol-Gel Sci. Technol.*, pp. 1–7, 2016.
- [94] K. Tetzner, K. A. Schroder, and K. Bock, “Photonic curing of sol-gel derived HfO₂ dielectrics for organic field-effect transistors,” *Ceram. Int.*, vol. 40, no. 10, pp. 15753–15761, 2014.
- [95] C. Avis, Y. G. Kim, and J. Jang, “Solution processed hafnium oxide as a gate insulator for low-voltage oxide thin-film transistors,” *J. Mater. Chem.*, vol. 22, no. 34, p. 17415, 2012.
- [96] T. Nishimura, L. Xu, S. Shibayama, T. Yajima, S. Migita, and A. Toriumi, “Ferroelectricity of nondoped thin HfO₂ films in TiN / HfO₂ / TiN stacks,” vol. 1.

- [97] L. V Yakovkina, T. P. Smirnova, V. O. Borisov, V. N. Kichai, and V. V Kaichev, "Synthesis and Properties of Dielectric $(\text{HfO}_2)_{1-x}(\text{Sc}_2\text{O}_3)_x$ Films," vol. 49, no. 2, pp. 172–178, 2013.
- [98] T. Shiraishi, K. Katayama, T. Yokouchi, T. Shimizu, T. Oikawa, O. Sakata, H. Uchida, Y. Imai, T. Kiguchi, T. J. Konno, and H. Funakubo, "Effect of the film thickness on the crystal structure and ferroelectric properties of $(\text{Hf}_{0.5}\text{Zr}_{0.5})\text{O}_2$ thin films deposited on various substrates," *Mater. Sci. Semicond. Process.*, no. July, pp. 0–1, 2016.
- [99] P. V. Jithin, P. K. Baghya, N. Roona, A. Thomas, N. Thomas, V. D. Sudheesh, V. Sebastain, and N. Lakshmi, "Synthesis and characterization of $\text{Co}_x\text{Ni}_{1-x}\text{Fe}_2\text{O}_4$ samples by solution combustion method using glycine as fuel," *Phys. Status Solidi*, vol. 6, pp. 1–6, 2016.
- [100] S. Maensiri, C. Masingboon, B. Boonchom, and S. Seraphin, "A simple route to synthesize nickel ferrite (NiFe_2O_4) nanoparticles using egg white," *Scr. Mater.*, vol. 56, no. 9, pp. 797–800, May 2007.
- [101] C. Dong, G. Wang, D. Guo, C. Jiang, and D. Xue, "Growth , structure , morphology , and magnetic properties of Ni ferrite films," *Nanoscale Res. Lett.*, vol. 8, no. 196, pp. 1–5, 2013.
- [102] K. Maaz, A. Mumtaz, S. K. Hasanain, and M. F. Bertino, "Temperature dependent coercivity and magnetization of nickel ferrite nanoparticles," *J. Magn. Magn. Mater.*, vol. 322, no. 15, pp. 2199–2202, 2010.
- [103] S. Riedel, P. Polakowski, and J. Müller, "A thermally robust and thickness

independent ferroelectric phase in laminated hafnium zirconium oxide,” *AIP Adv.*, vol. 6, no. 9, p. 95123, 2016.

- [104] B.-T. Lin, Y.-W. Lu, and M.-J. Chen, “Induction of ferroelectricity in nanoscale ZrO₂ thin films on Pt electrode without post-annealing,” *J. Eur. Ceram. Soc.*, 2016.